Aalto-yliopisto
Insinööritieteiden
korkeakoulu

Sabra Razooqibastak

A Numerical Investigation of Ship Responses in Head Sea

Thesis submitted for examination for the degree of Master of Science in Technology.

Espoo: 23.11.2017
Supervisor: Prof. Jani Romanoff (Aalto University)
Advisors: DSc. Tommi Mikkola (Aalto University) &
MSc. Matthew Patey (Foreship Oy.)

Aalto University
School of Engineering

Aalto University, P.O. BOX 11000, 00076 AALTO
www.aalto.fi

Abstract of master's thesis

Author Sabra Razooqibastak

Title of thesis A Numerical Investigation of Ship Responses in Head Sea

Degree programme Mechanical engineering

Major/minor Maritime Engineering **Code** ENG25

Thesis supervisor Prof. Jani Romanoff (Aalto University)

Thesis advisor(s) DSc. Tommi Mikkola (Aalto University), MSc. Matthew Patey (Foreship Oy.)

Date 23.11.2017 **Number of pages** 58+60 **Language** English

Abstract

This thesis aims to provide a numerical framework to investigate ship motions in head train waves with sufficient accuracy and least computational and financial effort. OpenFOAM CFD software is utilized along with the waves2Foam package to assess the problem. Due to the complexity of the problem three steps are taken to reach the goal.

The first step was a systematic grid refinement study of wave propagation in a two-dimensional wave flume tank. An example ocean wave was defined using a grid with a specific number of divisions over the wave height and with a specific aspect ratio. The cells in the directions of wave height and wavelength are refined four times, each time with factor of square root of two. Two courant numbers were considered, resulting in a total of 50 cases. The results show no adverse effect with long cells meaning higher edge length in the wave-propagation direction. It was found that tall cells (high y-to-x aspect ratio) caused ripples in the free-surface. It was found that the number of cells over the wave height has the most impact on the computed wave amplitude. It was also found that the phase shift is a function of the time step and the number of cells in the wavelength direction.

In the second step, forces on a cylinder in a three-dimensional domain were assessed considering two grids. Comparing the results with experimental data shows an excellent agreement for both cases.

The third step was computing ship motions with a constant forward speed in head waves. SST turbulence model is utilized to deal with turbulence features of the problem. The ship is set to pitch and heave freely, but other motion components were fixed. Due to the symmetric nature of the problem, only a half-domain is simulated to reduce the computational effort. The results were compared to experimental data, and favorable accuracy is obtained.

At the final stage, the ship model was enlarged with a factor of 5 and assessed with a comparable set-up and mesh to model scale simulation. The result shows higher values of pitch motions. Some possible reasons for these discrepancies between different model scales are discussed.

Keywords CFD, OpenFOAM, waves2Foam, heave, pitch, Stokes waves, seakeeping

Preface

This Thesis is written as a part of Master of Science in Mechanical Engineering of Aalto University. The work is supported by Foreship Oy. a Finnish ship design and engineering company.

I wish to express my deep gratitude to my instructor (DSc.) Tommi Mikkola, who not only invested many of his hours to advise me on the thesis but also guided me during the whole master program with patience and helped me to find my way better. I would like to acknowledge Prof. Amin Chabchoub, my former supervisor who dedicated a lot of time to my thesis and gave me valuable comments and suggestions to achieve my thesis goals. I would like to thank my supervisor Prof. Jani Romanoff, who kindly accepted me in a busy time and helped me to deliver this thesis.

I also wish to thank my instructor (MSc.)Matthew Patey for fruitful and guiding discussions and support during the process. I should thank all my colleagues in Foreship Oy., especially Niilo Luukkainen for his exceptional comments and Conny Söderholm for his kind help with the geometry CAD.

I would like to acknowledge the Finnish Information Technology Center for Science (CSC) for providing me numerous CPU hours which was essential for my studies. I wish to indeed thank Mr. Esko Järvinen for his kind assistance and technical support during my thesis.

I also wish to thank Aalto University for providing the opportunity to study in this program and Foreship Oy. for supporting my thesis.

I would like to dedicate this thesis to,
All my family members who always loved me and support me, even, when they did not agree with me;

My newborn nephew Shahriar, who brings new joy to my life;

All my wonderful friends and my boyfriend Rafael Alberto Valpaços de Lemos Leal who encouraged me and supported me along the way.

Espoo 23.11.2017

Sabra Razooqibastak

Table of Contents

List of Figures

List of Tables

List of Symbols and Abbreviations

A	matrix of discretized equation coefficients in OpenFOAM
C	cell center in OpenFOAM
C_f	face center in OpenFOAM
$CD_{k\omega}$	cross-function coefficient in SST turbulence model
Co	Courant number
D	cylinder diameter
E	wave energy
H	wave height
F_1	blending function of SST turbulence model
F_2	blending function of SST turbulence model
$\mathcal{K}$	Von Kármán constant
Ma	Mach number
P	production term in SST turbulence model
Re	Reynolds number
S	stress invariant
S_{ij}	mean strain rate tensor
S_f	face area vector in OpenFOAM
$\|S_f\|$	face area magnitude in OpenFOAM
T	wave period
U	velocity vector
$\vec{U}_\alpha$	relative compression velocity
V	cell volume in OpenFOAM
a_1	coefficient in SST turbulence model
b	source vector in OpenFOAM
b_1	coefficient in SST turbulence model
c	wave celerity
c_1	coefficient in SST turbulence model
f	wave frequency
g	gravity acceleration
h	free-surface function
k	turbulence kinetic energy
p	pressure
p	x-wise component of angular velocity in equation of pitch motion
q	y-wise component of angular velocity in equation of pitch motion
r	z-wise component of angular velocity in equation of pitch motion
t	time
u	x-wise component of velocity vector
u^+	dimensionless velocity
u_τ	frictional velocity
v	y-wise component of velocity vector
v	kinematic viscosity
x	variable vector in OpenFOAM
y^+	dimensionless distance from the wall
ϕ_g	face motion fluxes in OpenFOAM
α	volume fraction
α_{k1}	coefficient in SST turbulence model
α_{k2}	coefficient in SST turbulence model

$\alpha_{\omega 1}$	coefficient in SST turbulence model
$\alpha_{\omega 2}$	coefficient in SST turbulence model
$\alpha_R(\mathcal{X}_R)$	relaxation function
β	coefficient in SST turbulence model
β^*	coefficient in SST turbulence model
β_1	coefficient in SST turbulence model
β_2	coefficient in SST turbulence model
γ	volume fraction in relaxation zone
γ_1	coefficient in SST turbulence model
γ_2	coefficient in SST turbulence model
ε	turbulence dissipation rate
λ	wavelength
μ	dynamic viscosity
μ_T	turbulent eddy viscosity
ν_t	turbulent kinematic viscosity
ρ	density
σ_k	coefficient in SST turbulence model
σ_ω	coefficient in SST turbulence model
τ_{ij}	shear stress
τ_ω	wall shear stress
φ	potential flow field
ω	specific turbulence dissipation rate
ω	wave angular frequency

Operators

∇	Gradient
$\nabla.$	Divergence
$\nabla \times$	Curl
$\frac{D}{Dt}$	material derivative
.	time derivative

Abbreviations

CAD	Computer Aided Design
CFD	Computational Fluid Dynamics
DIC	Diagonal Incomplete-Cholesky
DNS	Direct Navier Stokes
GAMG	Geometric-Algebraic Multi-Grid
OpenFOAM	Open Field of Operation and Manipulation
PBiCG	Preconditioned (bi-) Conjugate Gradients
PISO	Pressure Implicit with Splitting Algorithm
RANS	Reynolds Averaged Navier Stokes
SST	Shear Stress Transport
URANS	Unsteady Reynolds Averaged Navier Stokes
VOF	Volume of Fluid

1 Introduction

1.1 Introductory Notes

The ship design process is frequently described by a design spiral which is step-wise and iterative. Each step consists of a subsystem design, e.g., machinery system, structural design, which together forms the final solution. The process will repeat on the spiral until the final solution meets all the criteria. The criteria might be a safety concern, economic interest or it might have an environmental purpose. The process is naturally restricted by the financial resources, time and technology limits. These limitations lead to many simplifications.

One crucial feature that historically has been eliminated from the early design process is the dynamic effects due to the presence of waves. It is known that a ship subjected to waves is a dynamic system; however, the cost and complexity of the assessment in the past did not spark interest to increase the accuracy by taking waves into account.

The wave presence mainly affects ship resistance and propulsion, maneuverability, and seakeeping. Most of the methods to evaluate these issues in the past were either experimental approaches or very simplified numerical methods. Experimental techniques are still considered as the most accurate solution for ship seakeeping problems, but they are costly and time inefficient. For example, optimization of the hull for resistance in waves or desired ship motions through the experimental process is inapplicable in term of costs and required time. On the other hand, simplified and fast numerical approaches like potential flow methods gained popularity among the researchers. Many techniques, such as strip theory, are done based on potential flow theory. However, as mentioned they apply many simplifications on the problem; for instance, the flow is inviscid, or the ship is slim, or the waves are not affected by the presence of the ship.

With rapid computer development, more sophisticated approaches like CFD were introduced. Computational Fluid Dynamic (CFD) methods are numerical approaches that are based on Navier-Stokes equations. These methods were soon widely used to obtain the ship resistance in calm water. Recently, many researchers started to develop numerical wave tanks and tools to provide more computationally efficient solutions.

Nowadays, with the increased interest in energy efficiency, as well as the global warming concerns, more accurate prediction of ship resistance is necessary. Also, an authentic assessment of ship motions and consequently maneuverability is crucial in terms of safety and economics which tighten the tolerance of possible errors in the design process.

1.2 Objectives

The primary objective of this thesis is to contribute to ship design development in terms of ship motion assessment with sufficient accuracy and minimum effort in early stages of design. To achieve this, a systematic study of wave propagation with grid refinement is performed. Validation against experimental data are presented. In addition, a possible

scaling effect is investigated to propose an advantage of the computational method over laboratory approaches. It is expected the research work would answer following questions:

- How wave propagate with different grid resolution, aspect ratio, and time step? Alternatively, how these factors will affect the wave characteristics?
- Is it possible to provide a practical numerical model for ship motions that provide sufficient accuracy with low computational and financial effort that could be utilized in early ship design process?
- Is there any effect due to scaling, on ship responses traveling through head train waves?

1.3 Thesis Structure

Chapter 2 provides a background review of research works that have been done in the current subject. It starts with a history of studies on ship/wave hydrodynamics and later provides more recent numerical attempts to model waves. This review was done in the first step of the actual work and was the first source of decisions made for the next steps.

Chapter 3 discusses the governing equations in the system. It explains the Navier-Stokes equations upon which CFD methods are based followed by potential flow theory. After that, derivation of Stokes waves is presented as well as the free-surface and boundary layer treatment.

Chapter 4 introduces the computational tool that is used in the work and discusses its implementation, as well as the link with the governing equations.

Chapter 5 presents the model set up, discussions and results. This chapter is divided into three main parts. In the first part wave propagation in an empty basin is studied. A systematic grid study of a typical ocean wave with two different Courant numbers is presented. The setup as well as results are presented and discussed. After studying general wave behavior an elementary geometry is subjected to a wave train in order to see does correct wave necessarily cause the correct load on the object. The point of the first two stages is to solve a complicated problem step by step and decrease the number of unknowns and uncertainties in the final problem. The set-up, as well as the results are discussed in this part also. In the final part first, a model-scale ship with forward speed in the head waves is simulated, and the results are validated with experimental data. Next, a larger scale is simulated and compared to the smaller scale. As with the previous two parts, the set-up and results are discussed.

The summery of the thesis and conclusion, as well as proposed future work , are provided in chapter 6.

The scope of this work is limited to:
Only head waves, meaning encounter angle of 180 degree, are studied. The waves are modeled with Stokes theory and only waves in the range of Stokes' second order wave theory are studied. Variation of parameters i.e. number of cells in wavelength, wave height and in the y-direction, Courant number, wave characteristics, are very limited due to time and resources considered for a master thesis project. Ship responses are restricted to only pitch and heave motions.

2 Literature Review

One of the earliest studies on the hydrodynamics of ship in waves is done by Kent. He performed studies on model (Kent, 1922) and full-scale ships (Kent, 1924) in different wave types to determine the relationship between the real condition and calm water resistance. He finally concludes that pitch motions mainly cause added resistance due to the wave presence and the maximum value occurs when the encounter frequency is close to the natural pitching frequency. Moreover, it is pointed out that resistance increases if the ratio of ship length to wavelength is slightly less than one.

He also demonstrates some tests in which ships were exposed to irregular seas with different wave types and concluded that the resistance of a ship in an irregular sea could be approximated accurately enough by testing the ship in a regular waves with average wavelength and height of the sea state.

After Kent's studies, the need for more revealing and practical methods to deal with the ship-wave interaction problem was evident. At the time it was not possible to perform a full solution of the Navier-Stokes equations, and most of the numerical studies were done with potential flow theory due to technology limits. The potential solution for multiphase fluids should satisfy two conditions: the Neumann condition, which means no flow through the body is allowed, and the Stokes condition for wave potential and preservation of the free surface. However, for a complicated problem like a moving ship in waves, many simplifications are usually applied to the Neumann-Stokes problem.

Prior to this approach, some methods were already developed. Michell (1898) was one of the pioneers that developed a numerical approach to solve flow around a moving ship. He assumed the ship is thin and can be considered two dimensional. Applying this simplification, he was able to linearize the boundary condition. Moreover, he considered the ratio between wave amplitude and wavelength are small and linearized the free-surface. This method is called Thin Ship Theory.

Another approach that was applied was based on the Froude-Krylov hypothesis (Froude, 1861; Krylov, 1896, 1898). It proposes that in a wave system the pressure field can be estimated regardless of the substantial body presence. In simple words, the sea-waves can be solved separately from generated waves. Froude first proposes this idea in 1861 but it was investigated more by Krylov in 1896 and 1898. With this approach, the pressure loads on the hull can be estimated by undisturbed pressure fields due to waves. However, this method is more like a rough estimate, and it is not valid if the waves are disturbed by the hull.

In 1929, Lewis developed a new idea called strip theory (Lewis, 1929), to deal with the Neumann-Stokes problem. In this method, the ship is split into transverse sections. It is assumed the sections are thin, thus the problem can be treated as two dimensional and the result can be estimated by adding the solutions of each section together. In each strip, the problem is solved for a simple geometry and mapped to a hull section with conformal-mapping. The advantage of this method is that it is applicable for most hull shapes. This solution was also nonviscous and applies many simplifications which affect the accuracy of results.

Kreitner in (1939) proposed that the Froude-Krylov hypothesis is not an appropriate method to deal with this complicated problem because it assumes the waves are

unaffected by the hull. He claimed the interaction would affect the wave height and consequently the energy. He also discussed the effect of heave and pitch damping on ship motions and radiation energy loss. However, Havelock (1940), showed that the reflection forces are negligible compared to heave and pitch induced forces.

Hanoka (1957) and Mauro (1957, 1960b) attempted to provide a more detailed solution for calculating the loads on a ship hull traveling through waves. In Hanoka's method, it was assumed that the ship always oscillates with the applied force or moment frequency. This idea was already proposed by Kochin (1937). Mauro proposed that some terms that were neglected in linear theory cause inconsistent results. He suggests three parts for potential:

- Incident wave potential
- Wave generated by ship oscillation
- Wave diffraction by ship potential

He also shows that heaving and pitching are two primary sources of added resistance and waves diffracted by ship cause the third part. In addition, the couplings between each pair of these components will affect the result. Furthermore, he came up with a formula to describe the added resistance from waves and showed it is proportional to the wave height square, supporting Kent's studies assuming resistance changes with velocity squared.

Mauro later (1960a, 1963) substituted the direct integration of pressure with a control volume method and upgraded his approach. He assumed loads on the hull are associated with a difference in momentum in a control volume.

Later, Stern et al. (1987) showed that waves affect the boundary layer of a flat plate. Thus to obtain more accuracy a full viscous solution would be required.

Recently researchers tend to apply a full viscous assessment of the problem. Castiglione *et al.* (2011) performed an analysis to evaluate catamaran motions in waves as well as the effect of wave steepness on ship response and the natural frequency with the URANS solver CFDSHIP-Iowa V.4. They compared the results with strip theory and concluded that RANS provide the results with higher accuracy.

Various software and codes were developed to deal with a full viscous solution of the flow field around a ship. OpenFOAM is one of the tools which was widely used to study this phenomenon and has the advantage of being free and extensible.

Morgan *et al.* (2010) used rasInterFOAM as part of the OpenFOAM library to simulate the propagation of monochromatic waves over a submerged bar. The result shows a good agreement with the experimental data. However the model was suffering from lack of wave absorption techniques, and as a result, the computational domain was vast and inefficient. Later Jacobsen *et al.* (2012) developed a wave generation toolbox called waves2FOAM which generate waves and used an absorption method termed "wave relaxation zones."

Seiffert *et al.* (2014) used this tool as a numerical towing tank and modeled a solitary wave acting on a coastal bridge. Horizontal and vertical forces on a flat plate were

investigated in 133 cases and compared to experimental data. The result shows the solver is very capable of modeling this phenomenon.

Gadelho *et al.* (2014) investigate the effect of an obstacle on two-dimensional wave propagating with OpenFOAM. They used two test cases to evaluate the wave transmission, reflection, and dissipation. The result shows a good agreement and functional performance of the toolbox waves2FOAM.

Jacobsen *et al.* (2015) show the toolbox is capable of modeling the interaction of irregular waves and a porous coastal structure. Chenari *et al.* also in (2015) validate waves2Foam with three different cases and conclude it is not only a powerful tool for generating and absorbing the waves but also it is very capable of modeling the wave breaking.

Wave-structure simulations have been modeled accurately over the recent years, but complicated geometries such as ships were not assessed as widely as coastal objects.
Shen (Shen *et al.*, 2012; Shen and Wan, 2013) performed a RANS simulation to investigate added resistance, heave and pitch motions in different waves with their in-house naoe-Foam-SJTU software developed under the framework of the open source code OpenFOAM and found a good agreement with experimental results.

Considering the extensible and open source advantages of OpenFOAM, as well as the promising results obtained by the software and waves2FOAM package, it is utilized in this work as a numerical tool.

3 Governing Equations

Computational Fluid Dynamics is based on fluid mechanics laws which are the mathematical representation of fundamental physics conservation laws. The conservation laws are:

- Conservation of mass
- Conservation of momentum
- Conservation of energy

Hydrodynamics mainly deals with the two first laws which result in two fundamental equations in Fluid Mechanics: Continuity and Navier-Stokes equations.

3.1 Continuity Equation

The continuity equation is derived from the fundamental conservation of mass law. In a fixed control volume mass is not created nor vanishes. In mathematical terms, in a fixed control volume, the amount of flux which is entering the control volume should be equal to the amount of flux which leaves it in the absence of a mass source. The differential form of the continuity equation is (Larsson and Raven, 2010):

$$\frac{\partial \rho}{\partial t} + \nabla.(\rho U) = 0 \tag{1}$$

where ρ is density and U is flow velocity vector.
Usually flows with low Mach number (≤ 0.3), can be considered incompressible.

$$Ma = \frac{fluid\ speed}{Sound\ speed\ in\ flow} \tag{2}$$

In incompressible flows the density is constant, and the continuity equation will reduce to:

$$\nabla.U = 0 \tag{3}$$

Assuming there is no air trapped in the water, the flow can be considered incompressible around the ship.

3.2 Navier-Stokes equations

Navier-Stokes equations are based on the fundamental conservation of momentum law. According to the conservation of momentum, the change in momentum is equal to forces acting on the fluid, which is the representation of Newton's second law. Based on this concept, the Navier-Stokes equations can be derived. For incompressible flows, the equations take the form below.

$$\rho \frac{DU}{Dt} = -\nabla p + \mu \nabla^2 U + \rho g \tag{4}$$

where p is pressure and g is gravity force.

3.3 RANS and Turbulence Models

A full calculation of the Navier-Stokes equations, known as Direct Numerical Simulation (DNS), for ships is still beyond the computational power of modern technology. Therefore, other methods are developed to simulate only a desired part of the flow. The most widely used method is currently Reynolds Averaged Navier Stokes (RANS) equations.

3.3.1 Reynolds Averaged Navier-Stokes Equations

Reynolds Averaged Navier-Stokes Equations are time averaged Navier-Stokes Equations. These equations are used to describe turbulent flows. The general idea in RANS equations is decomposition of the equations into Time-Averaged and Fluctuation Quantities. Removing the fluctuation arising from turbulence from the time-averaged equation is done by averaging the equations over a time larger than the largest scale of turbulence. However, the fluctuations will not wholly vanish due to non-linearity. This fluctuation term is presented as a tensor called Reynolds Stress.(Larsson and Raven, 2010)

3.3.2 Turbulence Modeling

Turbulence models are models to describe the turbulent flows. A brief classification of the models is discussed in the following.

The Boussinesq Assumption

This assumption is the most important approximation in turbulence theory. It relates the Reynolds Stresses to the rate of strain tensor in a similar way that relates viscous stresses to the Strain Tensor. The only difference is replacing the dynamic viscosity μ with its equivalent turbulent viscosity μ_T. Unlike the dynamic viscosity, this value is not constant and should be calculated at every point. This assumption is the base of Zero-equation models, One-equation models & Two-equation models. However, this assumption only applies when the stress tensor is caused by molecular activity not turbulence.

The Zero-Equation Models

In this model turbulent quantities are calculated with an algebraic equation. Some of these models were popular for aerodynamic purposes for many years but these are not a proper model to simulate complex problems like flow at the stern of the ship.

One-Equation Models

In these turbulent models a transport equation is solved for k, which is Turbulent Kinetic Energy and represents the energy in turbulence.

Two-Equation Models

In two-equation models, turbulence is treated by two equations. One of the most famous models is $k-\varepsilon$ where k is the same as described and epsilon represents the dissipation energy. Although this model is very popular, it is not very suitable for flow with strong streamwise vortices. Therefore this model is not appropriate for predicting the wake

around ship. An alternative solution is the $k-\omega$ model, where the omega is specific energy dissipation rate. This model also has some difficulties which should be overcome. One of the well-known modifications of the $k-\omega$ model is Menter's Shear Stress Transport (SST) model.

Algebraic Stress and Reynold Stress Models

As mentioned earlier, some modifications are required for the Boussinesq assumption. In Reynolds Stress models, transport equations for each of the 6 Reynolds stress components are solved and most often an additional equation will be included.

$k-\omega$ *SST* Turbulence Model

The Shear Stress Transport (SST) turbulence model, is a two-equation model introduced by Menter (1994). The idea of this model is to combine the two $k-\varepsilon$ and $k-\omega$ models to reinforce their qualities. The $k-\varepsilon$ model is robust; however it fails when it comes to boundary layer flow. On the other hand $k-\omega$ is more accurate in modeling the boundary layer flow as well as flows with adverse pressure gradients but it is very responsive to the value of ω in the free-stream (Wilcox, 2008). The Menter model uses $k-\omega$ in the boundary layer and transforms to $k-\varepsilon$ in the free-stream flow to take advantage of both models. To combine these two formulations, the SST model uses a blending function which computes the proper distance from the wall at which to switch the model.

The SST latest version (Menter, Kuntz and Langtry, 2003) is formulated as shown below:

Turbulence kinetic energy equation:

$$\frac{\partial}{\partial t}(\rho k)+\frac{\partial(\rho u_j k)}{\partial x_j}=\frac{\partial}{\partial x_j}\left[(\mu+\sigma_k\mu_t)\frac{\partial k}{\partial x_j}\right]+P-\rho\beta^*\omega k \tag{5}$$

Turbulence frequency equation:

$$\begin{aligned}\frac{\partial}{\partial t}(\omega k)+\frac{\partial(\rho u_j \omega)}{\partial x_j}&\\ =\frac{\partial}{\partial x_j}\left[(\mu+\sigma_\omega\mu_t)\frac{\partial \omega}{\partial x_j}\right]+\frac{\rho\gamma P}{\nu_t}-\rho\beta\omega^2&\\ -\rho(F_1-1)CD_{k\omega}&\end{aligned} \tag{6}$$

where P is production term:

$$P=\min(G,10\beta^*\rho\omega k) \tag{7}$$

$$G=\tau_{ij}\frac{\partial u_i}{\partial x_j} \tag{8}$$

$$\tau_{ij}=\mu_t\left(2S_{ij}-\frac{2}{3}2S_{ij}\frac{\partial u_k}{\partial x_k}\delta_{ij}\right)-\frac{2}{3}\rho\delta_{ij} \tag{9}$$

$$S_{ij} = \frac{1}{2}\left(\frac{\partial u_i}{\partial x_j} + \frac{\partial u_j}{\partial x_i}\right) \tag{10}$$

$$CD_{k\omega} = \max\left(2\rho\sigma_{\omega 2}\frac{1}{\omega}\frac{\partial k}{\partial x_i}\frac{\partial \omega}{\partial x_i}, 10^{-10}\right) \tag{11}$$

μ_t is turbulent eddy viscosity :

$$\mu_t = \frac{\rho a_1 k}{\max(a_1\omega, SF_2)} \tag{12}$$

Each constant is blended with blending functions.

$$\phi = F_1\phi_1 + (1 - F_1)\phi_2 \tag{13}$$

$$F_1 = \tanh\left\{\left\{\min\left[\max\left(\frac{\sqrt{k}}{\beta^*\omega y}, \frac{500\nu}{y^2\omega}\right), \frac{4\rho\sigma_{\omega 2}k}{CD_{k\omega}y^2}\right]\right\}^4\right\} \tag{14}$$

S is strain invariant and F_2 is a second blending function.

$$F_2 = \tanh\left\{\left\{\max\left(\frac{2\sqrt{k}}{\beta^*\omega y}, \frac{500\nu}{y^2\omega}\right)\right\}^2\right\} \tag{15}$$

$$\mathrm{S} = \sqrt{2S_{ij}\,S_{ij}} \tag{16}$$

The constants are:

α_{k1}	α_{k2}	$\alpha_{\omega 1}$	$\alpha_{\omega 2}$	β_1	β_2	β^*	γ_1	γ_2	a_1	b_1	c_1
0.85	1.0	0.5	0.856	0.075	0.0828	0.09	5/9	0.44	0.31	1.0	10.0

3.4 Boundary Layer

Earlier, the Navier-Stokes and continuity equations for an incompressible flow were introduced. Although in reality the flow is viscous, the effect is mainly limited to a thin layer called the "Boundary Layer" next to solid walls. A boundary layer is a thin layer of viscous fluid in the vicinity of a solid wall surface which is in contact with a moving fluid. The flow velocity varies from zero at the wall up to the free-stream velocity at the edge of the boundary layer. This concept was first introduced by Prandtl in 1904. Figure 1 shows the classic evolution of the boundary layer on a flat plate with uniform velocity.

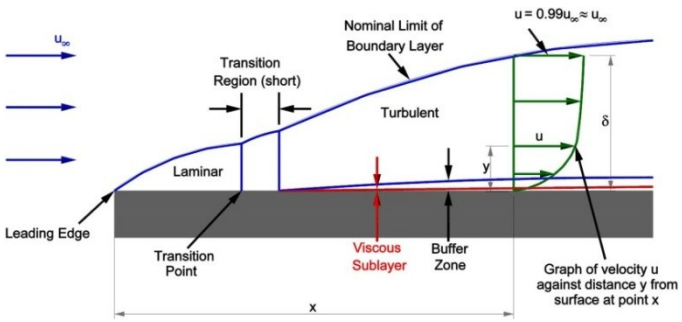

Figure 1 *Progression of boundary layer on a flat plate* (*tutor*)

The transition from laminar to turbulent flows usually occurs around $Re = 5 \times 10^5$. Therefore for normal ship speeds at model scale the flow is considered turbulent.

The turbulent boundary layer is often presented with two non-dimensional quantities y^+ and u^+.

$$y^+ = \frac{u_\tau y}{\nu} \tag{17}$$

$$u^+ = \frac{u}{u_\tau} \tag{18}$$

where, $u_\tau = \sqrt{\tau_\omega/\rho}$ is frictional velocity, τ_ω is the wall shear stress, y^+ is the dimensionless distance from the wall and u^+ is the dimensionless velocity. Figure 2 shows a schematic of the near wall region.

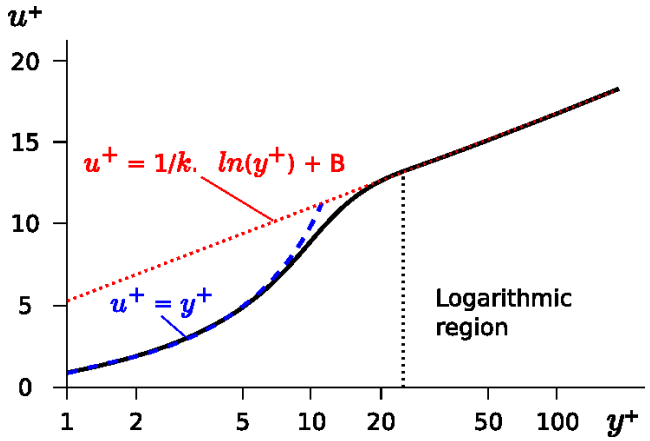

Figure 2 *Turbulent boundary layer regions* (*CFD Online*, 2011)

The velocity profile near the wall is divided into three zones: the **viscous sublayer** in which $y^+ < 5$ and the velocity profile is linear ; an **overlap region** which is considered between $5 < y^+ < 30$ and a **logarithmic region** where y^+ lies between 30 to 300. In this region the velocity profile follows a logarithmic curve and can be described as:

$$u^+ = \frac{1}{\mathcal{K}} \ln(y^+) + B \tag{19}$$

Where $\mathcal{K} \approx 0.41$ is a Von Kármán constant and $B \approx 5.1$.
Capturing the boundary layer through the viscous sublayer is computationally expensive since it requires that $y^+ = 1$ next to the wall. To overcome this limitation various wall-functions have been proposed. These functions use the above "law of the wall" as a

fundamental relation between velocity profile and flow shear stress through the whole boundary layer. Implementing this technique, the flow can be solved with coarser grids but on the other hand the accuracy may be reduced. In case wall functions are applied, the y^+ value should be set in the logarithmic region ($30 < y^+ < 300$). (White, 2006)

3.5 Potential Flow Theory

It is mentioned that viscosity effects are mainly limited to the adjacent wall. Far from the wall in the free stream, the fluid can be approximated as inviscid since the frictional effect is less pronounced. This assumption will simplify the Navier-Stokes equation to the Euler equation. The incompressible Euler equation is expressed as:(Larsson and Raven, 2010)

$$\rho \frac{DU}{Dt} + \nabla p - \rho g = 0 \tag{20}$$

This assumption will considerably decrease the computational cost; however, it will reduce the accuracy of results.

Again considering no friction effect, the flow can also be considered irrotational. Irrotational flow is a flow in which fluid particles are not rotating. Mathematically, it means the curl of velocity is zero.

$$\nabla \times U = 0 \tag{21}$$

Therefore if we define a flow field φ in which $\nabla\varphi = U$, the following statement is valid for any value of φ:

$$\nabla \times \nabla\varphi = 0 \tag{22}$$

where, $\varphi = \varphi(x, y, z, t)$ is a function of space and time and is called the velocity potential. The velocity component of the flow can be represented in terms of velocity potential φ. By substituting the potential velocity into the continuity equation

$$\nabla . \nabla\varphi = 0 \tag{23}$$

the Laplace equation will be obtained:

$$\nabla^2\varphi = 0 \tag{24}$$

3.6 Stokes Wave Theory

Sir George Stokes in the mid-19th century (Stokes, 1847), based on potential flow theory, developed a method to obtain an approximate solution for non-linear gravity wave motions. Stokes waves are harmonic nonlinear gravity waves, which are generated at a finite and infinite water depth and have quite small amplitudes. (Lautrup, 2011)

Assumptions

If the wave originates from the water at rest, the flow can be considered irrotational. In addition since the Reynolds number is quite high in gravity waves, the flow may be assumed inviscid, therefore potential flow theory can be applied to describe the flow. Waves are considered two dimensional. The Cartesian coordinate system is placed on the unperturbed free-surface.

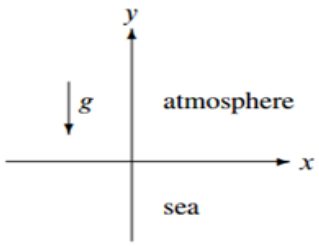

Figure 3 *problem coordinate system* (Lautrup, 2011)

The free surface function can be presented as $y = h(x,t)$. In a very small time interval δt the surface particles will be displaced $\delta x = u\,\delta t$ and $\delta y = v\,\delta t$ in the horizontal and vertical directions respectively. Therefore the free surface function will change as

$$h\,(x+\delta x, t+\delta t) = h(x,t) + \delta y \tag{25}$$

Using a first Taylor expansion:

$$h\,(x+\delta x, t+\delta t) = h(x,t) + \delta x\frac{\partial h}{\partial x} + \delta t\frac{\partial h}{\partial t} + O(\delta x^2) + O(\delta t^2) \tag{26}$$

Therefore,

$$\frac{\partial h}{\partial t} + u\,\nabla_x h = v \quad for \quad y = h \tag{27}$$

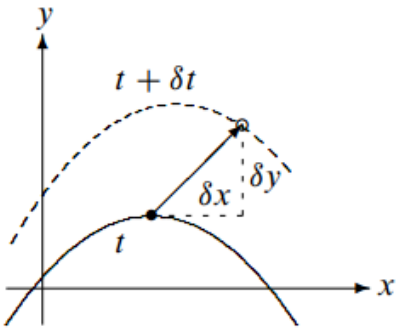

Figure 4 *Motion of surface particle from time* $\boldsymbol{t}$ *to* $\boldsymbol{t+\delta t}$ (Lautrup, 2011)

For a potential flow, the momentum equation is simplified to the Bernoulli equation:

$$\frac{\partial \varphi}{\partial t} + gy + \frac{(u^2+v^2)}{2} + \frac{p}{\rho} = cte \tag{28}$$

where cte is a constant. It is known that pressure at the free surface is defined by the water column below the particle and therefore it can be treated as a constant.

$$\frac{\partial \varphi}{\partial t} + gy + \frac{(u^2 + v^2)}{2} = cte\ for\ \ y = h \tag{29}$$

Applying the impermeability boundary condition at the ocean depth:

$$v = 0\ \ for\ y = -d \tag{30}$$

where $d,$ is the water depth.

Stationary, Symmetric, and Periodic

A wave is called stationary if it progresses without changing shape along a horizontal axis with a constant celerity c. Therefore the potential will be a function of $\varphi = \varphi(x - ct, y)$
Consequently, the surface boundary condition transforms to:

$$v = \frac{(u - c)dh}{dx}\ for\ y = h \tag{31}$$

$$gh = cu - \frac{(u^2 + v^2)}{2} + cte\ \ \ for\ y = h \tag{32}$$

Another feature of Stokes waves are periodicity with the spatial period of λ and symmetry

$$h(x + \lambda) = h(x)\quad and\quad \varphi(x + \lambda, y) = \varphi(x, y) \tag{33}$$

$$\varphi(-x, y) = -\varphi(x, y) \tag{34}$$

The periodicity and symmetry will permit decomposition of the surface function into a Fourier series.

$$h = \sum_{n=1}^{\infty} H_n \cos(n\theta) \tag{35}$$

Since the velocity potential is odd and periodic, it will expand to odd Fourier components of $\varphi \sim f_n(ky)\sin(n\theta)$, where k is the wave number, $\theta = kx - \omega t + \varepsilon$, and ε is the phase. The series should satisfy Laplace equation.

$$f_n'' = n^2 f_n(ky) \tag{36}$$

The general solution of this differential equation is

$$f_n = A_n \cosh(nky) + B_n \sinh(nky) \tag{37}$$

Applying the permeability boundary condition

$$v = 0\ for\ y = -d \tag{38}$$

where $v \sim f_n'(ky)\sin(n\theta)$

This requires that

$$f_n'(-d) = 0 \tag{39}$$

Consequently, the general solution will take the form

$$f_n = \cosh(nk(y+d)) \tag{40}$$

Moreover, the velocity potential can be written as:

$$\varphi = \sum_{n=1}^{\infty} \varphi_n \frac{\cosh(nk(y+d))}{\sin(nkd)} \sin(n\theta) \tag{41}$$

And,

$$u = \sum_{n=1}^{\infty} n\,\varphi_n \frac{\cosh(nk(y+d))}{\sin(nkd)} \cos(n\theta) \tag{42}$$

$$v = \sum_{n=1}^{\infty} n\varphi_n \frac{\sinh(nk(y+d))}{\sin(nkd)} \sin(n\theta) \tag{43}$$

If the wave amplitude is much smaller than the wave length ($ka \ll 1$) the problem can be simplified. In this situation the $\frac{\partial h}{\partial t}$ term in equation (27) will be one order of magnitude smaller than v. Similarly, in equation (32) the term $(u^2 + v^2)$ is one order smaller than other terms in the equation (Alberello, 2017). Therefore:

$$\frac{\partial h}{\partial t} = v \quad for\ y = h \tag{44}$$

$$\frac{\partial \varphi}{\partial t} + gy = 0 \quad for\ \ y = h \tag{45}$$

Since the boundary conditions are defined on an arbitrary surface the problem is still complicated. The velocity at the free surface can be described as a Taylor expansion of the mean value at the mean water level $y = 0$.

$$v\,(y = h) = v(y = 0) + \frac{\partial v}{\partial y}\,(y = h) * h + O((ka)^2) \tag{46}$$

Therefore the governing equations for a linear wave problem will take the form:

$$\nabla^2 \varphi = 0 \tag{47}$$

$$\frac{\partial \varphi}{\partial y} = 0 \quad for\ y = -d \tag{48}$$

$$\frac{\partial h}{\partial t} = v \quad for\ y = 0 \tag{49}$$

$$gy + \frac{\partial \varphi}{\partial t} = 0 \quad for\ y = 0 \tag{50}$$

The solution for a monochromatic linear wave is:

$$h = a.\cos(\theta) \tag{51}$$

$$\varphi = \frac{ag}{\omega}\frac{\cosh\big(k(y+d)\big)}{\cosh(kd)}\sin(\theta) \tag{52}$$

$$u = a\omega\frac{\cosh(k(y+d))}{\sin(kd)}\cos(\theta) \tag{53}$$

$$v = a\omega\,\frac{\sinh(k(y+d))}{\sin(kd)}\cos(\theta) \tag{54}$$

The term ω is coming from the dispersion relation. The dispersion relation in an arbitrary depth is defined by:

$$\omega^2 = gk\tanh(kd) \tag{55}$$

However in deep water where $kd \gg 1$ the relation will simplify to

$$\omega^2 = gk \tag{56}$$

Accordingly, the potential field and velocity components will take the form

$$\varphi = \frac{ag}{\omega}e^{ky}\sin(\theta) \tag{57}$$

$$u = a\omega\, e^{ky}\sin(\theta) \tag{58}$$

$$v = a\omega\, e^{ky}\cos(\theta) \tag{59}$$

Stokes Second Order Wave Theory

When the wave steepness increases, linear theory is no longer valid and higher order terms in the Taylor expansion should be added according to a range of applicability. The range of applicability of theories is presented in Figure 5.

In this study the waves in the range of Stokes second order wave theory are of interest. Hence first and second order terms in the equations should be considered. The governing equations for the second order term are:

Kinematic boundary condition:

$$\frac{\partial h_2}{\partial t} - \frac{\partial \varphi_2}{\partial t} = h_1\frac{\partial^2\varphi_1}{\partial y^2} - \frac{\partial\varphi_1}{\partial x}\frac{\partial h_1}{\partial x} \quad for\ y = 0 \tag{60}$$

Dynamic boundary condition:

$$h_2 + \frac{1}{g}\frac{\partial \varphi_2}{\partial t} = -\frac{1}{g}\left(\frac{1}{2}\frac{\partial \varphi_1}{\partial x}\cdot\frac{\partial \varphi_1}{\partial x} + h_1\frac{\partial^2 \varphi_1}{\partial y \partial t}\right) \quad for\ y = 0 \tag{61}$$

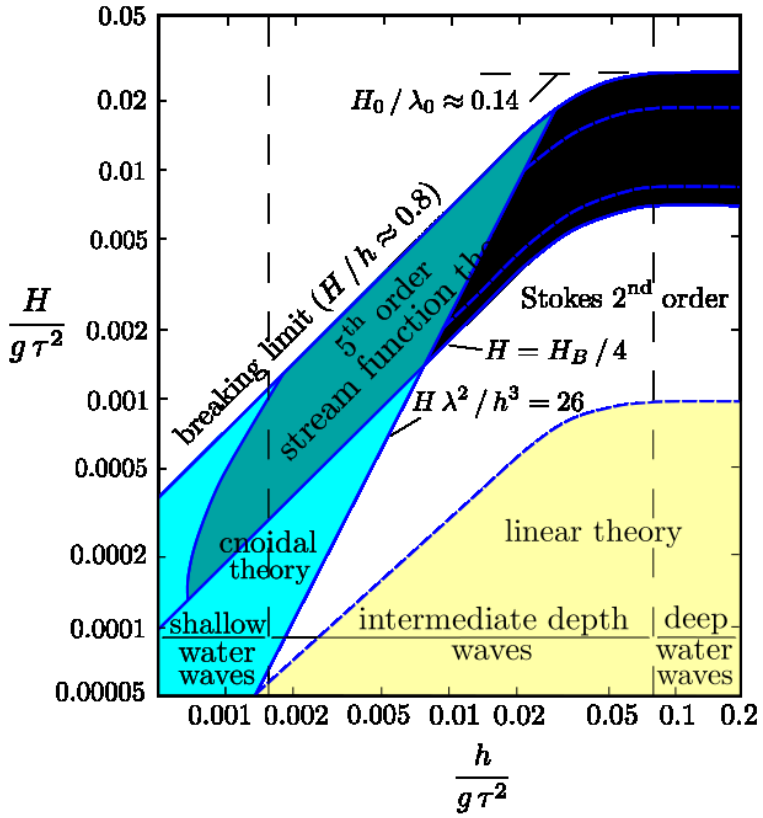

Figure 5 *wave theory validation regions* (LeMéhauté, 1976). *h and H represents water depth and wave height respectively.*

The problem can be re-written as:

$$\nabla^2 \varphi_2 = 0 \tag{62}$$

$$\frac{\partial^2 \varphi_2}{\partial t^2} + g\frac{\partial \varphi_2}{\partial y} = -\frac{\partial}{\partial t}\left(\frac{\partial \varphi_1}{\partial x}\cdot\frac{\partial \varphi_1}{\partial x}\right) + \frac{1}{g}\frac{\partial \varphi_1}{\partial t}\frac{\partial}{\partial y}\left(\frac{\partial^2 \varphi_1}{\partial t^2} + g\frac{\partial \varphi_1}{\partial y}\right) \tag{63}$$

$$h_2 = -\frac{1}{g}\left(\frac{\partial \varphi_2}{\partial t} + \frac{1}{2}\frac{\partial \varphi_1}{\partial x} + h_1\frac{\partial^2 \varphi_1}{\partial y \partial t}\right) \tag{64}$$

In intermediate water depth:

$$h_2 = \frac{1}{4}ka^2\frac{\cosh(kd)}{\sinh^3(kd)}[2 + \cosh(2kd)]\cos(2\theta) \tag{65}$$

$$\varphi_2 = \frac{3}{8}ka^2\frac{\cosh(2k(y+d))}{\sinh^3(kd)\cosh(kd)}\sin(2\theta) \tag{66}$$

$$u_2 = \frac{3\omega}{4k}(ka^2)\frac{\cosh(2k(y+d))}{\sinh^4(kd)}\cos(2\theta) \tag{67}$$

$$v_2 = \frac{3\omega}{4k}(ka^2)\frac{\cosh(2k(y+d))}{\sinh^4(kd)}\sin(2\theta) \tag{68}$$

Therefor:

$$h = h_1 + h_2 = a\cos(\theta) + \frac{1}{4}ka^2\frac{\cosh(kd)}{\sinh^3(kd)}[2+\cosh(2kd)]\cos(2\theta) \tag{69}$$

$$\begin{aligned}\varphi = \varphi_1 + \varphi_2 = {} & \frac{ag}{\omega}\frac{\cosh\big(k(y+d)\big)}{\cosh(kd)}\sin(\theta) \\ & + \frac{3}{8}ka^2\frac{\cosh(2k(y+d))}{\sinh^3(kd)\cosh(kd)}\sin(2\theta)\end{aligned} \tag{70}$$

$$\begin{aligned}u = u_1 + u_2 = {} & a\omega\frac{\cosh(k(y+d))}{\sin(kd)}\cos(\theta) \\ & + \frac{3\omega}{4k}(ka^2)\frac{\cosh(2k(y+d))}{\sinh^4(kd)}\cos(2\theta)\end{aligned} \tag{71}$$

$$\begin{aligned}v = v_1 + v_2 = {} & a\omega\frac{\sinh(k(y+d))}{\sin(kd)}\cos(\theta) \\ & + \frac{3\omega}{4k}(ka^2)\frac{\cosh(2k(y+d))}{\sinh^4(kd)}\sin(2\theta)\end{aligned} \tag{72}$$

In deep water

$$h_2 = \frac{1}{4}ka^2\cos(2\theta) \tag{73}$$

$$\varphi_2 = 0, \quad u_2 = 0, \quad v_2 = 0 \tag{74}$$

Therefore:

$$h = h_1 + h_2 = a\cos(\theta) + \frac{1}{4}ka^2\cos(2\theta) \tag{75}$$

$$\varphi = \varphi_1 + \varphi_2 = \frac{ag}{\omega}\frac{\cosh\big(k(y+d)\big)}{\cosh(kd)}\sin(\theta) \tag{76}$$

$$u = u_1 + u_2 = a\omega\frac{\cosh(k(y+d))}{\sin(kd)}\cos(\theta) \tag{77}$$

$$v = v_1 + v_2 = a\omega\frac{\sinh(k(y+d))}{\sin(kd)}\cos(\theta) \tag{78}$$

3.7 Free Surface Treatment

In multiphase flows, free surface conduction is important. Different methods such as hybrid (a combination of RANS and potential solution) or fully viscous approaches are developed to handle the free surface.

The free surface in OpenFOAM is treated with the Volume of Fluid (VOF) method, presented by Hirt and Nicholas in (1981). In this method, a different volume fraction is assigned to different phases of the same computational fluid. The concept is straightforward. In a two-phase fluid, logically a cell can be full of either one of fluid the phases or partially occupied by both of them. Thus, if a cell full of water is assigned a phase fraction of 1 when it is it is filled with water and 0 when it is filled with air, any value between them indicates that there is both air and water in the cell and the amount is proportional to the volume fraction.

$$\alpha(x,t) = \begin{cases} 1, & water \\ 0, & air \\ 0 < \alpha < 1 & free\ surface \end{cases} \tag{79}$$

In the multiphase region, flow is considered as a mixture. Density and viscosity are computed as

$$\rho = \alpha\rho_1 + (1-\alpha)\rho_2 \tag{80}$$

$$\mu = \alpha\mu_1 + (1-\alpha)\mu_2 \tag{81}$$

The free-surface is expressed as iso-contour $\alpha = 0.5$.
Free-surface deformation can be obtained by solving an additional transport equation for α.

$$\frac{\partial\alpha}{\partial t} + \nabla.\left(\alpha\vec{U}\right) + \nabla.\left(\alpha(1-\alpha)\vec{U}_\alpha\right) = 0 \tag{82}$$

The last term in the equation is called artificial compression. It is added to limit numerical diffusion. $\vec{U}_\alpha$ is relative compression velocity.

The VOF method is capable of dealing with highly non-linear problems. In addition, it allows use of a simple grid and it adds only one additional equation for each fluid, thus it is computationally friendly. (Weller *et al.*, 1998)

4 Computational Tool

4.1 OpenFOAM

Open Source Field Operation and Manipulation (OpenFOAM) is a C^{++} library consist of solvers and utilities for CFD applications. The toolbox is licensed under the GNU license which means it can be downloaded and manipulated by anyone. The overall structure of the software is sketched in Figure 6. (The OpenFOAM Foundation, 2017a)

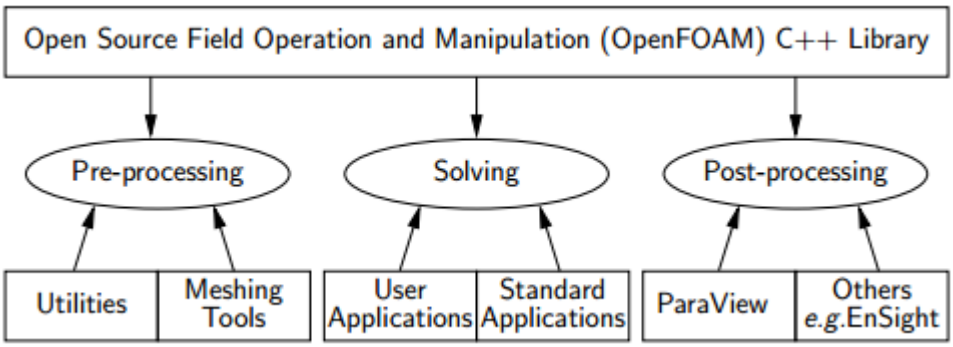

Figure 6 *OpenFOAM library* (The OpenFOAM Foundation, 2017a)

It provides tools for pre- and post-processing and a variety of solvers appropriate for different engineering problems. One advantage of OpenFOAM is that new utilities or solvers can be created by the users adopting relevant knowledge. Also, it provides some templates to make this process more accessible to the users. In this work OpenFOAM version 4.1 is used.

4.2 Discretization in OpenFOAM

In problems for which an analytical solution is not available a discrete solution can be applied. Discretization means an estimation of the problem into discrete quantities. The Finite Volume Method is a discretization technique that is used by OpenFOAM. Similar to other numerical approaches, e.g. Finite Difference, the problem is discretized in three aspects.

Spatial Discretization: This means to define the spatial domain with some points that form non-overlapping finite volumes.

Temporal Discretization: This means to split the simulation of time evolution of the flow into finite steps.

Equation Discretization: This means to transform partial differential equations into algebraic equations by integrating them over each finite volume.

4.2.1 Spatial Discretization

As mentioned, the geometric domain should be discretized into nonoverlapping finite volumes over which partial differential equations would be subsequently transformed to

discrete algebraic equation. The grid cells should be contiguous, non-over-lapping and cover the entire domain. Figure 7 shows a typical computational mesh.

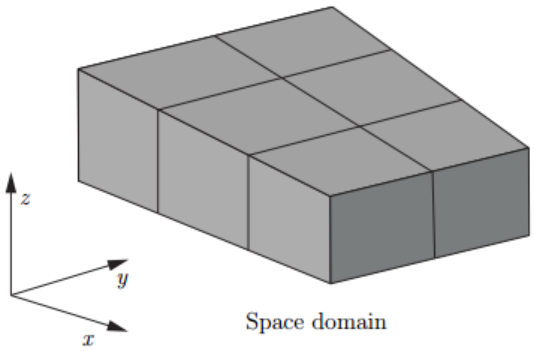

Figure 7 *A typical computational mesh* (The OpenFOAM Foundation, 2017a)

A closer look at the cells is pictured in Figure 8 and shows essential features of a grid in OpenFOAM. P and N represent the centroid of the cell at which dependent variables and some other properties are stored there. Generic label f is given to the set of flat faces which bound the cell. In OpenFOAM, there is no limitation on neither number of faces that bound the cells nor their alignment, which provides more freedom regarding mesh generation and manipulation if the geometry is complex.

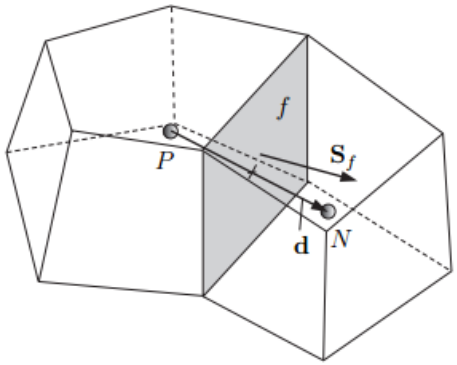

Figure 8 *An arbitrary cell features in OpenFOAM* (The OpenFOAM Foundation, 2017a)

Each face has an area $|S_f|$ with a unit normal vector n pointing to a neighboring cell. The volume of each cell is represented by V. There are two kinds of faces in OpenFOAM Internal and Boundary faces. Internal faces are those which connect two cells, and Boundary faces are those which belong only to one cell, which can only happen on boundary cells.

The Finite Volume (FV) discretization in OpenFOAM uses some particular data that is extracted from the grid and stored in the *polyMesh* file, which is the simplest mesh description in OpenFOAM. Accordingly, the *polyMesh* class will be extended to *fvMesh* to store other required data for Finite Volume discretization. After *fvMesh* can be constructed from *polyMesh* and it will backlog the data shown in Table 1 and update them during the simulation in case of moving mesh.

Table 1 *Data stored in PolyMesh* (The OpenFOAM Foundation, 2017a)

Class	Description	Symbol	Access function
volScalarField	Cell volumes	V	V ( )
surfaceVectorField	Face area vectors	S_f	Sf ( )
surfaceScalarField	Face area magnitudes	$\|S_f\|$	magSf ( )
volVectorField	Cell centers	C	C ( )
surfaceVectorFiled	Face centers	C_f	Cf ( )
surfaceScalarField	Face motion fluxes	ϕ_g	Phi ( )

4.2.2 Equation Discretization

Equation discretization transforms Partial Differential Equations (PDE) into a set of algebraic equations that are generally represented in matrix form:

$$[A][x] = [b] \tag{83}$$

where x and b are variable and source vectors respectively and A is a square matrix containing a list of coefficients of the desired algebraic equation. FV discretization of each term in the equation is usually defined by integrating the term over the grid volume V and altering it to a surface integral using Gauss's theorem.

$$\int_V \nabla \star \phi \, dV = \int_S dS \star \phi \tag{84}$$

where ϕ represents any tensor field, S is the surface area vector and $\star$ shows any tensor product. After, by using a proper scheme, the surface and volume integrals are linearized. Major functions that are used to discretize PDE terms in OpenFOAM are listed in Table 2.

Table 2 *PDE terms discretization functions in OpenFOAM* (The OpenFOAM Foundation, 2017a)

Term Discerption	Implicit/Explicit	Text Expression	fvm::/fvc:: function
Laplacian	Imp/Exp	$\nabla^2\phi$	laplacian (phi)
		$\nabla.\Gamma\nabla\phi$	laplacian(Gamma, phi)
Time derivative	Imp/Exp	$\frac{\partial\phi}{\partial t}$	ddt (phi)
		$\frac{\partial\rho\phi}{\partial t}$	ddt (rho, phi)
Second time derivative	Imp/Exp	$\frac{\partial}{\partial t}(\rho\frac{\partial\phi}{\partial t})$	d2dt2 (rho, phi)
Convection	Imp/Exp	$\nabla.(\psi)$	div (psi, scheme)
		$\nabla.(\psi\,\phi)$	div (psi, phi, word)
			div (psi, phi)
Divergence	Exp	$\nabla.\chi$	div (chi)
Gradient	Exp	$\nabla\chi$	grad (chi)
		$\nabla\phi$	gGrad (phi)
			lsGrad (phi)
			snGrad (phi)
			snGradCorrection (phi)
Grad-grad squared	Exp	$\|\nabla\nabla\phi\|^2$	sqrGradGrad (phi)
Curl	Exp	$\nabla\times\phi$	curl (phi)
Source	Imp	$\rho\phi$	Sp (rho, phi)
	Imp/Exp		SuSp (rho, phi)

4.2.3 Temporal Discretization

As described, temporal discretization means dividing the simulation time into finite intervals; hence the problem will be solved in each time step. OpenFOAM provides three temporal schemes: Euler implicit, backward differencing and Crank Nicolson. However, currently waves2Foam package works more accurately with the Euler implicit, and it does not offer backward differencing scheme.
The first derivative over a control volume can be approximated merely by Euler implicit as below:

$$\frac{\partial}{\partial t}\int_V \rho\phi\, dV = \frac{(\rho\phi V)^{new} - (\rho\phi V)^{old}}{\Delta t} + O(h) \tag{85}$$

Euler implicit scheme is unconditionally stable but has a global truncation error of order one.

4.3 Interface in OpenFOAM

Although OpenFOAM has an advantage of being free and extensible, it does not have a user-friendly interface. Preparation for the simulation is usually handled through some folders and dictionaries that should be set in an appropriate place. These dictionaries contain information on the initial condition, mesh, schemes, boundary conditions, solvers and all the required variables for the simulation. A general structure of a case is shown in Figure 9.

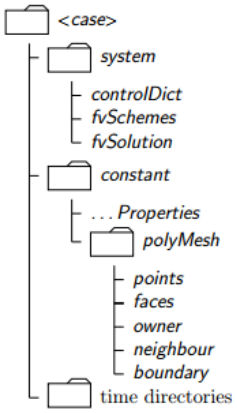

Figure 9 *Structure of a typical case in OpenFOAM* (The OpenFOAM Foundation, 2017b)

It consists of three main folders:

Time Directories: This folder has data from each write interval. At the beginning of the simulation field, the initial condition of the variables and their boundary conditions are defined here.

Constant: This folder usually contains information on the mesh, geometry and other constant properties of the problem.

System: Solution procedure associated parameters such as solver, discretization schemes, time control and so on are stored in this folder. (The OpenFOAM Foundation, 2017b)

4.4 Waves2Foam Toolbox

Waves2Foam is a wave generation toolbox developed by Jacobsen *et al.* (2012) under OpenFOAM software that offers various options for modeling waves, i.e., linear, stream function as well as the possibility to simulate irregular and combined waves. In addition, it provides a relaxation technique to absorb the waves at the domain boundaries to avoid reflection.

In this technique a relaxation function

$$\alpha_R(\mathcal{X}_R) = 1 - \frac{\exp(\mathcal{X}_R^{3.5}) - 1}{\exp(1) - 1} \quad for\ \mathcal{X}_R\ \epsilon\ [0;1] \tag{86}$$

is applied inside a relaxation zone in the following way:

$$\phi = \alpha_R \phi_{computed} + (1 - \alpha_R)\phi_{target} \tag{87}$$

where ϕ is either u or γ . $\mathcal{X}_R$ is defined in a way that α_R always take the value 1 on the border of the relaxation zone and inside the non-relaxed domain i.e. outside the relaxation zone. γ_{target} is the value of the volume fraction of cells in relaxation zones where the analytical waves meet the edge of computational cells. u_{target} is evaluated at the center of the wet part of the intersected cells and is assigned to the computational cell. In an outlet relaxation zone the γ_{target} are obtained based on the still water level position and u_{target} is set to zero. Figure 10 shows a schematic of relaxation zones.

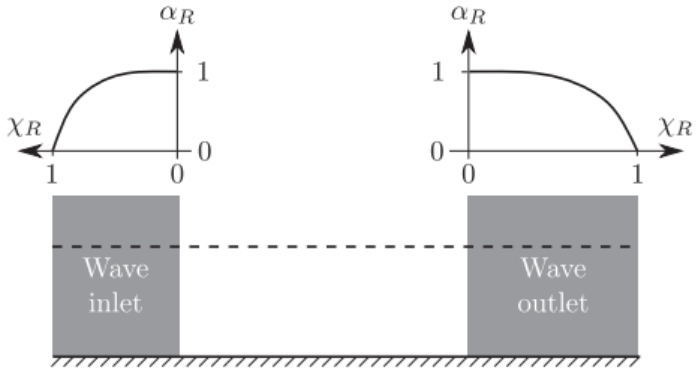

Figure 10 *A schematic of* $\boldsymbol{\alpha_R}$ *variation in relaxations zones (Jacobsen et. a.l, 2012)*

5 Set-up, Discussion, and Results

5.1 Wave Propagation

In the first part, a systematic study of wave propagation in an empty basin is performed. This study aims to understand the effect of grid resolution, cell aspect ratio and time step in wave propagation behavior. This step is the building block of the work because it will provide an overview of what the mesh and time interval should be in a practical simulation. Moreover, it is important to highlight that it will decrease the number of uncertainties and put more confidence in the simulation of a complex problem that involves waves. Interference of the ship wake with the wave train is an easy example. Decay in wave height behind the ship might be due to a destructive interference of waves, or it can be numerical diffusion due to an insufficient number of cells or too large time steps. The number of uncertainties will increase if we consider the appropriate turbulence model and other factors that might affect the results. Therefore, it is necessary to be confident about the accuracy of wave propagation in the domain. However, it is important to note that due to the scope of this master thesis only very limited simulations considering the resources and time are studied.

5.1.1 Set-Up

The studied wave is chosen in a range of ocean waves to represent the real situation that a ship is usually facing. The wave height is set to 2 meters and wave period to 9 seconds.

Table 3 *Wave characteristics*

Wave Type	Wave Height [m]	Wave Period [s]	$\frac{h}{gT^2}$	H/gT^2
Stokes Second	2	9	0.0881	0.00252

The Waves2Foam toolbox described by Jacobsen et al. (2012) is used to model the waves. A numerical wave tank is specified to investigate the effect of cell size and aspect ratio on wave propagation.

Geometry and Meshing

A 2D rectangular geometry is created with OpenFOAM's *blockMesh* utility. The domain length is set to 8 wavelengths to monitor wave dissipation. Water depth is set to 70 meters due to deep water wave range criteria, and 7 meters air above a free surface is considered to have enough distance from the boundary. The free-surface is set to be at zero. A sketch of the geometry is shown in Figure 11.

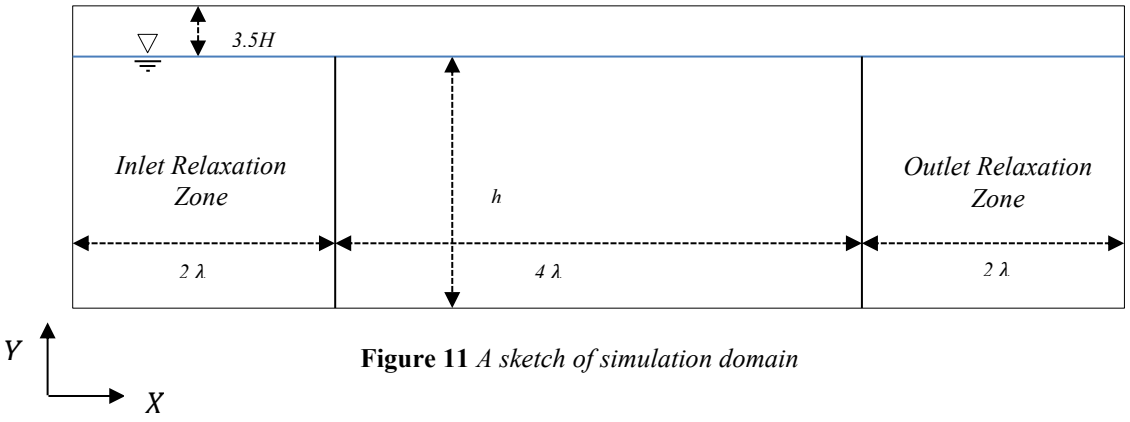

Figure 11 *A sketch of simulation domain*

The geometry is then divided into equal structural hexahedral cells. The first case is defined by four cells in wave height and aspect ratio of 1. Then the grid is refined four times, each time with a factor of square root of two in both length and height directions. To make the comparison easier, each case is named by the refinement level and the base cell is labeled by 1. For instance, X1Y3 case cells are refined two times in height direction, and the cells in wave-length direction did not change. There are 2032 cells in domain length, and 302 in domain height and the total number of cells is 613664. Therefore there are 254 cells in a wavelength and 7.9 cells in a wave height. The aspect ratio of cell is $\frac{x}{y} = 2$. Table 4 shows all the cases. The blue color indicates the number of cells in the x and y directions in domain and red color shows the cell size in each direction compare to original case.

Table 4 *Cases definition, red color represent the refinement level, and blue defines the number of cells in that direction*

			X1	X2	X3	X4	X5
		X	1	1.4	1.96	2.744	3.8416
	Y		2032	2845	3983	5576	7806
Y1	1	154	312928	438130	613382	858704	1202124
Y2	1.4	216	438912	614520	860328	1204416	1686096
Y3	1.96	302	613664	859190	1202866	1683952	2357412
Y4	2.744	423	859536	1203435	1684809	2358648	3301938
Y5	3.8416	592	1202944	1684240	2357936	3300992	4621152

All the cases are done with maximum interface Courant number and maximum Courant number of 0.25 and 0.125, respectively.

Boundary Condition

In OpenFOAM, boundary conditions are set on the patches, i.e. surfaces having specific boundary conditions. Patch names of the physical domain are shown in the picture. All the cases in this section are modeled with same boundary patches and boundary conditions, as well as numerical scheme. Boundary conditions are listed in Table 5.

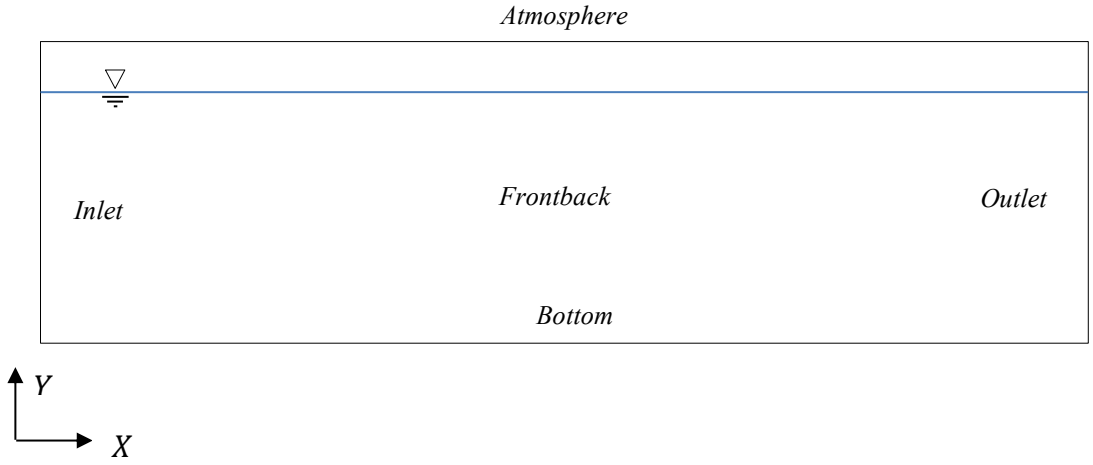

Figure 12 *Domain patch labels*

The flow model is URANS with PISO coupling and laminar characteristic. Euler implicit is used as temporal scheme. The advective term in volume fraction equation is solved with MUSCL scheme for sharp resolution. The limited linear scheme is set to solve the convective term, and linear limited scheme for the diffusion term in Navier-

Stokes equations. *nCorrectors* and *nNonOrthogonalCorrectors* are set to 3 and 1 respectively.

Table 5 *Boundary conditions on patches*

	Volume Fraction	Pressure	Velocity
Boundary patch	$\propto$	P	U
Inlet	waveAlpha	zeroGradient	waveVelocity
Outlet	zeroGradient		fixedValue
Bottom	zeroGradient		fixedValue
Atmosphere	inletOutlet	totalPressure	pressureInletOutletVelocity
Frontback	empty		

Solver and residual tolerances are listed in the table below:

Table 6 *Residual solvers and tolerances*

	alpha.water	p_rgh	pcorr	U
Solver	smoothSolver	GAMG		smoothSolver
Smoother	symGaussSeidel	DIC		symGaussSeidel
Tolerance	1.00E-08	1.00E-07		1.00E-09

5.1.2 Results

Run-Time graph

Taito supercluster is used to run the cases. Taito has two types of nodes:

- Apollo 6000 XL230a G9 server blades, each with two 12 core Intel Xeon E5-2690v3 (Haswell) 2.6 GHz CPUs
- HP ProLiant SL230s servers each equipped with two 8 core Intel Xeon E5-2670 (Sandy Bridge) 2.6 GHz CPUs

All the cases run to 60 wave periods. The simulation time for all cases in comparison to cell size is illustrated in Figure 13. Clearly, the cases with finer grid and lower Courant number took more time to complete the simulation. As it can be seen in the below picture, in logarithmic scale, simulation time changes almost linearly with the cell size. This means the simulation time is proportional to multiple factors in the power of curve slope.

For example, in case of X1Y3, the slope of the curve is 1.47. Therefore, simulation time compare to X1Y1 is

$$T_{X1Y3} \approx (2^{1.47}) * T_{X1Y1} = 2.77 * 19.17 = 53.17\ (h)$$

The slope of the curve in the X direction is around 1.7 and in the Y direction is around 1.47 which means if the number of cells doubles in wavelength, the simulation will increase ~3.3 times and ~2.8 times if it doubles in wave height.

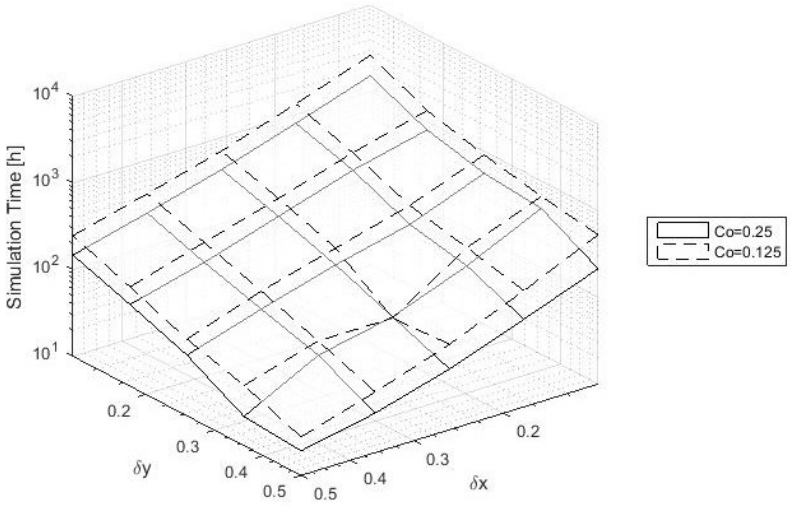

Figure 13 *Runtime graph*

All the cases were compared to ideal Stokes Second wave theory after 20, 40 and 60 wave periods. The picture below shows the first case X1Y1 with maximum Courant number of 0.25. As is evident in the picture, the waves are not only diffused with time, but also some instability starts to grow in the form of ripples mainly at the peaks.

All 50 cases diagrams can be found in Appendix 1**.** Observing the pictures leads to three preliminary conclusions.

Instability

Instability due to time-step

Even though the Euler temporal scheme is of order one global discretization error, it is still the best option that works with Waves2Foam package. Therefore the time-step should be sufficiently small to insure the stability and also the accuracy of the solution. It can be seen in other cases like X1Y2, X2Y1, X1Y3, X2Y2, and X3Y1 at maximum Courant number of 0.25.

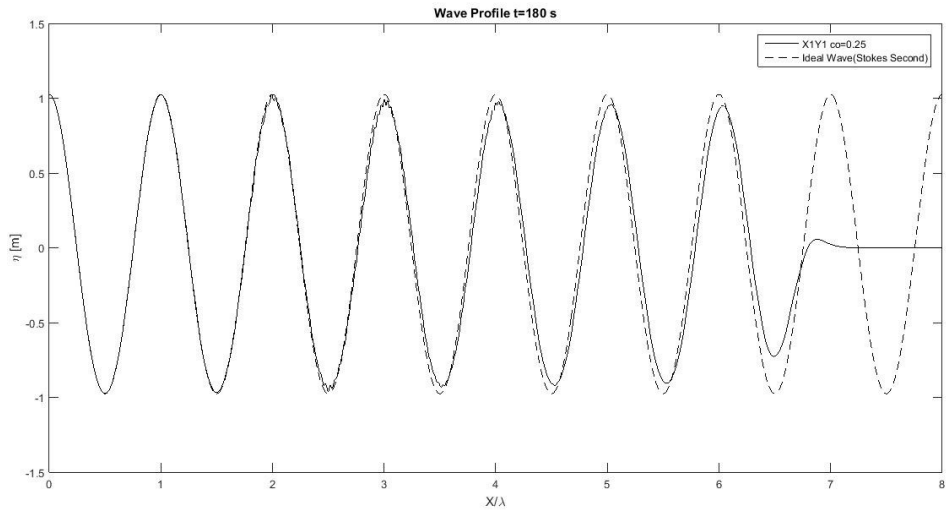

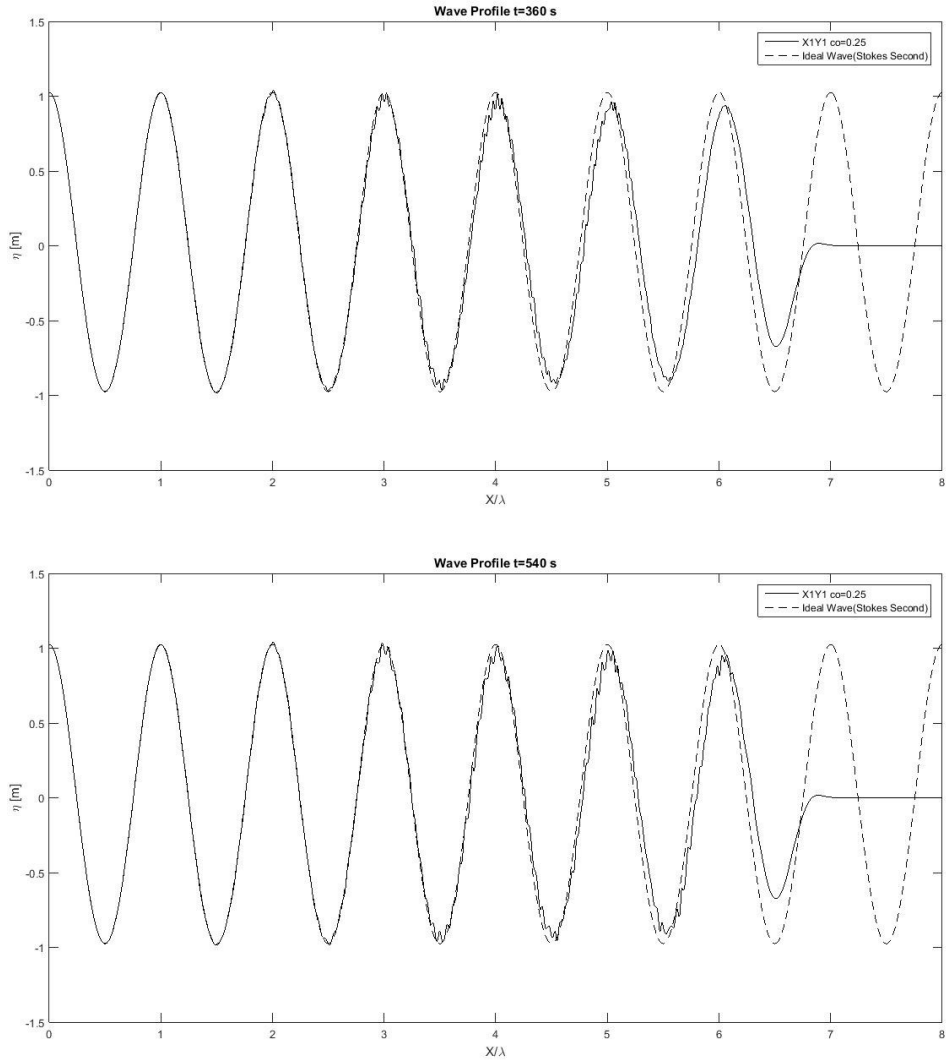

Figure 14 *Ripples on wave profile: case X1Y1 at t=20, 40 and 60 T*

Instability due to tall cells

Another type of instability is observed which occurs when the cells are tall. ($\frac{y}{x} > \sim 2$). This is in line with previous studies (Roenby *et al.* 2017).

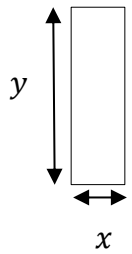

Figure 15 *A schematic of a tall cell*

Example of these instabilities are X4Y1, X5Y1 with maximum Courant number of 0.25 and X5Y1 with max Co=0.125. Instability might also be caused by both of these factors. Figure 16 shows case X5Y1 with max Co=0.125.

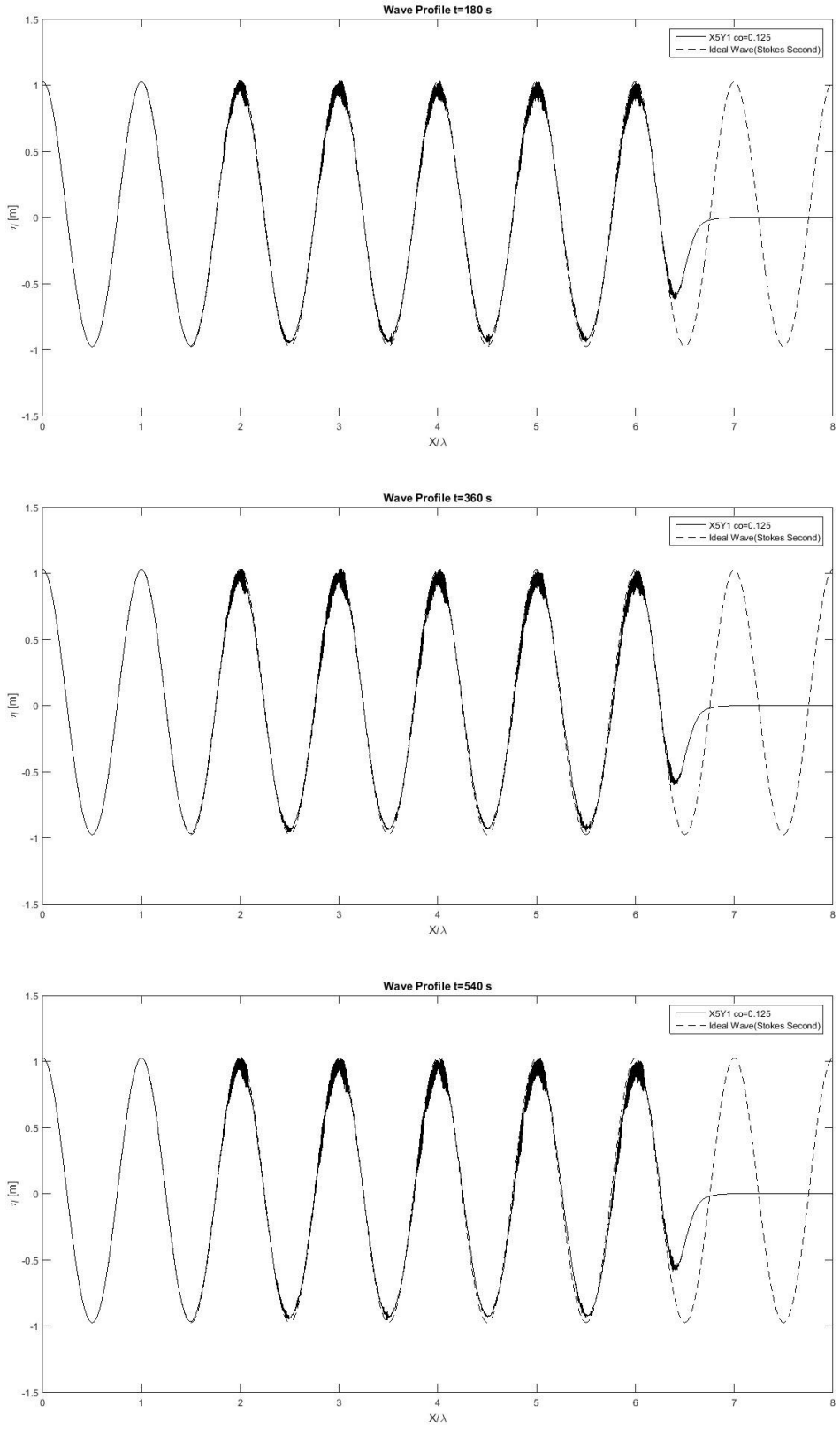

Figure 16 *Instabilities due to tall cells: case X5Y1 at t=20, 40 and 60 T*

Wave decay and Phase shift

Another preliminary observation from the pictures is that waves not only decay with time but also decay along the domain. In addition, a phase shift is seen along the numerical wave tank. This phenomenon is more pronounced with time procession.

Figure 17 compares the wave profile of X1Y1 and X5Y1 which has 4 times more cells in the wavelength direction.

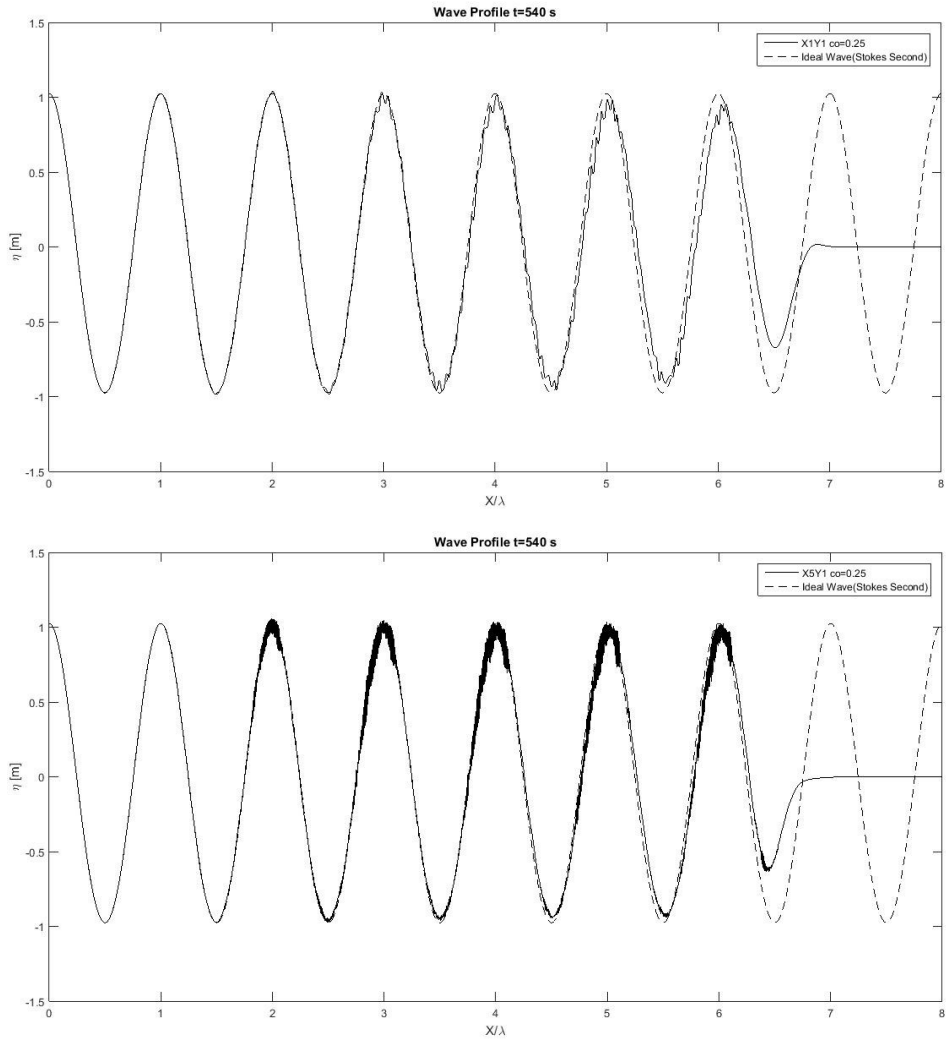

Figure 17 *Phase shift comparison between case X1Y1 and X5Y1 at t=60T*

It is easy to see that the error due to phase shift is more in the X1Y1 case which has fewer cells in wavelength. This proposes that wave shift is a function of number of cells in wavelength. Also, comparing cases X1Y1 in Courant number 0.25 and 0.125 and X1Y5 in Courant number =0.25 which has the same number of cells in wavelength shows time-step is another dependent factor in phase shift. Since the Courant number for both cases are the same, therefore the case with finer mesh should have lower time-step compare to the case with the coarser grid. Conclusively, X5Y1 case uses both advantage of more cells in wave-length and lower time step.

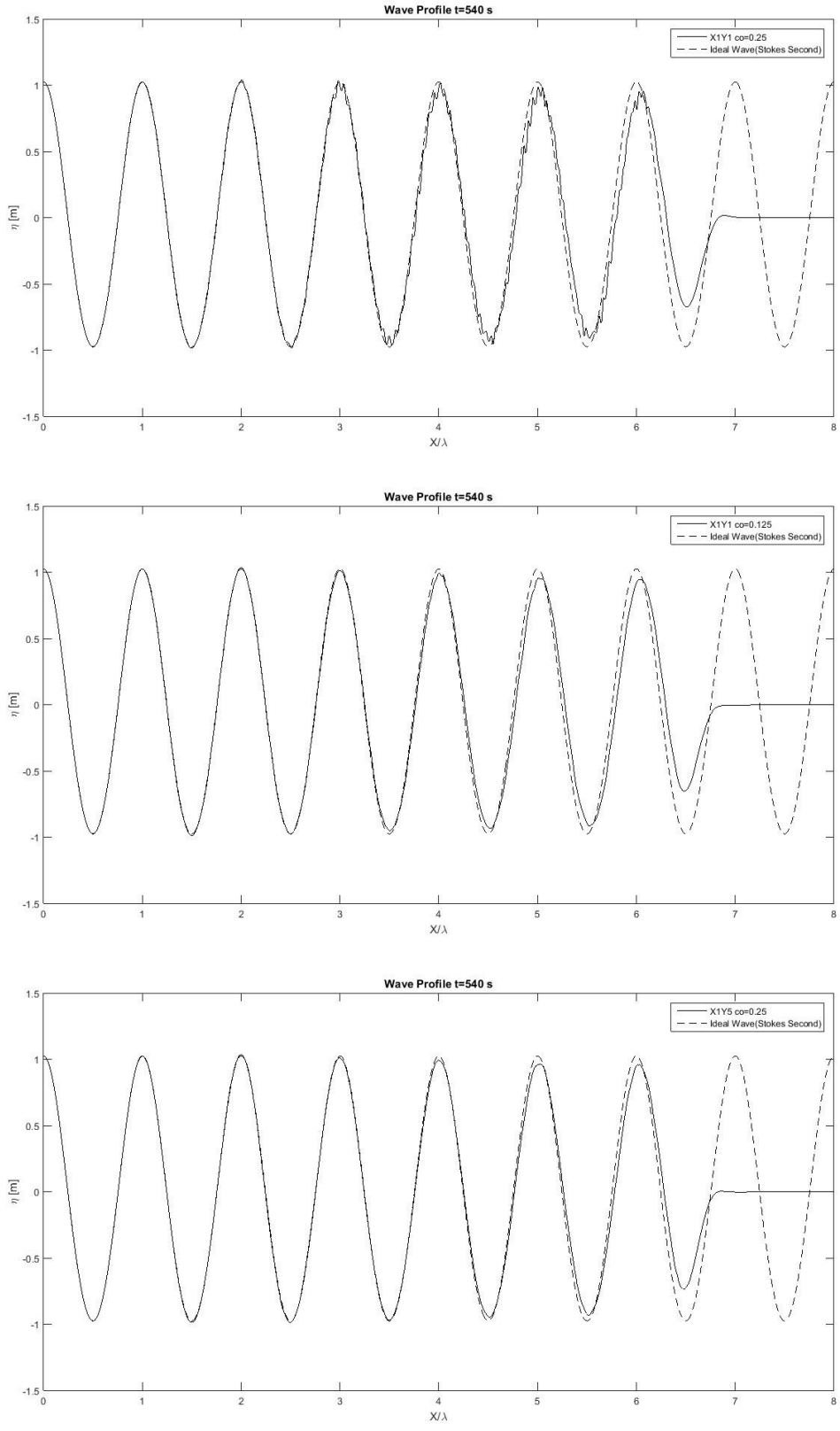

Figure 18 *Phase shift comparison between cases X1Y1 Co=0.25, X1Y1 Co=0.125 and X1Y5 Co=0.25*

Although the pictures were qualitatively fruitful, not much can be captured by human eyes, and therefore results should be analyzed quantitatively as well. To do that five equally spaced wave gauges were mounted from the end of the inlet relaxation zone to the beginning of the outlet relaxation zone with one wavelength distance to capture the wave elevation.

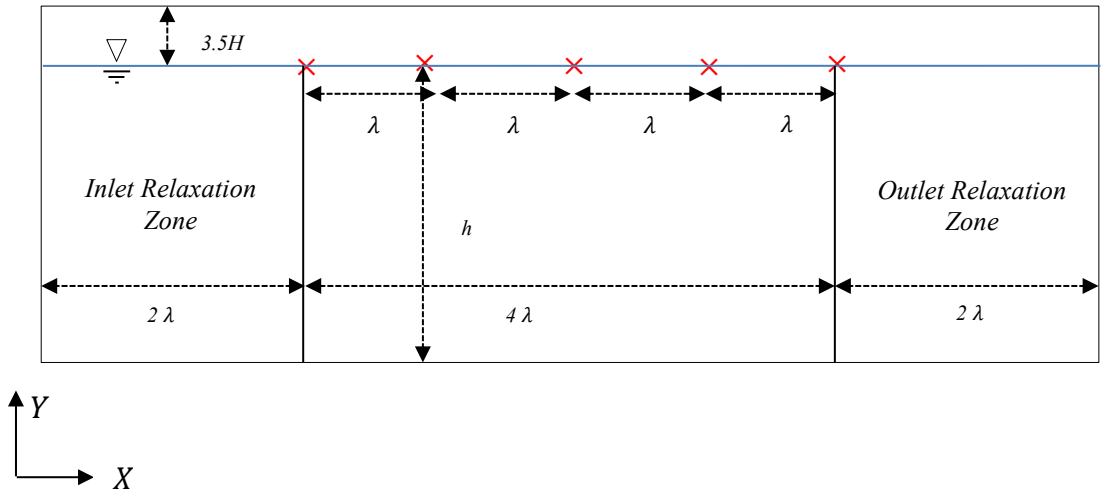

Figure 19 *A sketch of wave gauges positions*

Fourier Analysis

Fourier transform is a tool that expresses a function of time with the frequencies that produce that function.

Before discussing the results, some facts about the data and its limitations should be explained.

First, data is recorded at each time step. The time step control is handled by setting a maximum Courant and maximum interface Courant number. Therefore time intervals were varied slightly through the simulation time by the change in local velocity, for example. However, Fourier transform analysis requires that data be equally spaced in time; thus, a spline function is used to match the limitation. In addition, it allows sampling the data at the desired number.

Second, waves start to propagate from the inlet at the beginning of the simulation. Therefore there is a particular time required for the waves to reach each wave gauge.

$$t = x/c$$

where x is the distance from inlet, c is the wave celerity and t is the required time for the wave to reach a certain point. Therefore, considering the data before that time will cause wrong results.

Third, although relaxation zones are implemented to absorb the reflected waves, small reflections might happen at the boundary of relaxation zones. Therefore, the time between the incoming and reflected wave from the outlet boundary to reach the wave gauge should be considered for FFT to have more accurate results. However, if we only consider this, the wave gauges which are closer to the outlet boundary will not have enough wave periods to apply Fast Fourier Transformation. Watching the wave during a wave period shows the reflection influence is small and therefore in order to have a more-or-less similar situation for all the wave gauges the time after the reflected wave reaches all the wave gauges is considered for Fast Fourier Transformation analysis.

Fourth, at least 10 stationary periods of data is used for the assessment.

Wave Gauges Energy Spectrum

Energy spectrums were pictured for all wave gauges in all the cases. Picture below shows case X1Y1 in two Courant numbers 0.25 and 0.125. As it can be seen the numerical model captured the existence of harmonics in the implemented Stokes wave. Results for all cases can be found in Appendix 1.

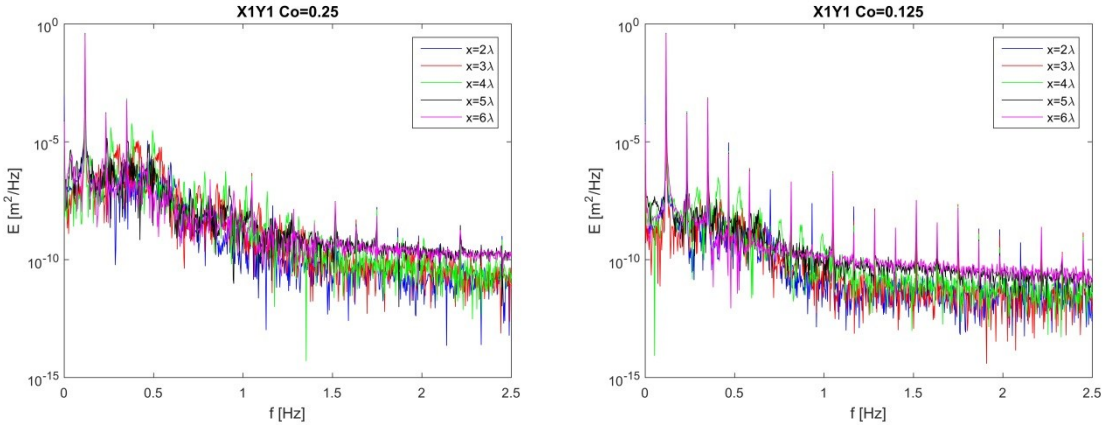

Figure 20 *Fourier analysis of cases X1Y1 Co=0.25 and X1Y1 Co=0.125*

The energy level of the first harmonic for each wave gauge with different cell size in x and y direction is plotted in both maximum Courant number of 0.25 and 0.125 in the figures below. To have a more sensible comparison, all the cases with notable ripples were eliminated from the graphs. As evident, increasing the number of cells in the wavelength direction does not have a significant influence on wave energy levels. The reason for this is simply because the wave steepness is quite low and therefore the number of cells along the wavelength is much higher compare to wave height due to aspect ratio below 4. In the first case, the number of cells in the wavelength is 254. In contrast, the number of cells in the wave height has a considerable effect on the energy level.

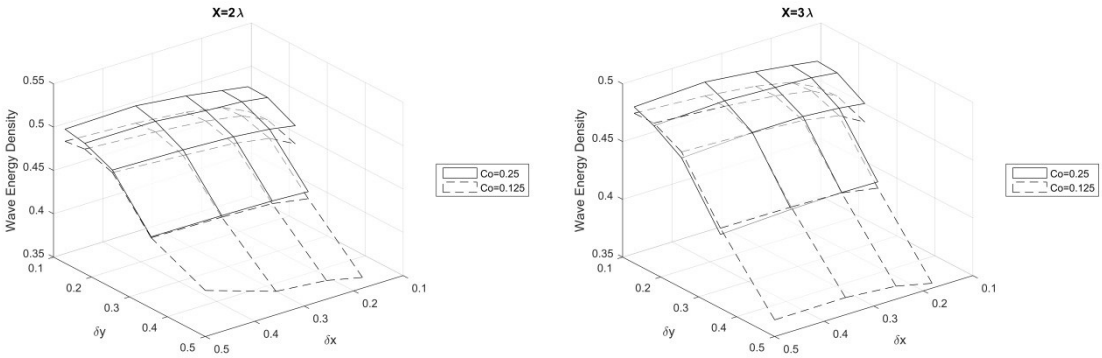

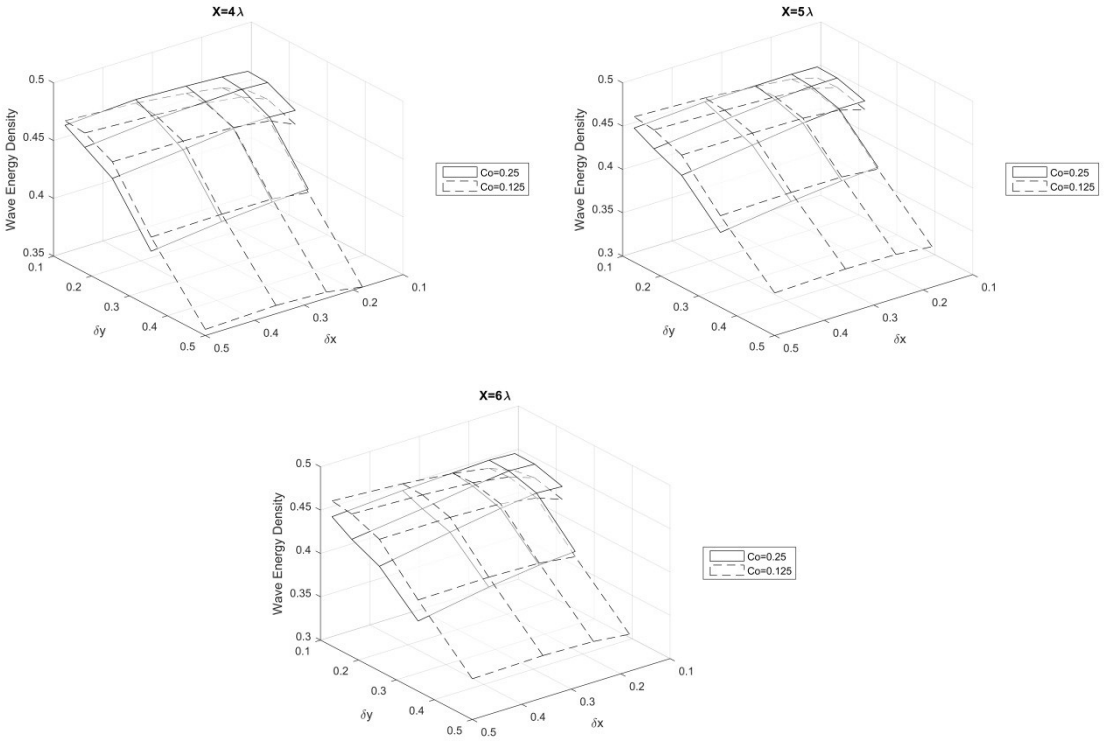

Figure 21 *Wave Energy change with grid resolution in different wave gauges*

Although it was expected that cases with lower Courant number result in higher or at least similar energy levels compared to higher Courant number cases due to less temporal error, in some cases, mainly with the finer grid in x direction, Courant 0.25 has higher energy level according to graphs.

One possible explanation can be that cases with finer mesh are experiencing more reflection which causes higher or lower amplitudes compared to coarse cases which affect the results. To investigate that, only the part of the data that wave gauges experiences without reflection is considered. Since wave gauge 3, 4 and 5 experience less than 10 periods without reflection, the analysis is done only for the first two wave gauges. Figure 22 shows the energy level of first harmonic for these gauges.

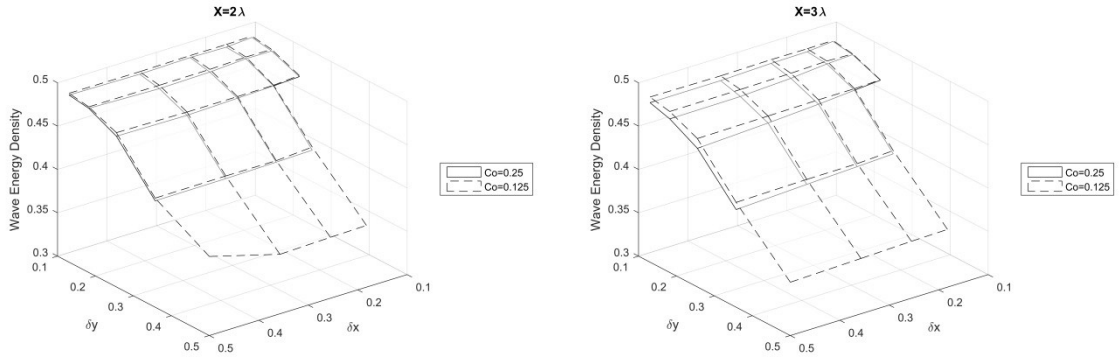

Figure 22 *Wave energy variation with grid resolution without reflection effect*

As shown, the unexpected results vanished which confirms that reflection was the probable source of error. It can be seen also that at the beginning of the domain the energy is a function of the number of cells in the wave height only.

Next, in order to see the effect of cell size on propagation dissipation in space, wave energy of the first harmonic is plotted along the domain for different cell sizes. It is observed previously that wave energy in space is mostly a function of the number of cells over the wave height. However, the rate of change in the energy level in each case along the domain shows a minor effect with this factor, approximately 1%. On the other hand, the number of cells per wavelength was found to be more influential, with approximately 5% dissipation. As demonstrated in the figure below, clearly the wave decays faster in x-wise coarser grids.

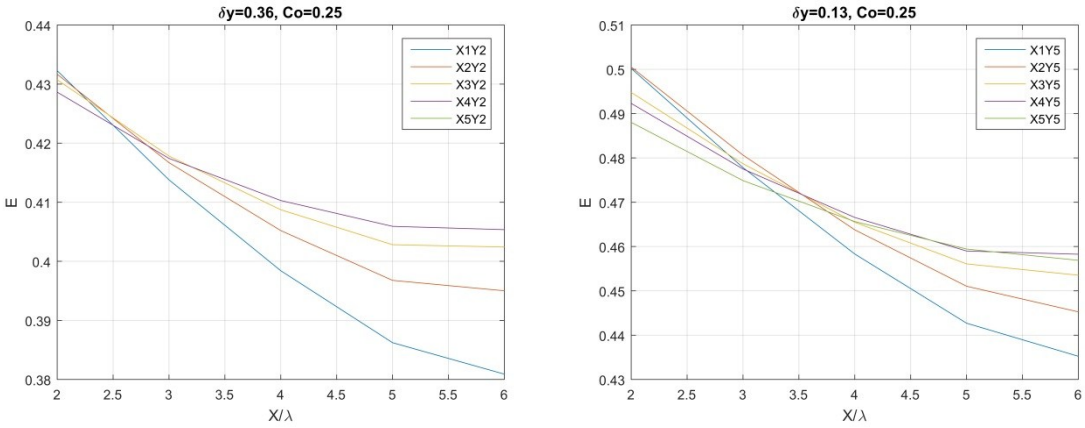

Figure 23 *wave dissipation along the domain with wavelength grid resolution*

Afterwards, an exponential function in MATLAB is fitted to data to represent the upper bound envelope of waves along the domain.

$$E = a + b * \exp\left(-c * \left(\frac{X}{\lambda}\right)\right) \tag{88}$$

Where E is the energy of first harmonic; X is the distance from inlet and λ is the wave length.

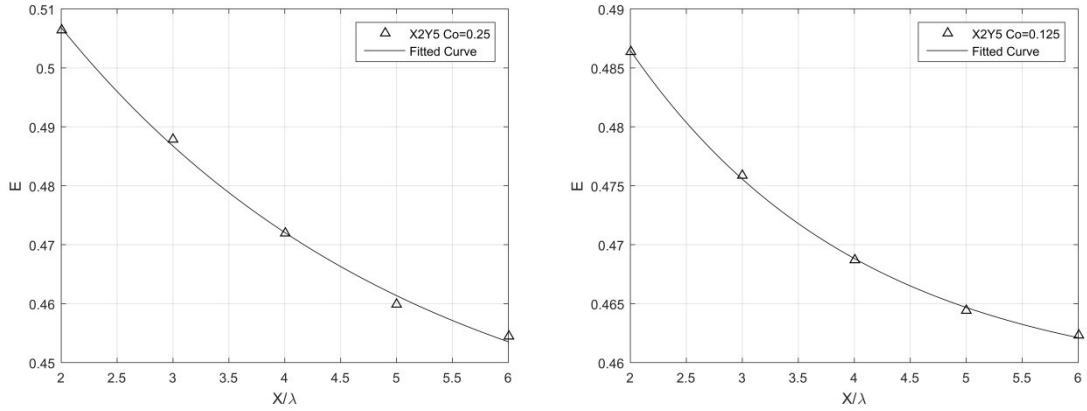

Figure 24 *Exponential curve fitting on wave dissipation along the domain*

According to this formula, energy will decay faster with higher $b * \exp\left(-c * \left(\frac{X}{\lambda}\right)\right)$ term where the term c is the exponential decay factor. This term is plotted for all the cases. However, cases with lower Courant number did not show meaningful trend which is probably again because of reflected wave interference with the original wave. Figure 25 illustrates the dissipation term for Co=0.25 cases.

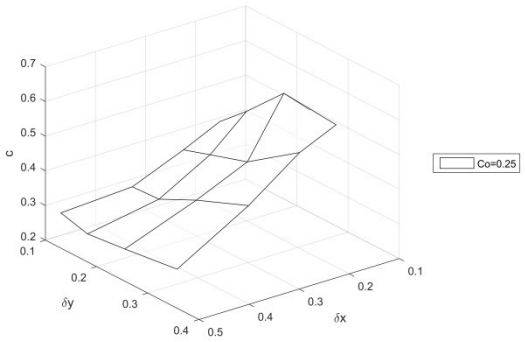

Figure 25 *Wave dissipation term with grid resolution*

It can be seen the decay term increases significantly with cell size in wavelength direction as predicted before.

Phase Shift

The phase shift is calculated by the zero crossing of the wave profile at the end of the simulation time.

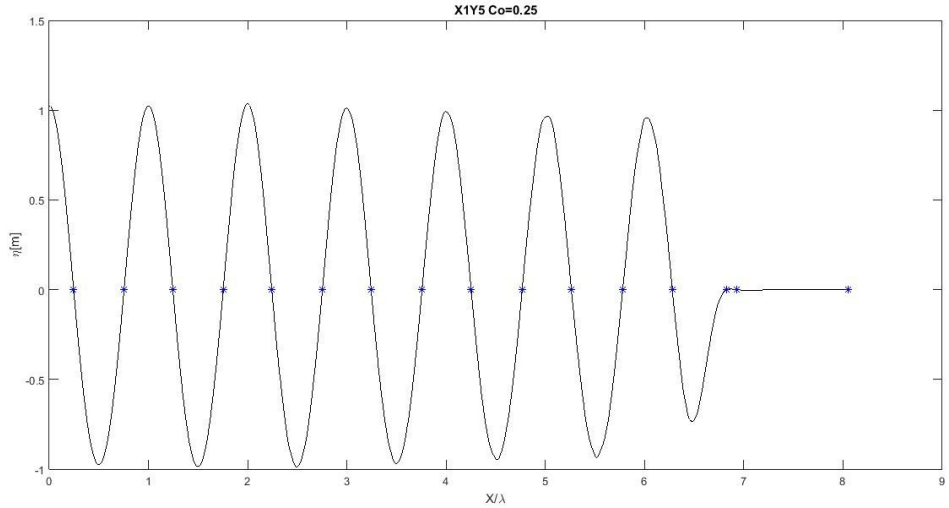

Figure 26 *A schematic of wave profile zero crossing*

It was previously understood that phase shift is mainly a function of cell size in wave-length direction and also time-step. Therefore, λ is plotted along the domain against grid size in X direction and at both Courant numbers.

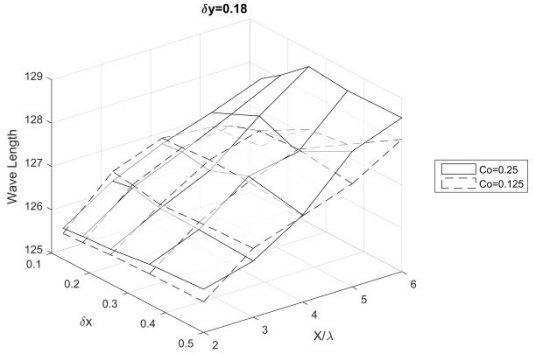

Figure 27 *Phase shift along the domain in different wavelength resolution*

As evident, the wavelength increases almost linearly over the domain. However, it is not easy to see the influence of cell size. To have a closer look on the cell size effect, only the gauges in the beginning and end of the domain are considered and the shift percentage from the original λ is plotted for a fixed δy. Similar $x-$wise grid size is shown with the same color. The solid lines represent Courant=0.25, and the lower Courant cases are shown with dashed lines.

As can be seen, the phase shift increases with a coarser mesh and higher time step. To have a holistic comparison between all the cases the slope of the curves are plotted against the cell size in Figure 29.

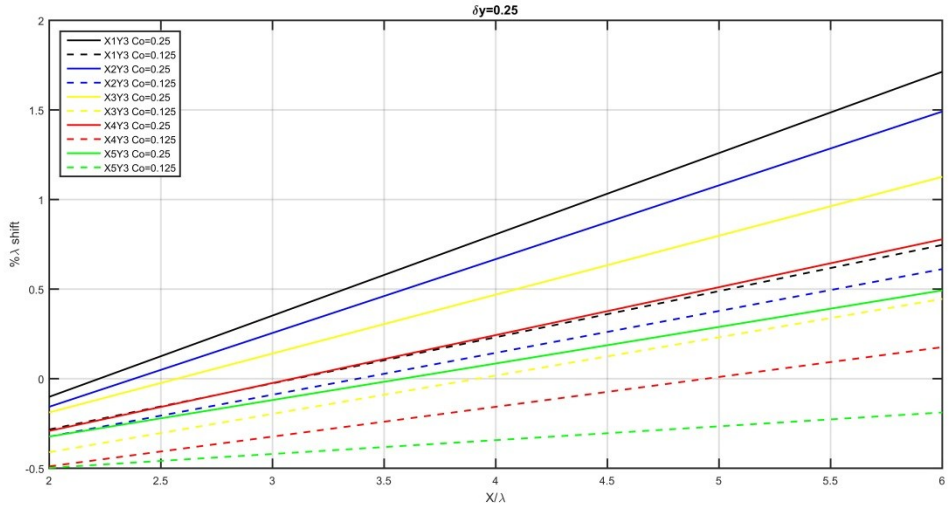

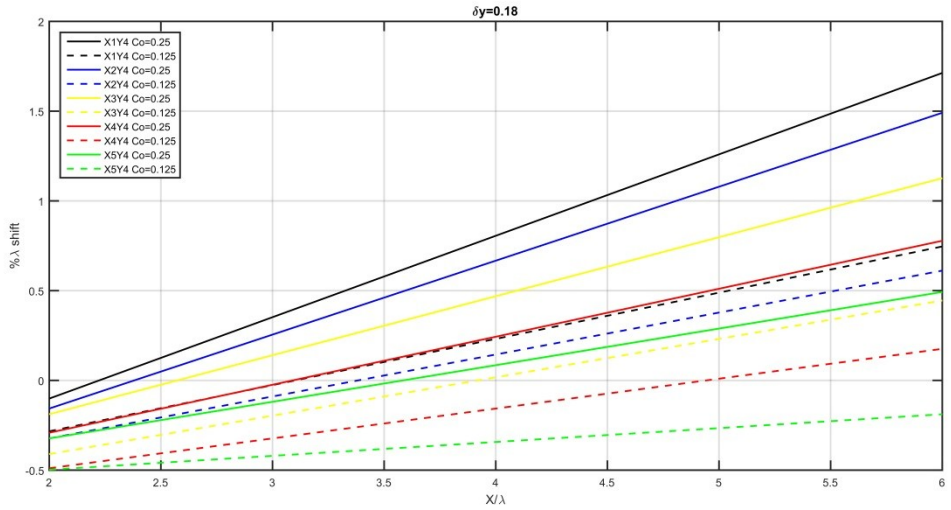

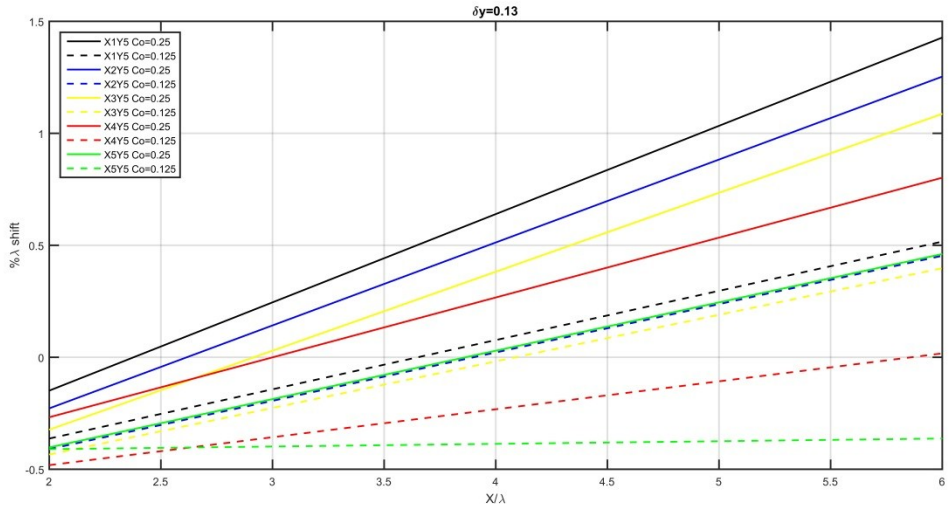

Figure 28 *Phase shift along the domain at different wavelength resolutions and Courant numbers*

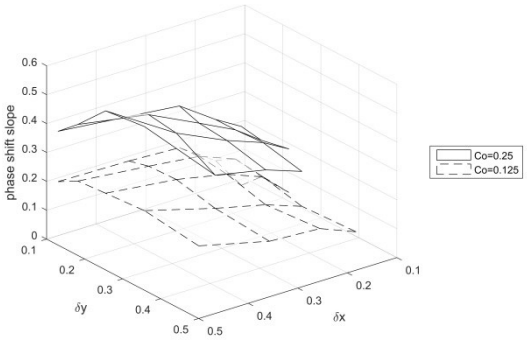

Figure 29 *Slope of phase shift with grid resolution*

From the picture, it can be seen that the slope is decreasing in finer grids. Moreover, it is evident that effect of the time step is more pronounced. This is probably because the grid in $x-$ wise direction is already very fine for all the cases.

5.2 Wave Load on Cylinder

In the previous section, wave propagation in 2-D was examined. It is understood that long cells do not have a noticeable effect on results, but tall cells will cause instability and ripples. A denser grid over the wave height will give better results. Moreover, a lower time step and a finer grid in wavelength will decrease the phase shift and diffusion.

In this part, a fixed cylinder in head waves is modeled, and the drag force is obtained. The aim of this part is first to move from a 2-D wave tank to a 3-D wave tank; second to observe if the correct wave propagation would result in accurate loading or not and also to examine the impact of different wave energy on wave loading.

5.2.1 **Set-Up**

This follows an experiment performed at Danish Hydraulic Institute (DHI) in the wave tank ($35\,m \times 25\,m$) and $0.505\,m$ depth (Zang *et al.*, 2010a ;2010b). The wave and cylinder characteristics are listed in the table below:

Table 7 *Wave and cylinder characteristics*

Wave Type	Wave Height [m]	Wave Period [s]	Cylinder Radius [m]	Cylinder Height [m]	$\frac{h}{gT^2}$	H/gT^2
Stokes Second	0.07	1.22	0.124	0.466	0.0346	0.0048

Geometry and Meshing

Chen *et al.* (2014) also used OpenFOAM to simulate the experiments and concluded that OpenFOAM is very capable of modeling this type of problems. The domain is reproduced utilizing his idea. A top view of the numerical wave tank, as well as the relaxation zones, is illustrated in Figure 30. Domain height is 1.1 m which is divided in half to air and water.

Two scenarios are considered: four and eight cells over the wave height. From the last part of this thesis, it is understood that after 60 periods the difference in the amount of energy between the wave with eight cells in the wave height in comparison with the wave with four cells in weight height could be around 6%. However, it is expected the difference after 25 periods would be lower since longer simulation time will lead to more substantial errors due to reflection effects. Moreover, it should be highlighted that cell sizes are much smaller than in the previous part of this work ($\sim 30\ times$), due to the difference in the nature of the problem, therefore Co=0.25 will result in much smaller time step than that used in the 2D case.

Table 8 *Case definitions*

Case	n/λ	n/H	x/y	z/y	Max Co	Run Time
1	120	4	1	22.8	0.25	25T
2	120	8	2	45.7	0.25	25T

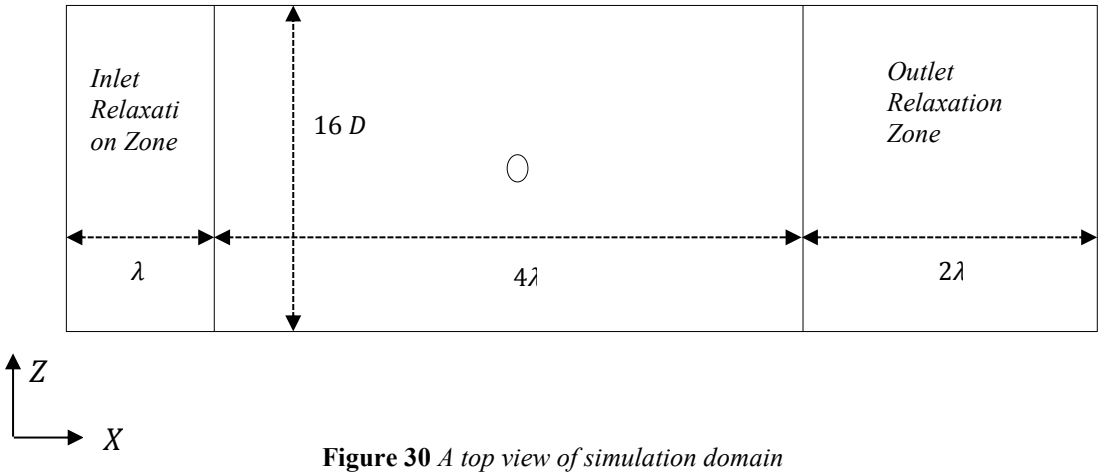

Figure 30 *A top view of simulation domain*

The domain is discretized with the *blockMesh* utility to hexahedral cells and refined 6 times around the cylinder location. *snappyHexMesh* utility is used to extract the cylinder geometry in the domain.

Boundary Condition

Reynolds number around the cylinder is 4.6×10^5 considering the wave celerity which is lower than the transition Reynolds number($\sim 5 \times 10^5$). Consequently, the flow is set to be laminar.

Boundary patches were named similar to the previous 2D case. Since the geometry was 3-D, one side is named frontback1 and the other side named frontback2. All the boundary conditions are listed in Table 9.

Table 9 *Boundary conditions on patches*

	Volume Fraction	Pressure	Velocity
Boundary patch	$\propto$	P	U
Inlet	waveAlpha	zeroGradient	waveVelocity
Outlet	zeroGradient		fixedValue
Bottom	zeroGradient		fixedValue
Atmosphere	inletOutlet	totalPressure	pressureInletOutletVelocity
Frontback1	zeroGradient		fixedValue
Frontback2	zeroGradient		fixedValue
Cylinder	zeroGradient		fixedValue

The same numerical schemes and solvers as the 2D case are used to model the problem.

5.2.2 Results

Taito supercluster is used to run the cases. After 25 periods passed, convergence histories of drag forces in both cases are plotted.

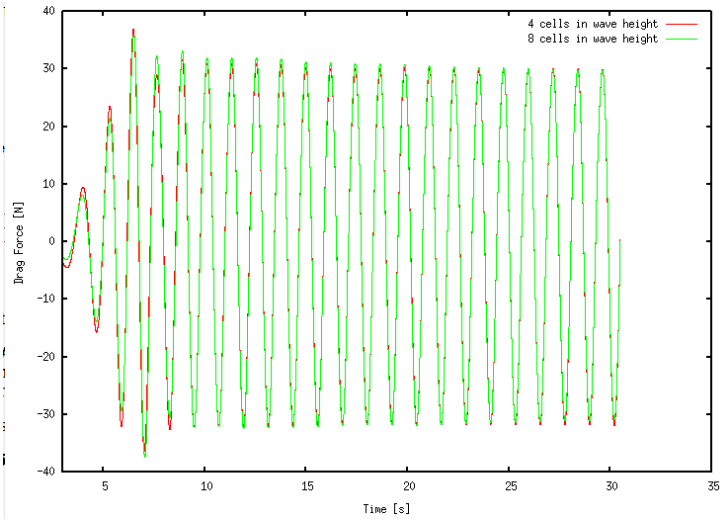

Figure 31 *Drag force history of cases*

As is evident from the plot, both cases show similar behavior after a certain amount of time. To compare the results with (Chen *et al.*, 2014), Fourier analysis of drag forces on

the cylinder were performed. Results show a difference of ~ 1.5% for case 1 and less than 1% for case 2 in comparison with Chen's results, which were perfectly matching the experimental data.

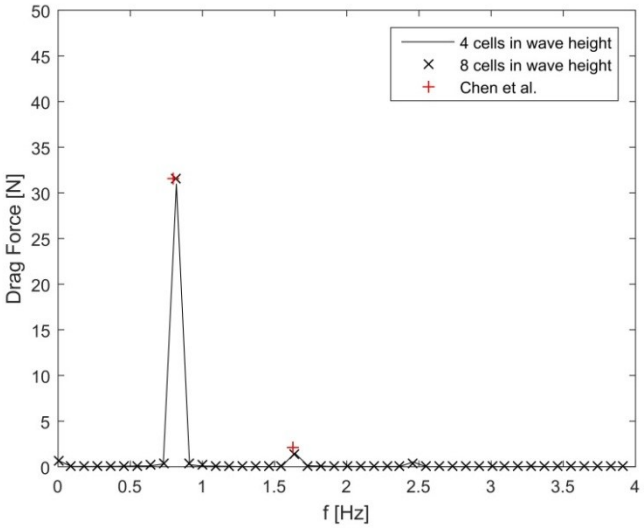

Figure 32 *Fourier analysis of drag forces on cylinder*

From the result, it is found that the numerical model is capturing the main features of wave interaction with the cylinder, which resulted in the correct magnitude and period of wave loads. Moreover, from the graph, it can be seen that major existing harmonics are captured.

Another important point that should be noted was that these results were obtained with very few cells in *z* direction which caused a high z/y aspect ratio. This is mostly because far from the cylinder there is no change in the flow field along the x direction. In any case the results confirmed these large aspect ratios are not problematic.
The free surface elevation is illustrated below to show the flow field around the cylinder in both crests and troughs.

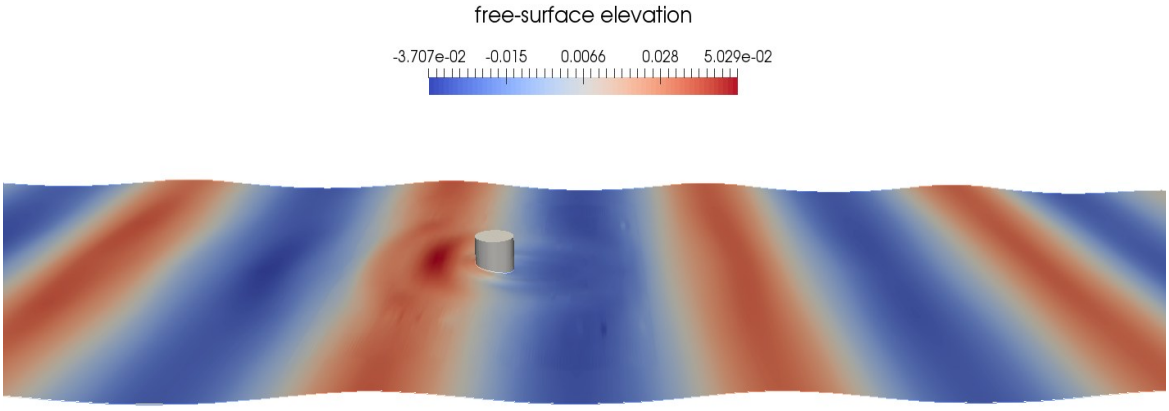

t=29.6 [s]

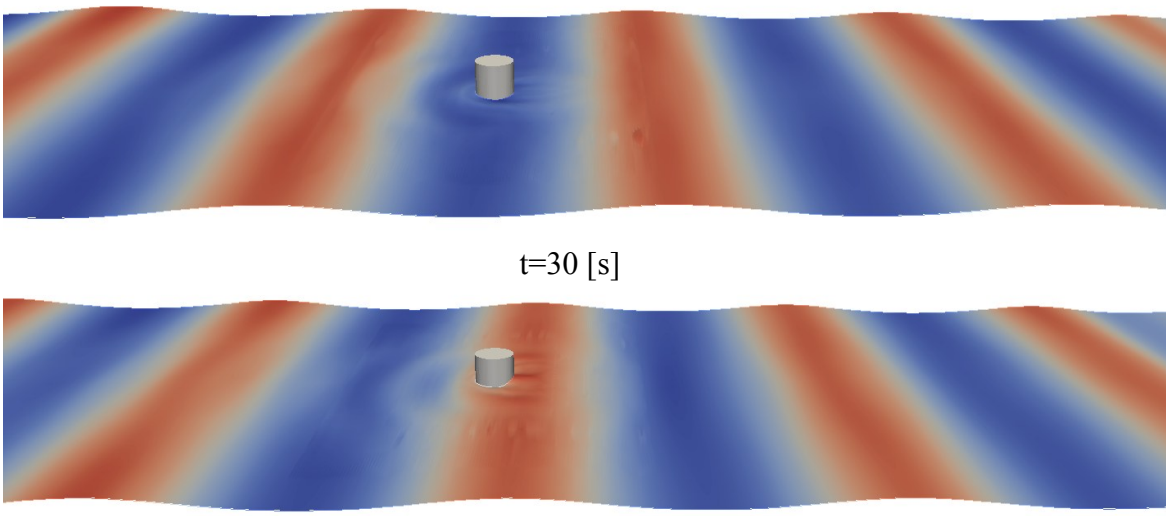

Figure 33 *Cylinder in crest and through*

5.3 Simulation of Ship with Forward Speed in Head Waves

Completing the preliminary steps, it is understood that long cells in wavelength direction and also in the third dimension do not have a negative effect on the results. In addition, it is observed that even with four cells in the wave height, the load can be predicted with less than 2% error when the time step is sufficiently small.

In this section, utilizing all remarks, a ship with forward speed subjected to head waves will be simulated in model scale, and ship motions will be validated with experimental data. Later, a 5 times larger scale, considering resources and simulation time, is modeled, and results are analyzed against the smaller scale to study the scale effect.

5.3.1 Ship and Wave Characteristics

The studied wave and ship features are listed in Table 10.

Table 10 *Ship and wave characteristics*

Ship Type	Lpp [m]	Draft [m]	Breadth [m]	C_b	Ship Speed [kn]	Model Scale
Cruise	315	9.2	45.4	0.715	17.9	50.83
Wave Type	Wave Height [m]		Wave Period [s]		$\frac{h}{gT^2}$	H/gT^2
Stokes Second	4.12		13.09		0.1512	0.00245

5.3.2 Set-Up

Geometry and Meshing

The domain is designed in a way that:

- There would be at least two ship length distances from the front and back of the ship to inlet and outlet.
- Domain depth would not change the wave number
- There would be enough distance from free surface to atmosphere
- Length would be enough for wave propagation

With this consideration, following domain is produced.

Figure 34 shows the side and top view

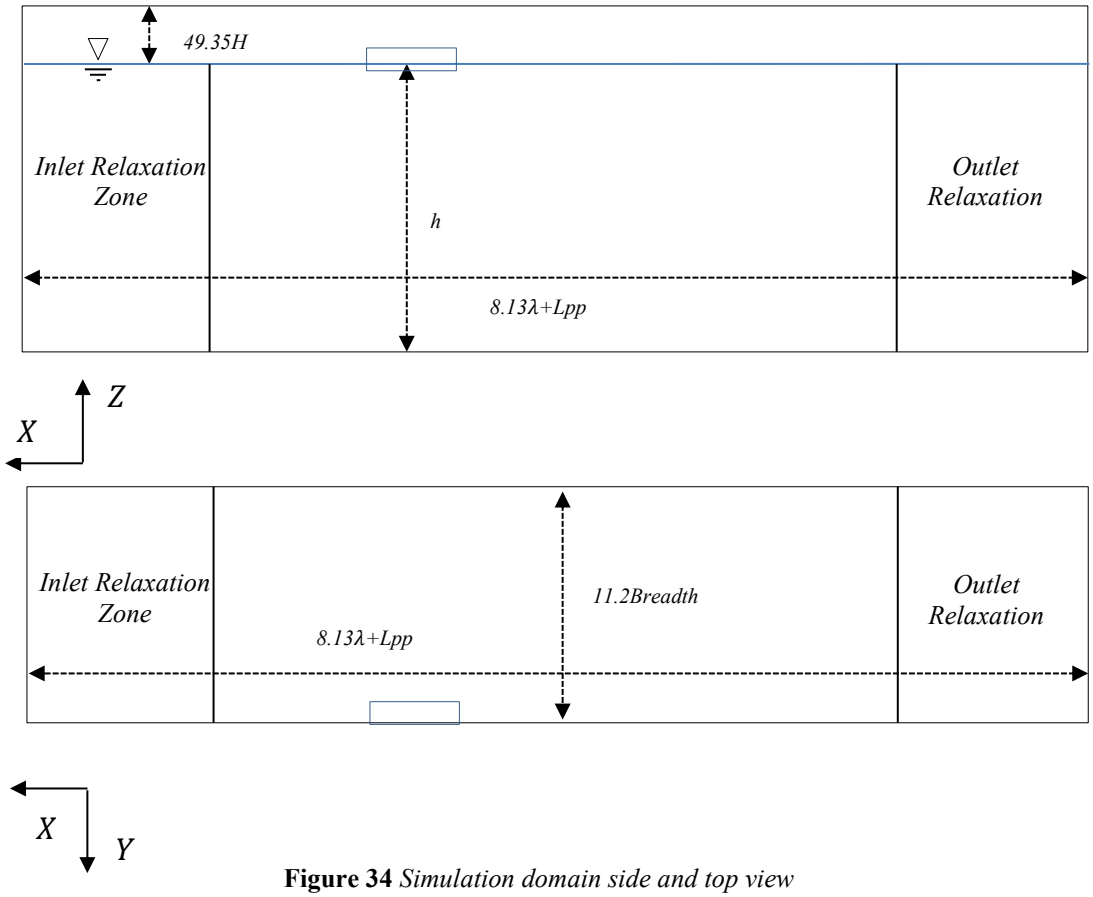

Figure 34 *Simulation domain side and top view*

Meshing is done considering the following factors:

- At least 4 cells in wave height should exist based on the observed results from previous parts
- According to a study by (Windén, 2014), the number of grids in wavelength should be at least 60 to avoid mesh dependency and high dissipation.
- The mesh should be fine enough around the ship to capture the flow field correctly, especially when there is a sharp change in geometry, e.i. bow and skeg
- Number of cells should be practical
- Tall cells should be avoided
- Transition between cell sizes should be smooth
- Depending on utilizing wall functions or not, an appropriate y^+ should be set around ship.

Based on this criteria the mesh was optimized, and finally, the following numbers were obtained:

Cells/wave height	Cells/wavelength	Number of cells
4.9	84.2	2957187

The mesh generation process is started with a background mesh in *blockMesh* utility, and the domain is divided into six blocks along the vertical direction:

Block one: from bottom to 3 meters below ship
Block two: from 3 meters to 2 meters below ship
Block three: from 2 meters below ship to free surface
Block four: from free surface to 0.6 m higher
Block five: from top of block four to 1 meter higher
Block six: from top of block five to atmosphere
A sketch of this division can be seen in Figure 35.

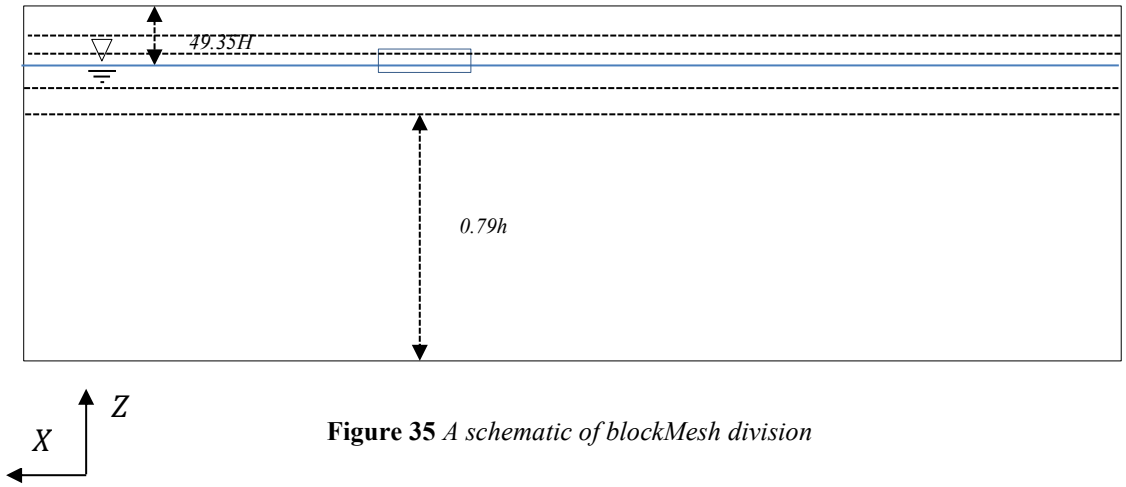

Figure 35 *A schematic of blockMesh division*

The reason for this division is to have enough cells in the wave propagation area and to have a smooth transition to the farthest parts.

To take into account the practicality of cell numbers, very few cells are considered in the x and y directions. However, to have enough cells per wavelength and around the ship, the mesh is refined six times from inlet to one wavelength after the ship in these directions using *topoSet* utility.

Figure 35 shows a top view of refinement reigns.

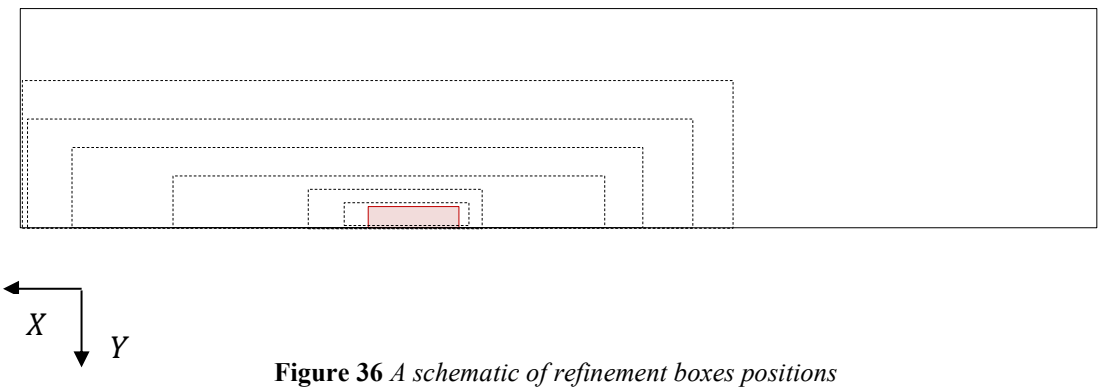

Figure 36 *A schematic of refinement boxes positions*

Next, *snappyHexMesh* tool is used to extract the geometry and create the desired y^+ value. This process is repeated many times with different background mesh and refinement regions to find a practical number which fulfills the criteria and required quality.
An overview of the mesh is illustrated in Figure 37.

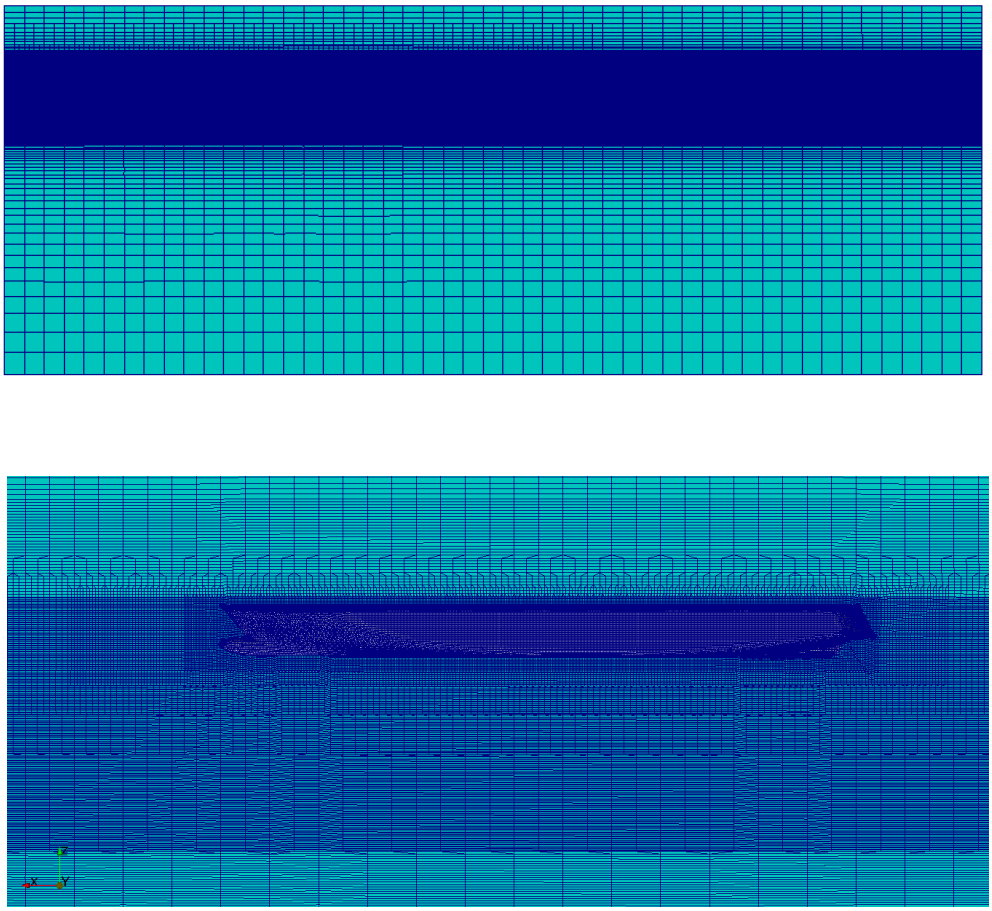

Figure 37 *Grid around the ship*

After producing the appropriate grid, three other cases are defined refining the grid over the wave height by a factor of square root of 2 to examine the grid independence of the solution. Therefore four scenarios are considered:

Case	Cells/wave height	Cells/wavelength	Number of cells
1	4.9	84.2	2957187
2	6.8	84.2	3916092
3	9.9	84.2	5174318
4	13.5	84.2	7128524

Dynamic Mesh Handling

Although the laboratory test is modeled with six degrees of freedom, following the literature (Kent, 1922, 1924; Havelock, 1940) only heave and pitch, which are the dominant motions, are set free to avoid complexity and instability in the problem. To increase the stability, translational and rotational dampers with the value of 18 times ship mass and inertia respectively is considered to control the excessive motions.

OpenFOAM also allows specifying a mesh motion region with *innerDistance* and *outerDistance* parameters. In *innerDistance* region, anything will directly move with mesh nodes as a rigid body. Between *InnerDistance* and *OuterDistance* the mesh nodes are morphed. Moreover, outside the *outerDistance* region the mesh is static. Inner and Outer Distances are set 0.2 and 1.2 respectively in the model scale. In the bigger scale, the values increased with the scale ratio.

Turbulence Modeling and Boundary Conditions

Boundary patches side view of the model is visualized in Figure 38. To capture the turbulent features of the flow, $k-\omega\ SST$, turbulence model is utilized. y^+ value is set to be 100 around the ship. The same numerical schemes and solvers as in the previous sections are used to solve the flow field, plus the linearUpwind scheme for advective terms in k and ω equations.

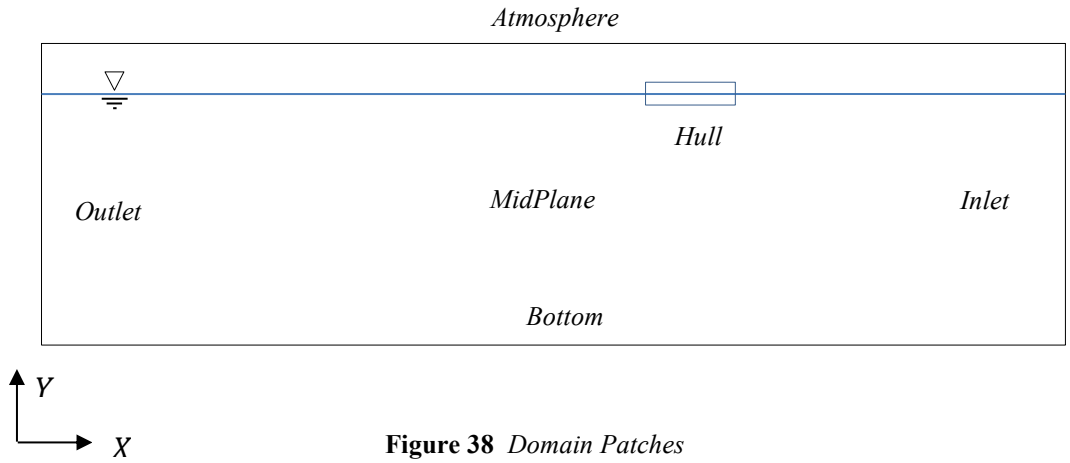

Figure 38 *Domain Patches*

Boundary conditions and solvers are listed in Table 11 and Table 12 respectively.

Table 11 *Boundary condition on patches*

	Volume Fraction	Pressure	Velocity	Turbulence-Intensity	Turbulence - Dissipation Rate	Turbulence-Viscosity
Boundary patch	$\propto$	P	U	k	ω	ν_t
Inlet	waveAlpha	fixedValue	waveVelocity	fixedValue		
Outlet	zeroGradient	fixedValue	zeroGradient	zeroGradient		
Bottom	symmetryPlane					
Atmosphere	inletOutlet	totalPressure	pressureInlet-OutletVelocity	inletOutlet		zeroGradient
MidPlane	symmetryPlane					
Side	symmetryPlane					
Hull	zeroGradient	fixedFlux-Pressure	movingWall-Velocity	kqRWall-Function	omegaWall-Function	nutRWall-Function

Table 12 Solvers and tolerances

	alpha.water	p_rgh	pcorr	U	k	omega
Solver	smoothSolver	GAMG		smoothSolver		
Smoother	symGaussSeidel	DIC		symGaussSeidel		
Tolerance	1.00E-08	1.00E-07	1.00E-04	1.00E-08		

The simulation is performed in two phases: In the first phase, calm resistance with a static mesh is modeled. In the second step, the latest state of calm water resistance after

convergence is used as an initial data for simulation of the ship with forward speed in the waves. In this stage, a dynamic mesh was used to capture the ship motions caused by wave impacts. Maximum time-step is set in a way that wave propagation Courant number is around 0.2.

Wave Modeling

To model the ship with forward speed usually a uniform current is used against the ship instead of static water and moving ship. Therefore to simulate the ship with forward speed in a wave, CombinedWaves theory in waves2Foam should be used. This will allow combining the uniform current and the incoming waves to solve the problem.

However, it should be noted that although we are aiming to only superpose the wave and current, in reality, a combination of wave and current will affect the wave characteristic, e.g., wave height. Therefore a modification is needed on the wave theory to deal with this problem as a superposition.

To do that, variable T which is wave period should be manipulated to be read from the waveProperties dictionary, and it should be set to the original wave frequency, but ω which is wave frequency should be set to encounter frequency. The reason for this is the wave theory is coded in a way that the frequency variable deals only with phase but the wave period variable deals with the combined effect. Therefore setting the wave period to the original wave frequency will change the problem to superposition.

5.3.3 Results

Taito supercluster is used to run the cases. Results are obtained after more than ten stable oscillations. Table 13 shows the computation time of cases.

Figure 39 shows the motions for all 4 cases in model scale. The heave values are multiplied by the scale ratio to represent the full-scale motions.

Table 13 *Computation time in all the cases*

	Number of cells $\times 10^6$	Simulation Type	Simulation Time	CPU Hours/Million Cell
Case1	2.957187	Calm Water	100 [s]	288.1
		Wave	30T	352.6
Case2	3.916092	Calm Water	100 [s]	160.1
		Wave	30T	428.3
Case3	5.174318	Calm Water	100 [s]	120.9
		Wave	30T	1348.0
Case4	7.128524	Calm Water	100 [s]	147.0
		Wave	30T	1272.5

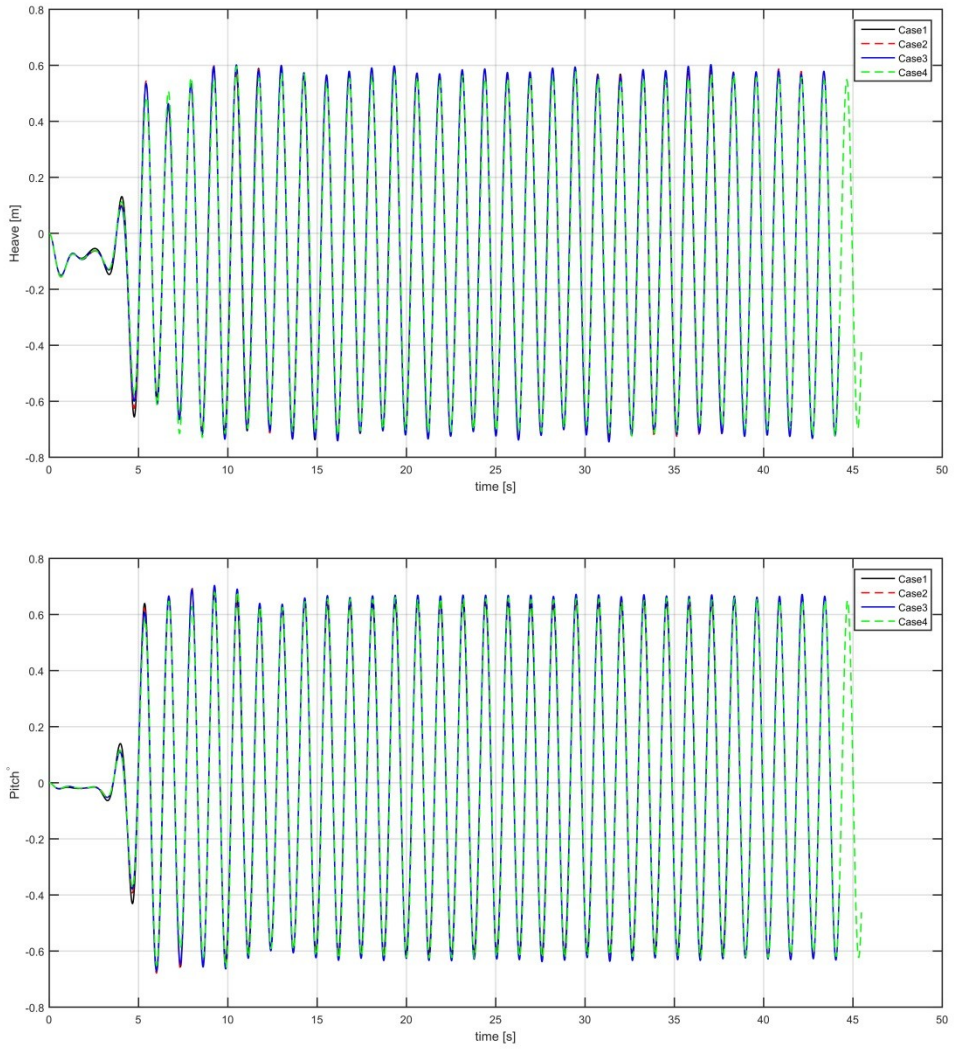

Figure 39 *Heave and pitch motions of all cases in model scale*

From the graphs, there is no noticeable difference between the cases results. To have a more clear look, Fourier analysis is performed on the motions history.

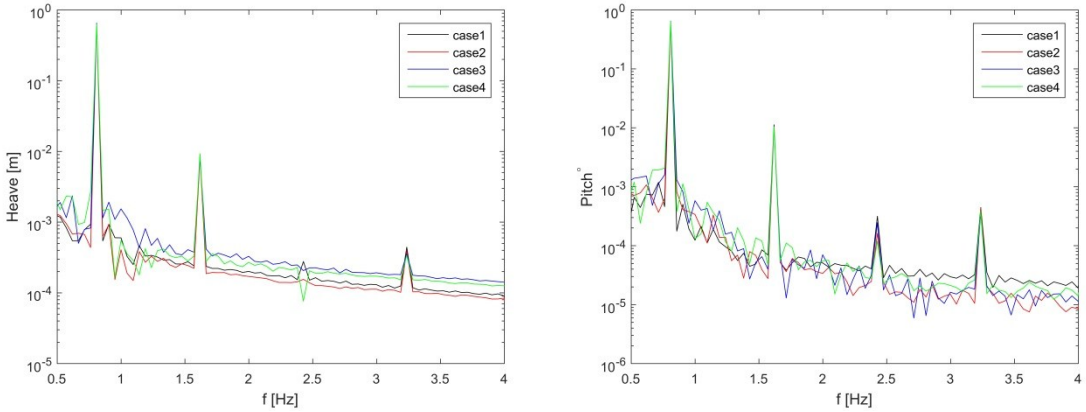

Figure 40 *Fourier analysis of heave and pitch motions in model scale*

The error compared to experimental data is reported in Table 14.

Table 14 *Error in heave and pitch motions compare to experimental data*

	Error in Heave	Error in Pitch
Case1	1.3%	0.5%
Case2	1.8%	2.5%
Case3	1.9%	4.6%
Case4	-1.3%	2.9%

As can be seen the error in heave is around -1%-2% and in pitch is up to 4%. Looking at the Fourier transform results it can be seen that case 3 and 4, which have finer grids, have more fluctuations. One explanation can be that in finer grids there are more cells in the mesh motion area than the coarser grid and also the aspect ratio of cells are higher, which cause distorted or poor meshes that might impair the quality of the results. Another source of error in the data can be due to the restriction of the other motions. Forexample, surge motion might change the longitudinal center of rotation which might affect the pitch motions. In addition, it should be mentioned that the experimental data also contains an error in measurement.
Ship motions over a period are pictured in Figure 41. At t=42.7 s, the ship experiences a trim to fore and submerged at its highest draft. The wave crest hits the ship and splashes on the foreship. Moving the wave crest to midship at t=43 s, the highest trim to aft occurs and it gradually comes back to even condition.

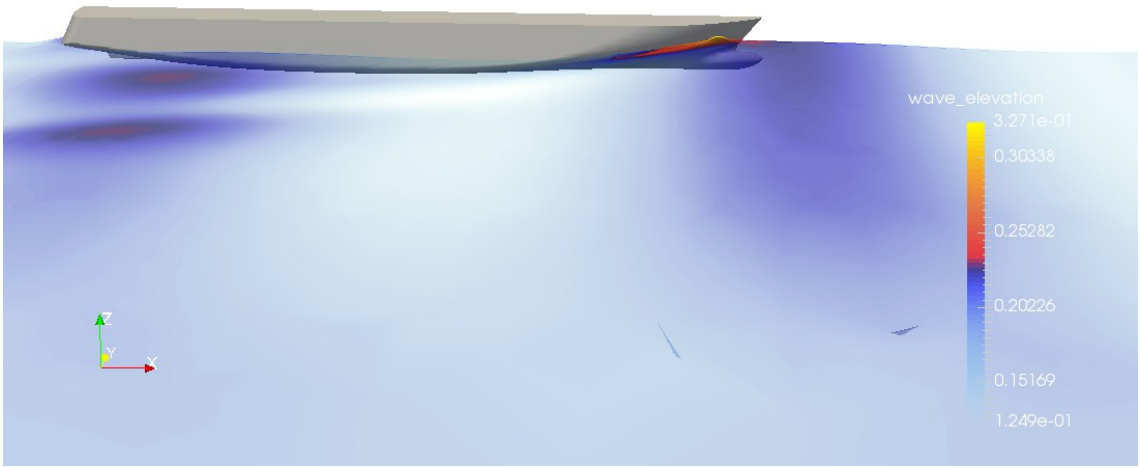

t=42.7 [s]

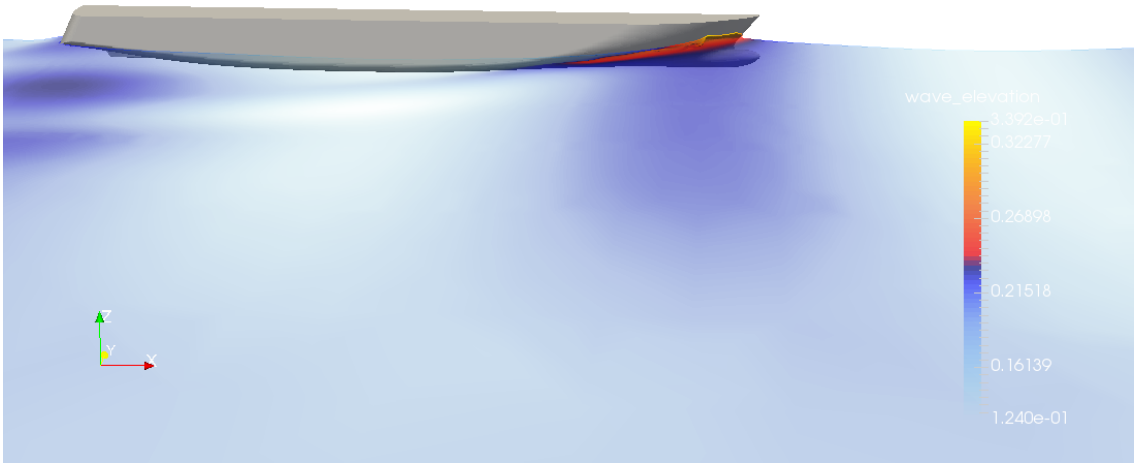

t=42.9 [s]

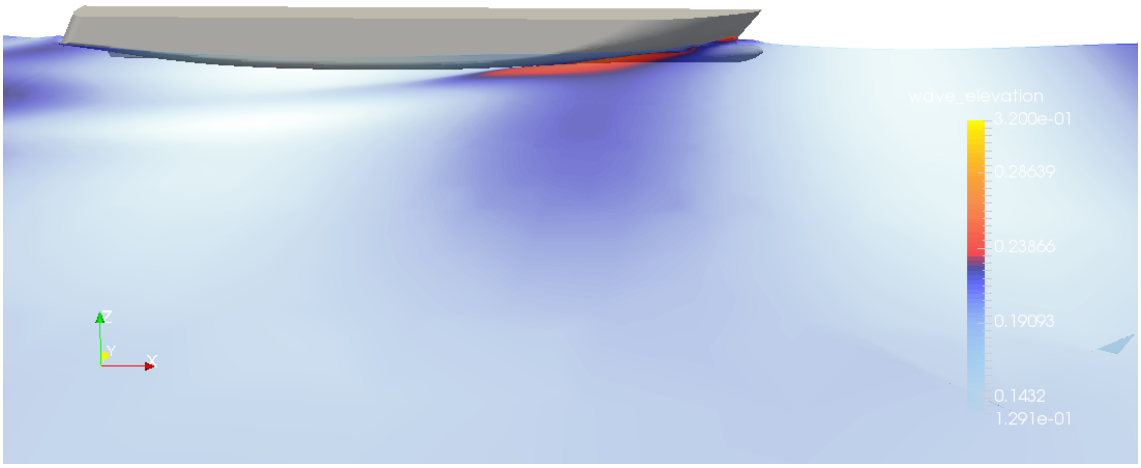

t=43.2 [s]

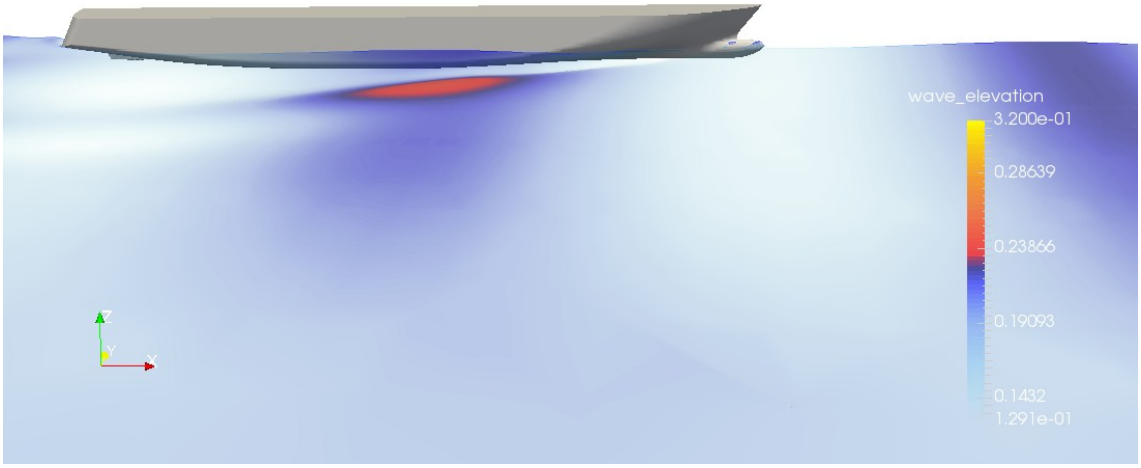

t=43.4 [s]

t=43.6 [s]

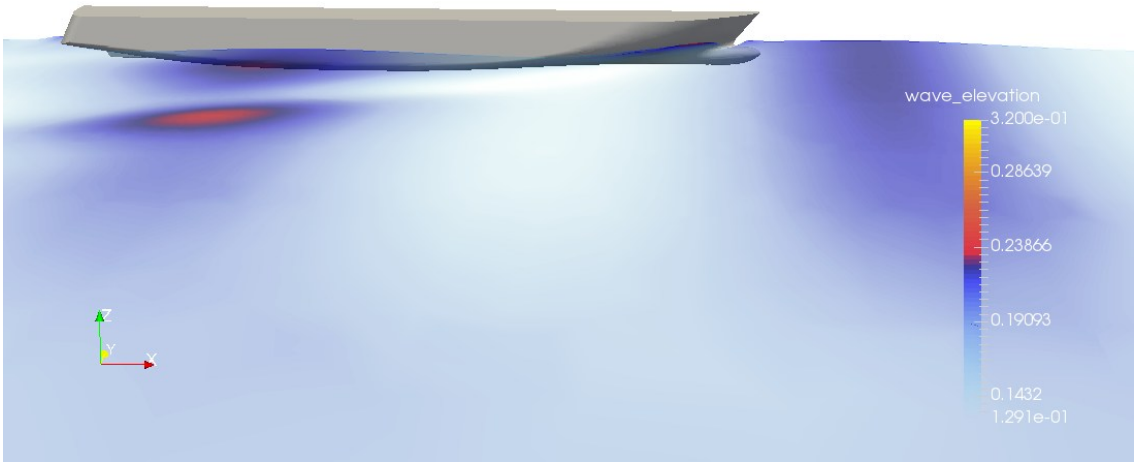

t=43.8

Figure 41 *Ship motions over a wave period*

5.3.4 Scaling Effect

Considering the resources and time, a five times' larger scale ship is modeled. To make comparison possible all the parameters such as solver, tolerances, boundary condition, mesh features, remain the same except the following that was not easy to do.

- y^+ increased slightly from 100 to 150
- A region close to the hull is refined one time to make a smooth transition between the boundary layer cells and castellated cells

To understand the effect of change in y^+value, case1 in model scale is tested with similar y^+ and results were compared to previous obtained data. The assessment shows less than 1% difference in the motions.
Three cases are defined:

Case	Cells/wave height	Cells/wavelength	Number of cells
1*	4.9	84.2	5160893
2*	6.8	84.2	6467009
3*	9.9	84.2	7824831

Results and Comparison

The Time history of heave and pitch motions are plotted in Figure 42.

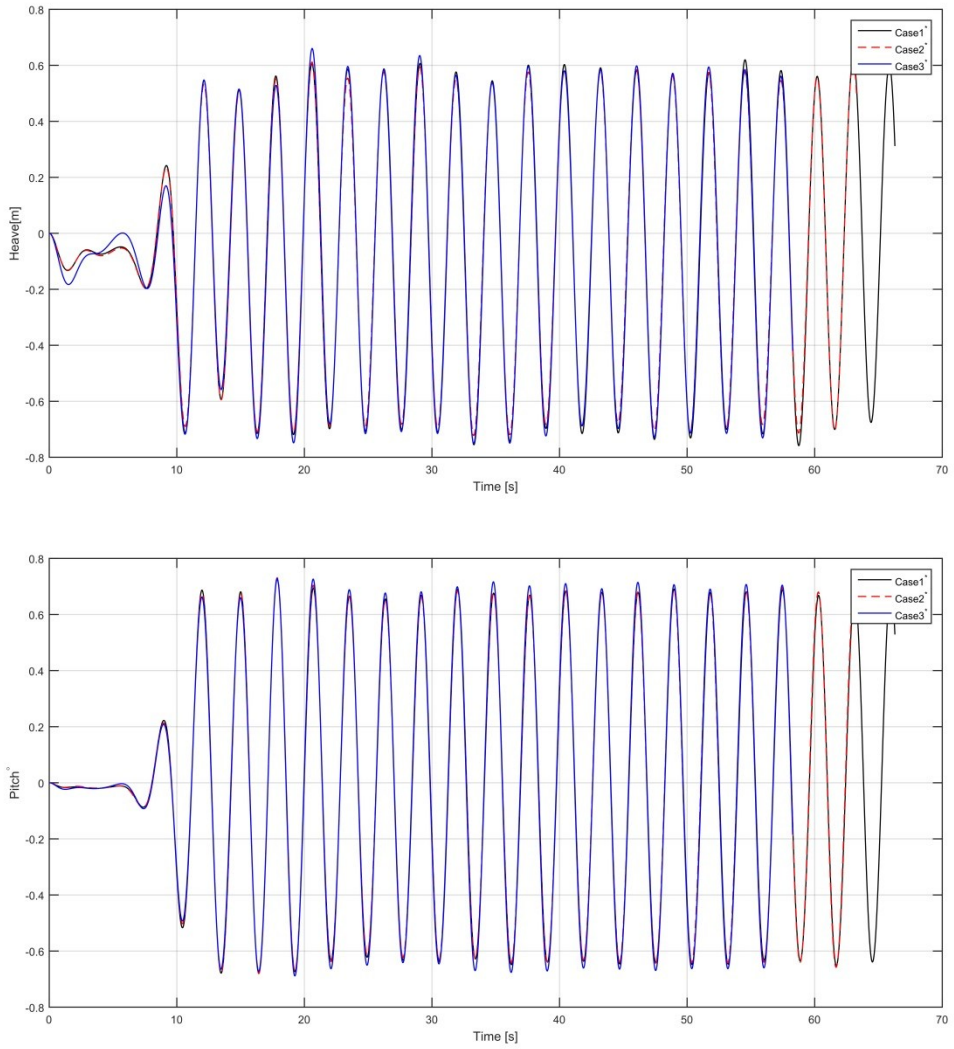

Figure 42 *Time history of heave and pitch motion in larger scale*

Moreover, the Fourier analysis of the results is illustrated below.

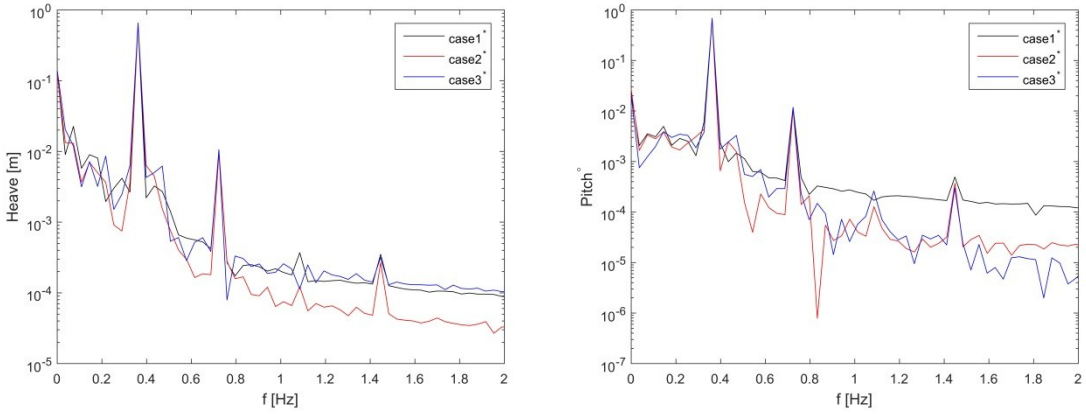

Figure 43 *Fourier analysis of the heave and pitch motions in larger scale*

Finally, the obtained values were compared to the model scale values, and the difference is reported in Table 15.

Table 15 *Difference in heave and pitch motions compared to model scale cases*

	Difference in Heave	Difference in Pitch
Case1*	0.9%	5.5%
Case2*	-1.6%	4.0%
Case3*	0.1%	4.8%

It can be observed, the difference between heave values are around $\pm 1\%$, but pitch values increased around $4 \sim 5\%$.

One comment about this result could be that ship motions in model scale are more restricted due to larger boundary layer while in the bigger scale the boundary layer is thinner. Therefore it is possible that pitch motions are more damped in model scale or more energy is dissipated with contact with the free surface. Another possibility is that waves are more attenuated in the vicinity of the hull due to larger boundary layer in model scale. To have a better understanding, a simplified equation of pitch motion in the center of gravity is presented below:

$$I_y \dot{q} - I_{yx} \dot{p} + I_{yz} \dot{r} = M \tag{89}$$

where, $p, q \; and \; r$ are directional components of angular velocity in x, y, z directions and I is the mass moment of inertia. Since the motion is only free to rotate around y axis, therefore $\dot{p} = \dot{r} = 0$ and,

$$I_y \dot{q} = M \tag{90}$$

And M is the momentum of forces acting on the body, (Matusiak, 2017)

$$M = \vec{r} \times F_{total} \tag{91}$$

A larger boundary layer could result in more extensive added mass and increase the inertia forces. Therefore, in model scale more force would be required to maintain the same angle, and it would be reasonable to obtain higher values of motion in the presence of a thinner boundary layer. If true, on the other hand, the effect should be noticed in heave motions as well. However, considering the magnitude of motions compared to the possible effect of these factors is unlikely to be of this magnitude.

On the other hand, it was already observed that finer grid with larger aspect ratio tends to result in more significant error especially for pitch motion. Because the grid is more refined around the hull in this larger scale for all the cases, the probability of considering this result as an overestimation is also realistic.

6 Summary and Conclusion

This thesis intended to numerically model ship motions and study possible scaling effects of ship motions in waves. The work was divided into three stages: a parametric grid study of wave propagation in an empty basin; validation of wave-induced forces on a cylinder and modeling of the ship motions with forward speed in head waves. This division aimed to build knowledge step by step.

OpenFOAM in pair with waves2Foam package was used as a numerical tool. In the first stage, a typical ocean wave was studied with 4 grid refinements by the square root of two in wavelength and wave height direction. The first case is defined with only four cells in wave height and aspect ratio of 1. The base case then was refined 4 times in both directions. Moreover two Courant number were considered. Therefore, 50 cases are defined and simulated in 2-D. The results showed longer time-steps and taller cells will cause instability and ripples in the free-surface, but long cells exposed no adverse effect on the quality of results. It was also presented that wave energy, and consequently amplitude strongly depends on the number of cells in the wave height. Wave dissipation shows an exponential decay along the domain with a more dependency on the number of cells in wavelength. It is also demonstrated that the phase shift in waves is a function of time step and number of cells in wavelength.

In the second stage, the wave loads on a circular cylinder were modeled in three dimensions and results were compared to experimental data. It is shown that the model is highly capable of predicting the forces on a simple geometry. In addition, it is determined that long cells in the third direction do not have a negative effect on the results.

In the third stage, first, a model scale ship with forward speed was simulated in head waves with 4 meshes and result were compared to experimental data. Good agreement with experimental data is obtained. It was also proposed that very fine meshes with large aspect ratio might be problematic in case of mesh motion in the vicinity of complex geometry. Finally, the ship is scaled five times larger and simulated with three comparable meshes for two model scale cases. The result show no noticeable change in heave motion but values of pitch motion increased 4~5%. It is proposed that the difference might come from the boundary layer characteristic of the problem; however, more studies would be required to increase the confidence in results.

Finally, it is concluded that the model is very capable of predicting the detailed flow field around the ship in head waves as well as ship motions in a justifiable amount of time in the model scale and can be utilized in ship early design process.

In future, the sensitivity of results to grid quality and aspect ratio in mesh motion area should be studied to eliminate the concerns associated with it. In addition, the simulation could be repeated using two sets of model and full-scale experimental data. Moreover, the study could be extended to incident waves with various angles and also irregular waves to simulate more realistic wave conditions.

7 Bibliography

Alberello, A. (2017) *Kinematics of Breaking Rogue Waves*. Swinburne University of Technology.

Castiglione, T. *et al.* (2011) 'Numerical investigation of the seakeeping behavior of a catamaran advancing in regular head waves', *Ocean Engineering*, 38, pp. 1806–1822.

CFD Online (2011). Available at: https://www.cfd-online.com/Wiki/Law_of_the_wall.

Chen, L. F. *et al.* (2014) 'Numerical investigation of wave–structure interaction using OpenFOAM', *Ocean Engineering*, 88, pp. 91–109.

Chenari, B., Saadatian, S. S. and Ferreira, A. D. (2015) 'Numerical Modelling of Regular Waves Propagation and Breaking Using Waves2Foam', *Journal of Clean Energy Technologies*, 3(4), pp. 276–281.

Froude, W. (1861) 'On the rolling of ships', *Transactions of Institution of Naval Architects*, 2, p. 180.

Gadelho, J. F. M., Lavrov, A. and Guedes Soares, C. (2014) 'Modelling the effect of obstacles on the 2D wave propagation with OpenFOAM', in Peña, G. S. & L. (ed.) *Developments in Maritime Transportation and Exploitation of Sea Resources*. London: Taylor & Francis Group, pp. 1057–1065. doi: 10.1201/b15813-133.

Hanoka, T. (1957) 'Theoretical Investigation Concerning Ship Motion in Regular Waves', in *Proceedings of Symposium on the Behaviour of Ships in a Seaway*, pp. 266–285.

Havelock, T. (1940) 'The Pressure of Water Waves upon a Fixed Obstacle', *Proceedings of the Royal Society*, 175, pp. 409–421.

Hirt, C. W. and Nichols, B. D. (1981) 'Volume of fluid (VOF) method for the dynamics of free boundaries', *Journal of Computational Physics*, 39(1), pp. 201–255.

Jacobsen, N. G., Fuhrman, D. R. and Fredsøe, J. (2012) 'A wave generation toolbox for the open-source CFD library: OpenFoam®', *International Journal for Numerical Methods in Fluids*, 70(9), pp. 1073–1088. doi: 10.1002/fld.2726.

Jacobsen, N., Van Gent, M. R. A. and Wolters, G. (2015) 'Numerical analysis of the interaction of irregular waves with two dimensional permeable coastal structures', *Coastal Engineering*, 102, pp. 13–29.

Kent, J. (1922) 'Experiments on Mercantile Ship Models in Waves (First Series)', *Transactions of the Institution of Naval Architects*.

Kent, J. (1924) 'The Effect of Wind and Waves on the Propulsion of Ships', *Transactions of Institution of Naval Architects*.

Kochin, N. (1937) 'On the wave resistance and lift of bodies submerged in a fluid', in *Proceedings of the Conference On the Wave Resistance Theory*. Moskow, pp. 65–134.

Kreitner, H. (1939) ‘Heave, Pitch, and Resistance of Ships In A Seaway’, *Transactions of Institution of Naval Architects*.

Krylov, A. (1896) ‘A new theory of the pitching motion of ships on waves and of the stresses produced by this motion’, *Transactions of Institution of Naval Architects*, 37, pp. 326–359.

Krylov, A. (1898) ‘A general theory of the oscillations of a ship on waves’, *Transactions of Institution of Naval Architects*, 40, pp. 135–190.

Larsson, L. and Raven, H. C. (2010) *Ship Resistance and Flow*. Edited by J. R. Paulling. The Society of Naval Architects and Marine Engineers.

Lautrup, B. (2011) ‘Stokes waves’, in *Physics of Continuous Matter, Second Edition: Exotic and Everyday Phenomena in the Macroscopic World*. CRC Press.

LeMéhauté, B. (1976) *An introduction to hydrodynamics and water waves*. Springer.
Lewis, F. (1929) ‘The inertia of water surrounding a vibrating ship’, *Transactions of Institution of Naval Architects*, 37, pp. 1–20.

Matusiak, J. (2017) *Dynamic of a Rigid Ship*. 2nd edn. Aalto University.

Mauro, H. (1957) ‘The Excess Resistance of a Ship in Rough Seas’, *International Shipbuilding Progress*, 4(35), pp. 337–345.

Mauro, H. (1960a) ‘The drift of a body floating on waves’, *Journal of Ship Research*, 4.

Mauro, H. (1960b) ‘Wave Resistance of a Ship in Regular Head Seas’, *Bulletin of the Faculty of Engineering, Yokohama National University*, 9.

Mauro, H. (1963) ‘Resistance in Waves’, *Society of Naval Architects Journal*, 8.

Menter, F. (1994) ‘Two-equation eddy-viscosity turbulence models for engineering applications’, *AIAA Journal*, 32(8), pp. 269–289.

Menter, F., Kuntz, M. and and Langtry, R. (2003) ‘Ten Years of Industrial Experience with the SST Turbulence Model’, in *Proceedings of the 4th International Symposium on Turbulence, Heat and Mass Transfer*, pp. 625–632.

Michell, J. H. (1898) ‘Wave Resistance of a Ship’, *Philosophical Magazine*, 45, p. 113.

Morgan, G. *et al.* (2010) ‘Using the rasInterFoam CFD model for wave transformation and coastal modelling.’, in *Proceedings of 32nd Conference on Coastal Engineering*. Shanghai.

Roenby, J. *et al.* (2017) ‘A NEW VOLUME-OF-FLUID METHOD IN OPENFOAM’, in *VII International Conference on Computational Methods in Marine Engineering*.

Seiffert, B., Hayatdavoodi, M. and Ertekin, R. C. (2014) ‘Experiments and computations of solitary-wave forces on a coastal-bridge deck. Part I: Flat Plate’, *Coastal Engineering*, 88, pp. 194–209.

Shen, Z. R. and Wan, D. C. (2013) 'RANS Computations of added resistance and motions of ship in head wave', *International Journal of Offshore and Polar Engineering*, pp. 263–271.

Shen, Z. R., Ye, H. X. and Wan, D. C. (2012) 'Motion response and added resistance of ship in head waves based on RANS simulations', *Chin. J. Hydrodyn*, pp. 621–633.

Stern, F., Hwang, W. S. and Jaw, S. (1987) *Effects of waves on the boundary layer of a surface-piercing flat plate: experiment and theory*.

Stokes, G. (1847) 'ON THE THEORY OF OSCILLATORY WAVES.', *From the Transactions of the Cambridge Philosophical Society*, VIII, p. 441.

The OpenFOAM Foundation (2017a) *OpenFOAM Programmer's Guide*. Available at: https://sourceforge.net/projects/openfoamplus/files/v1706/ProgrammersGuide.pdf.

The OpenFOAM Foundation (2017b) *The OpenFOAM User Guide*. Available at: https://sourceforge.net/projects/openfoamplus/files/v1706/UserGuide.pdf.

tutor (no date). Available at: http://www.tutorhelpdesk.com/homeworkhelp/Fluid-Mechanics-/Laminar-Boundary-Layer-Assignment-Help.html (Accessed: 1 August 2017).

Weller, H. G. *et al.* (1998) 'A tensorial approach to computational continuum mechanics using object-oriented techniques', *American Institute of Physics*.

White, F. M. (2006) *Viscous Fluid Flow*. 3rd edn. New York, NY: McGraw-Hill.

Wilcox, C. W. (2008) 'Formulation of the k −ω Turbulence Model Revisited', *AIAA Journal,* 46(11), pp. 2823–2838.

Windén, B. (2014) *Powering Performance of a Self Propelled Ship in Waves*. University of Southampton.

Zang, J., Taylor, P. H., Morgan, G., Tello, M., *et al.* (2010) 'Experimental study of non-linear wave impact on offshore wind turbine foundations.', in *Third International Conference on the Application of Physical Modelling to Port and Coastal Protection*. Barcelona.

Zang, J., Taylor, P. H., Morgan, G., Stringer, R., *et al.* (2010) 'Steep wave and breaking wave impact on offshore wind turbine foundations— ring re-visited', in *The 25th IWWWFB*. Harbin.

Appendix List

Appendix 1. Wave Profile and Fourier Analysis Figures

.

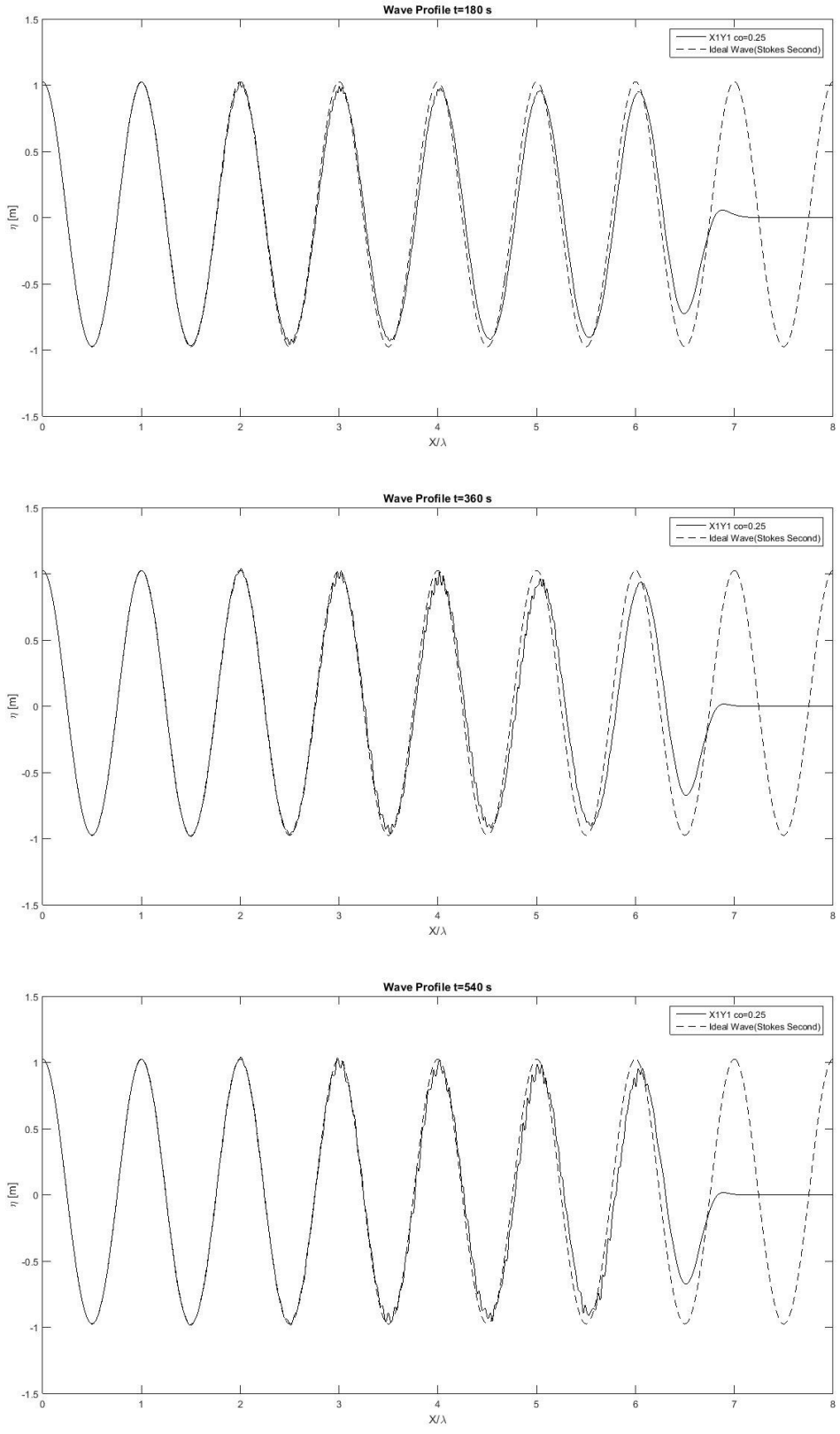

Figure 44 *Wave profile for case X1Y1 Co=0.25*

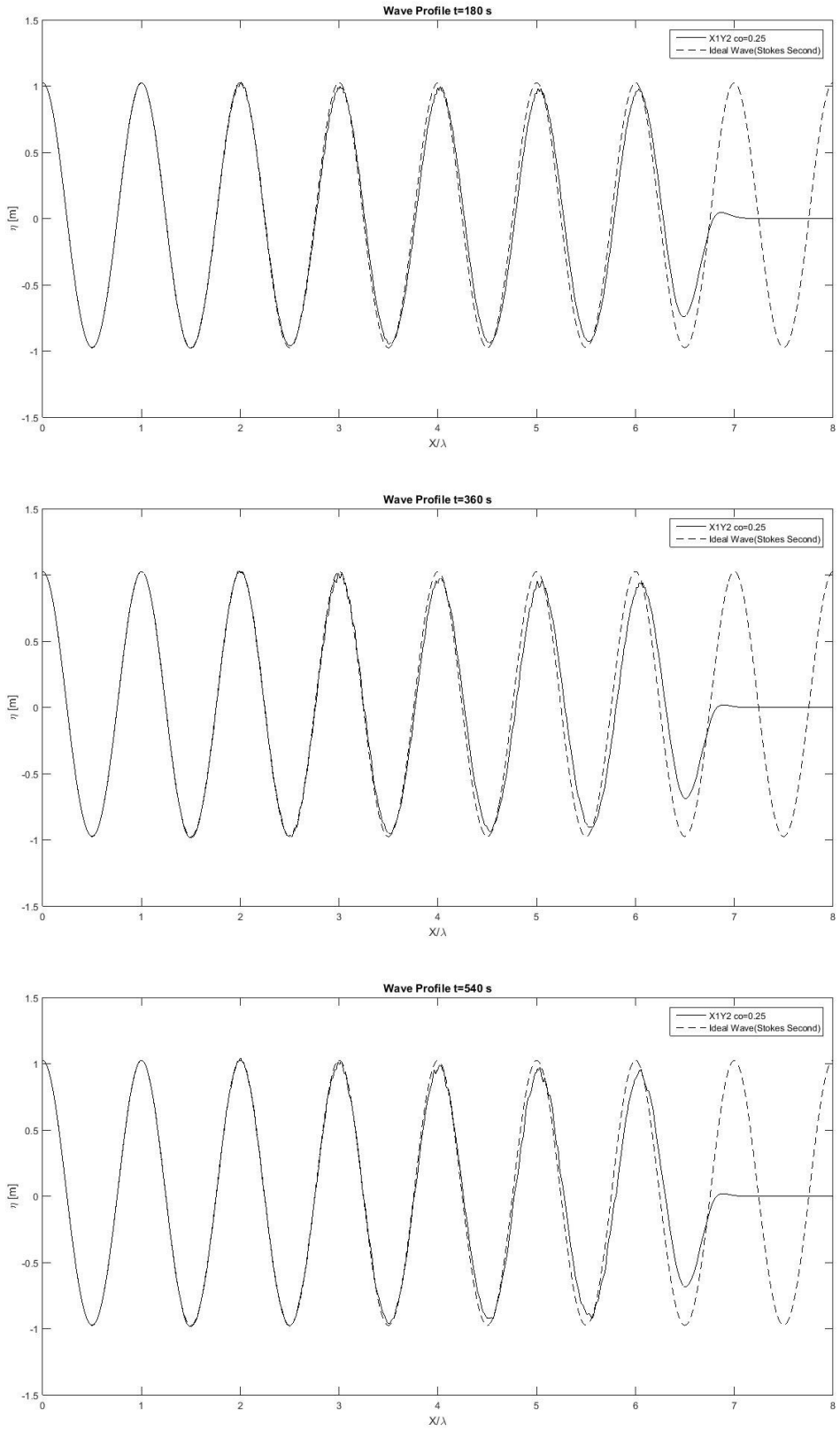

Figure 45 *Wave Profile for case X1Y2 Co=0.25*

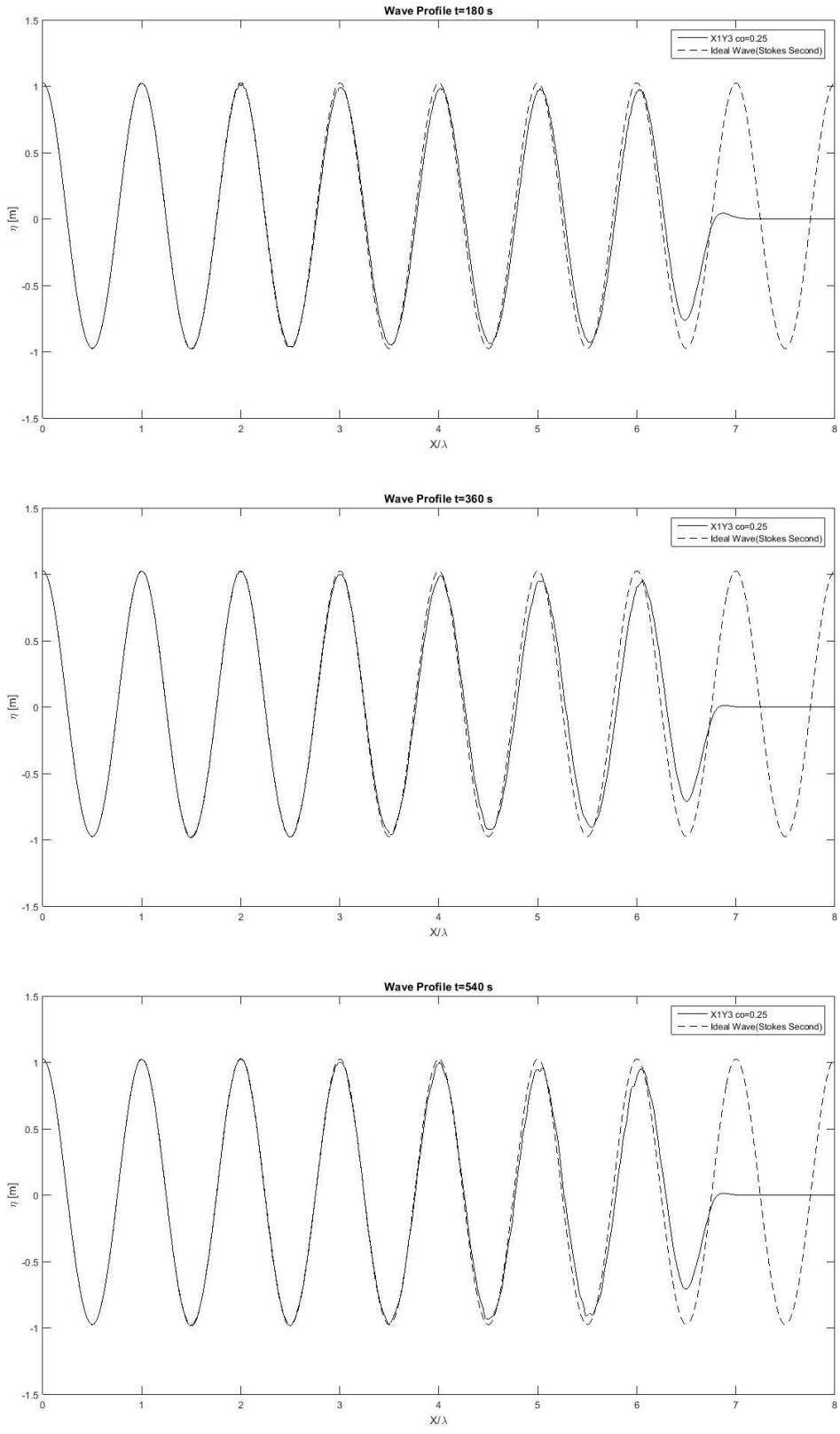

Figure 46 *Wave Profile for case X1Y3 Co=0.25*

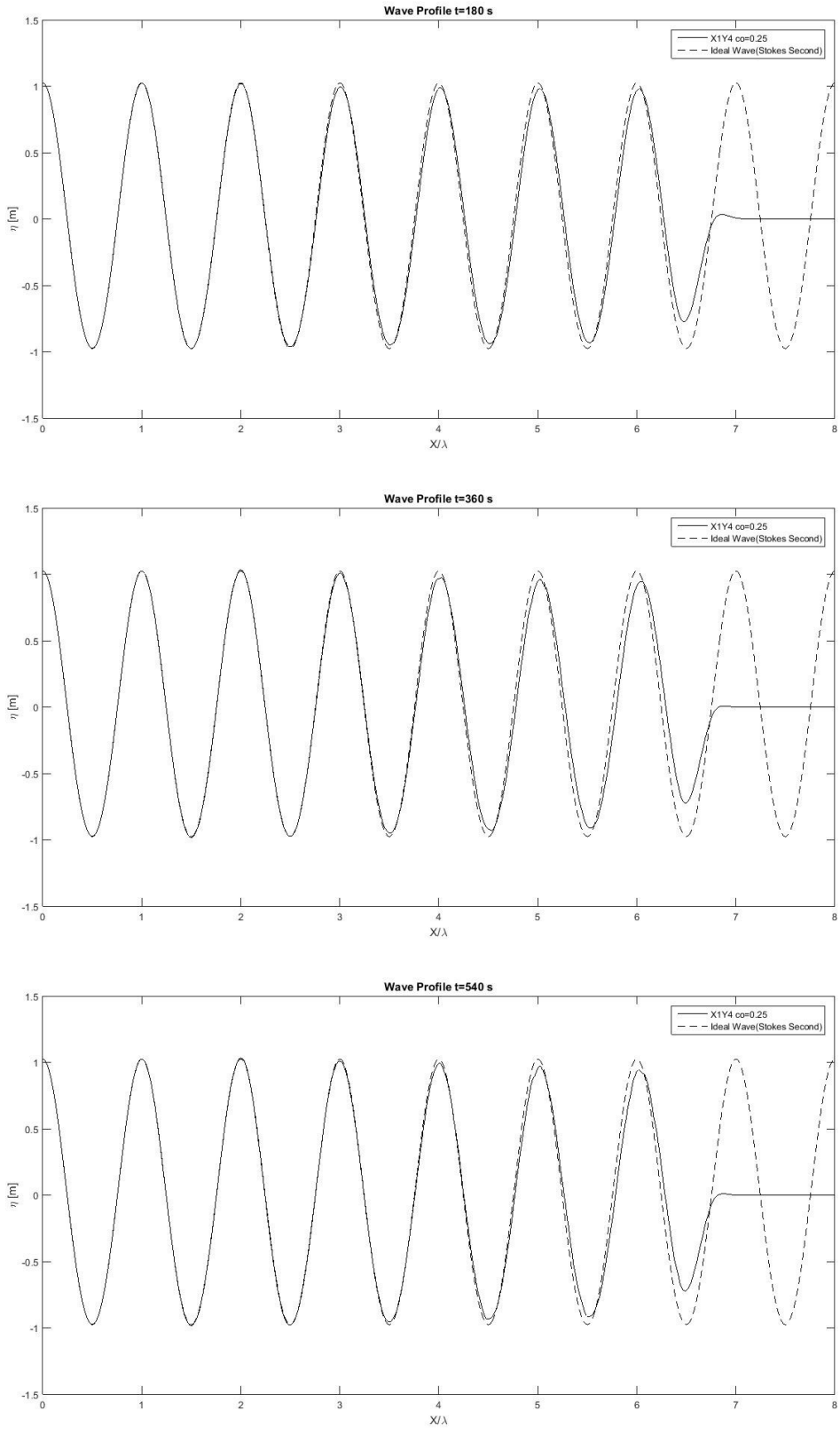

Figure 47 *Wave Profile for case X1Y4 Co=0.25*

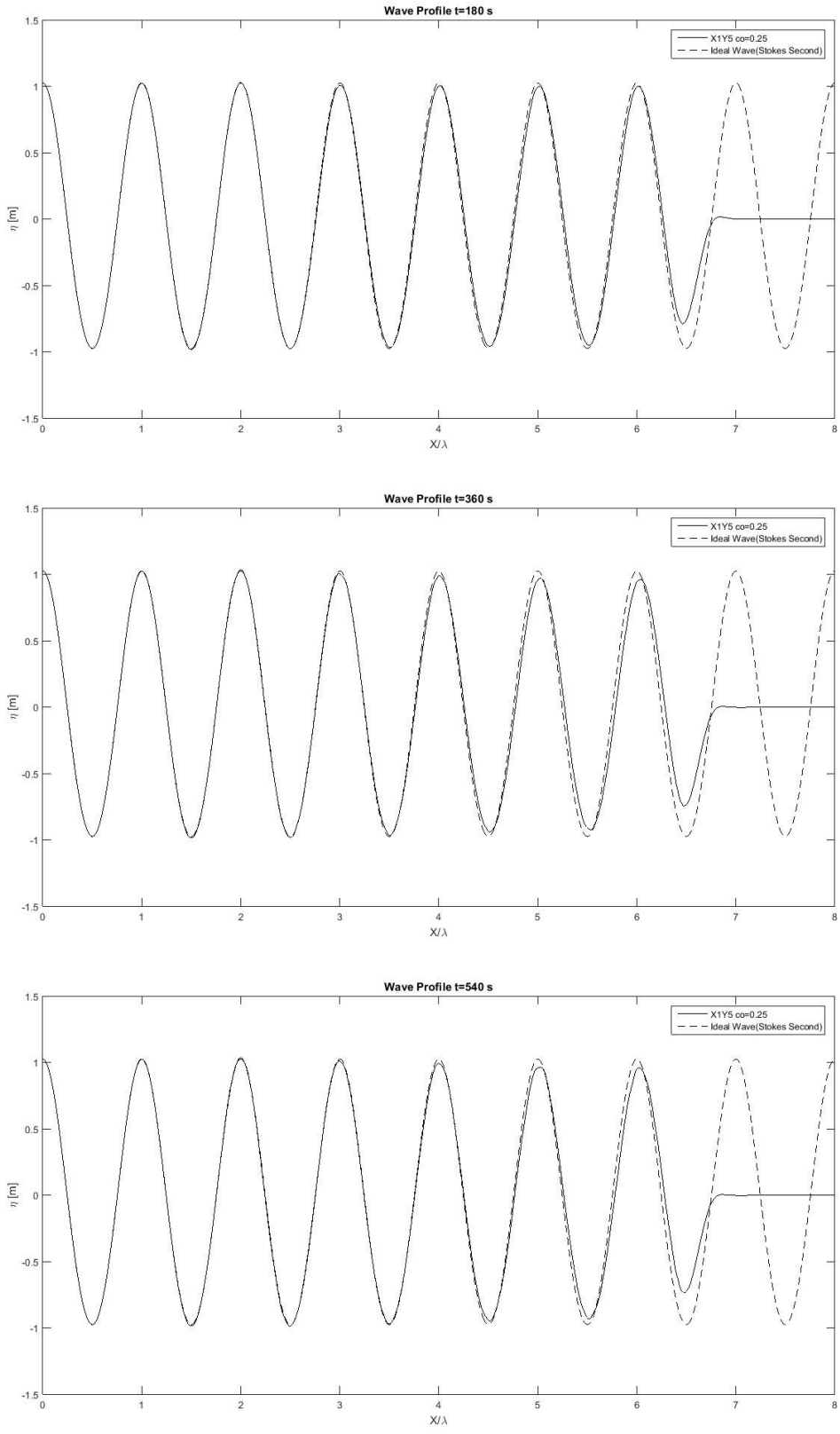

Figure 48 *Wave Profile for case X1Y5 Co=0.25*

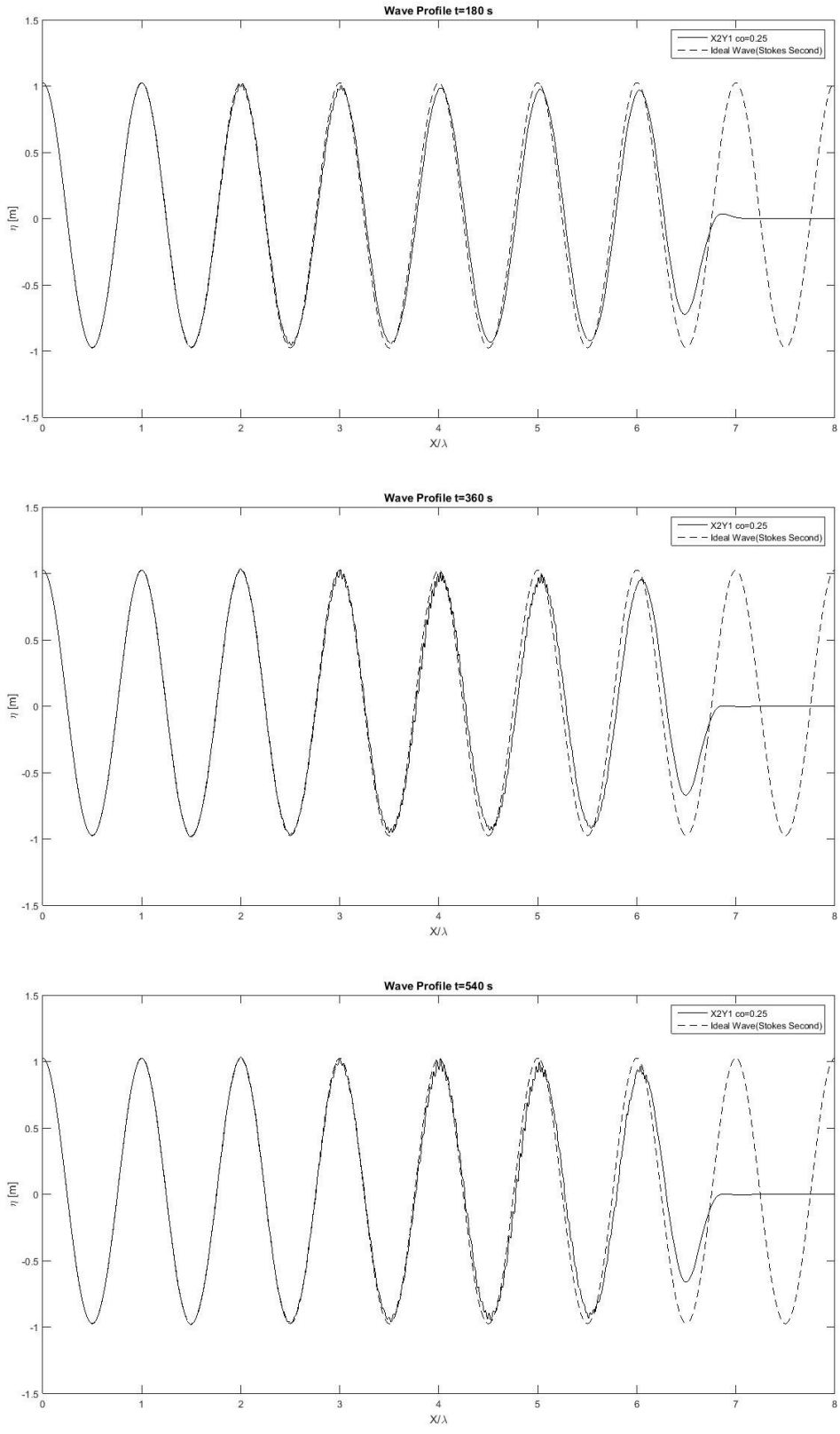

Figure 49 *Wave Profile for case X2Y1 Co=0.25*

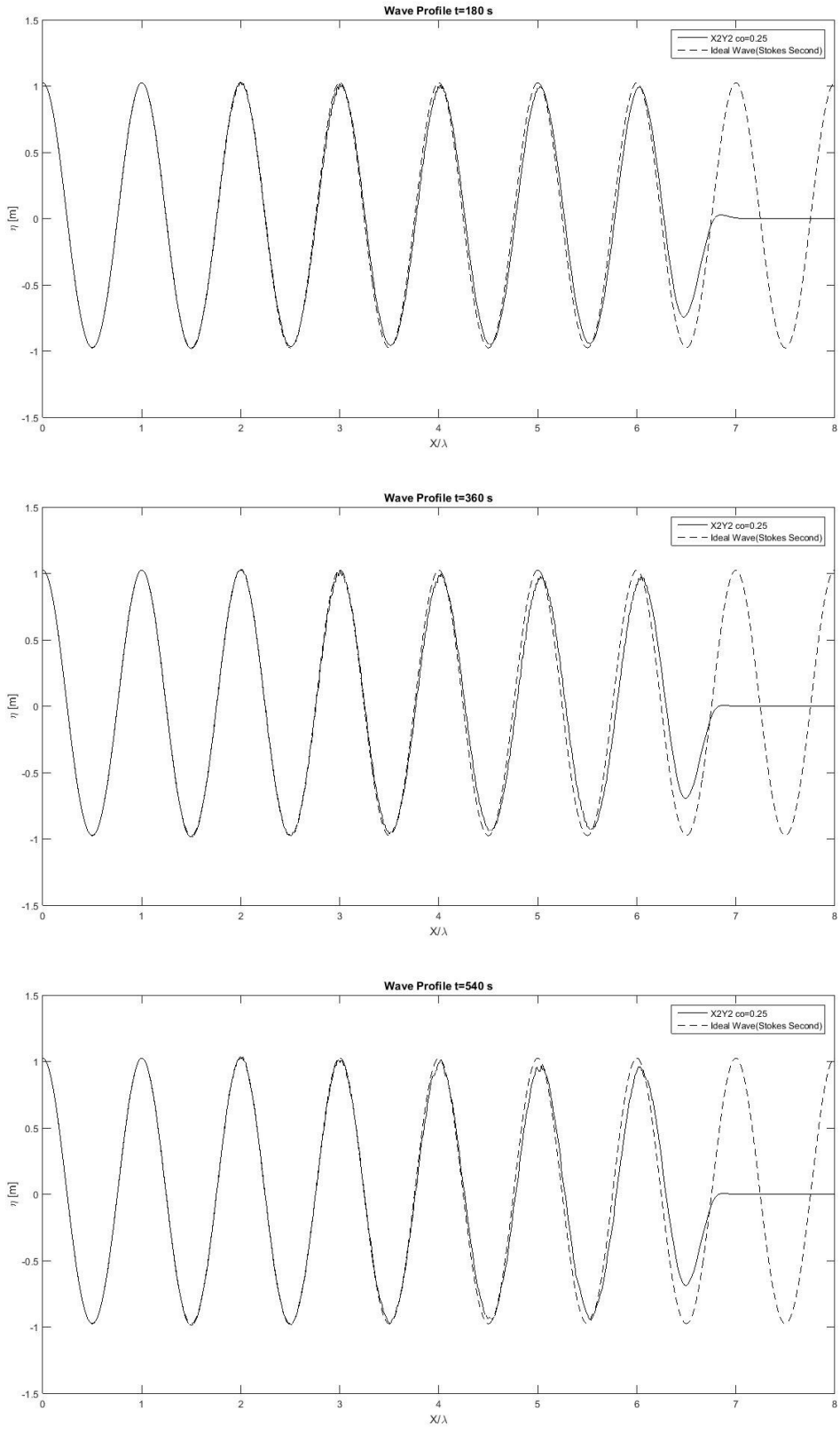

Figure 50 *Wave Profile for case X2Y2 Co=0.25*

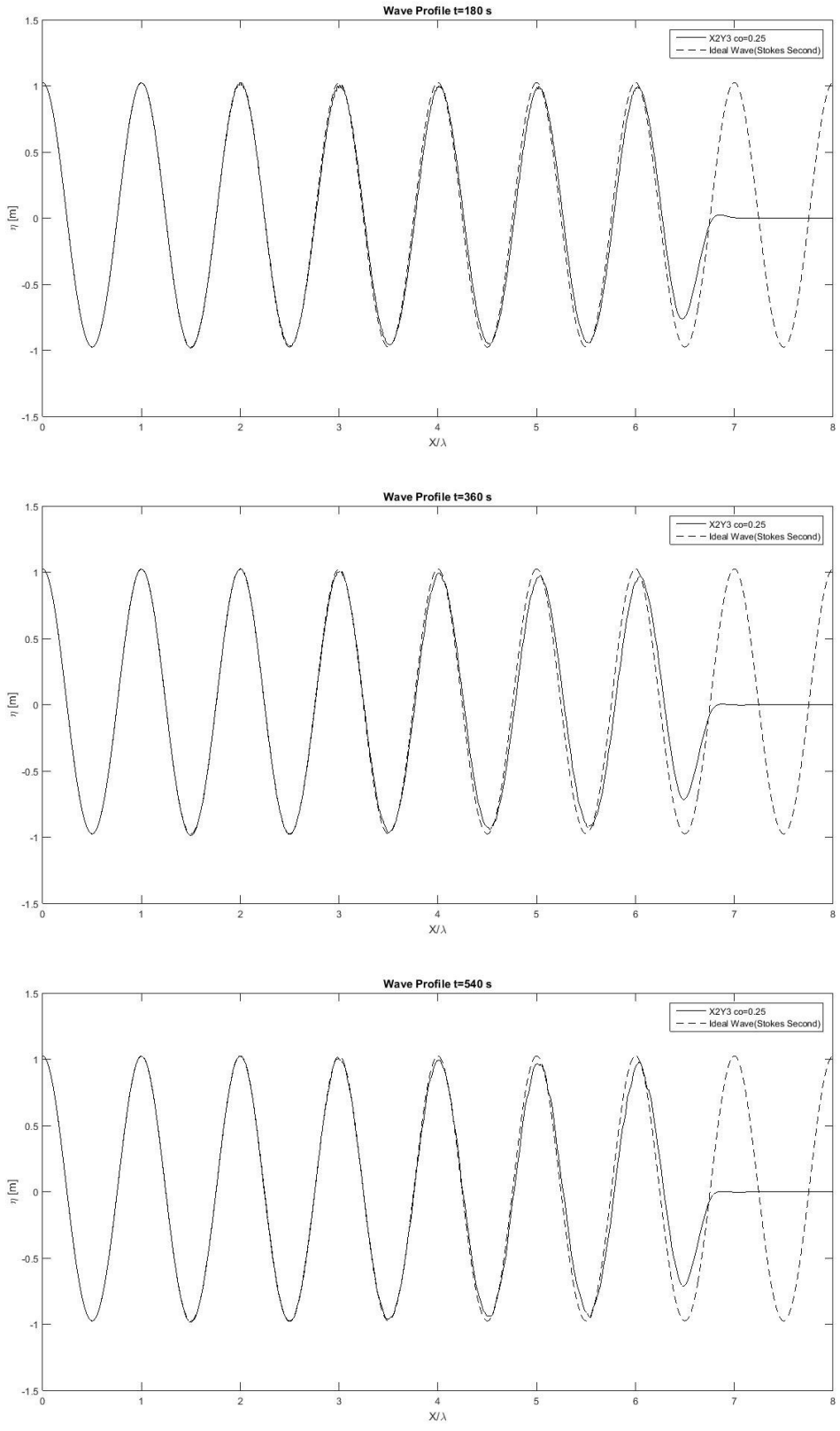

Figure 51 *Wave Profile for case X2Y3 Co=0.25*

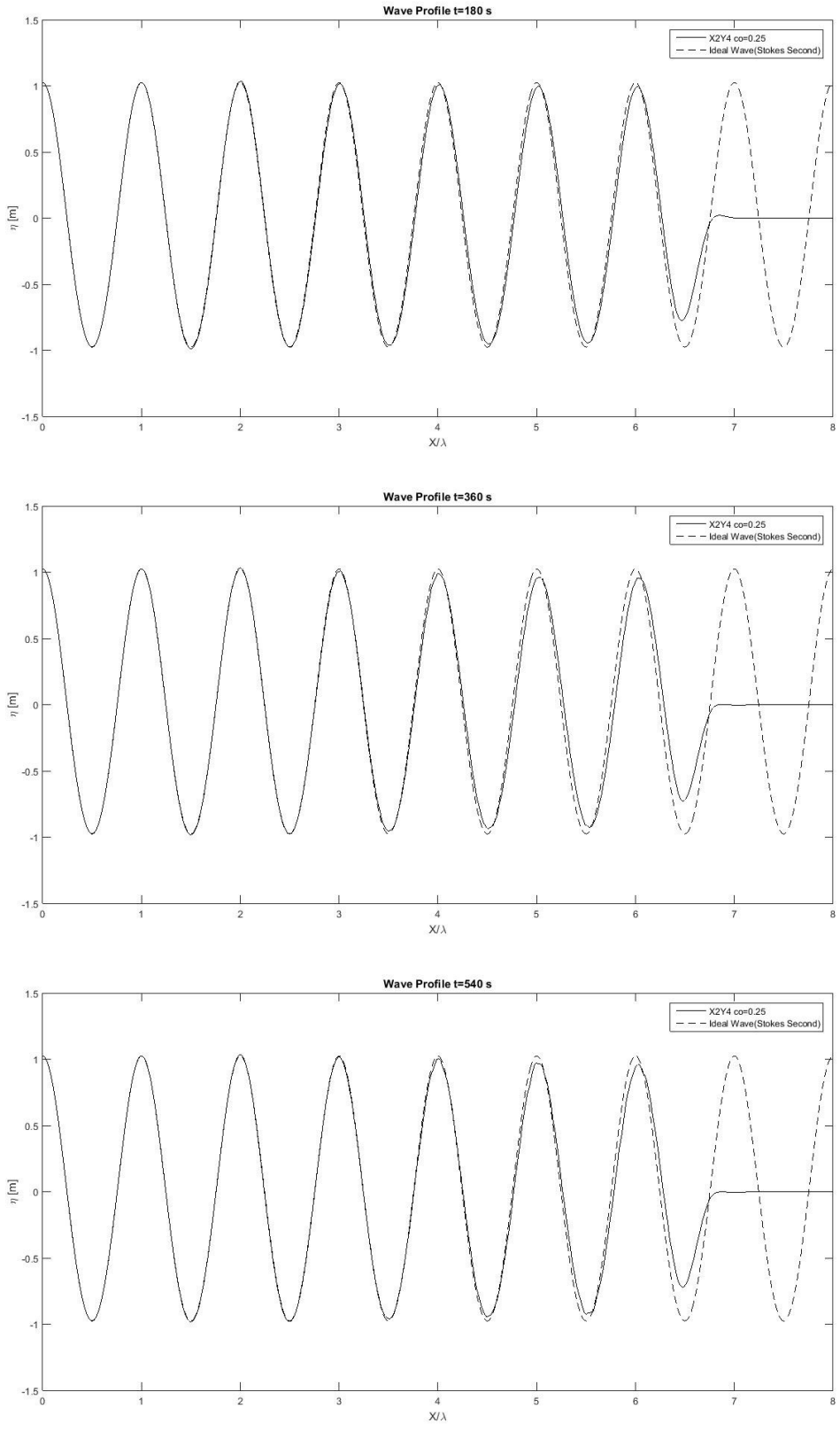

Figure 52 *Wave Profile for case X2Y4 Co=0.25*

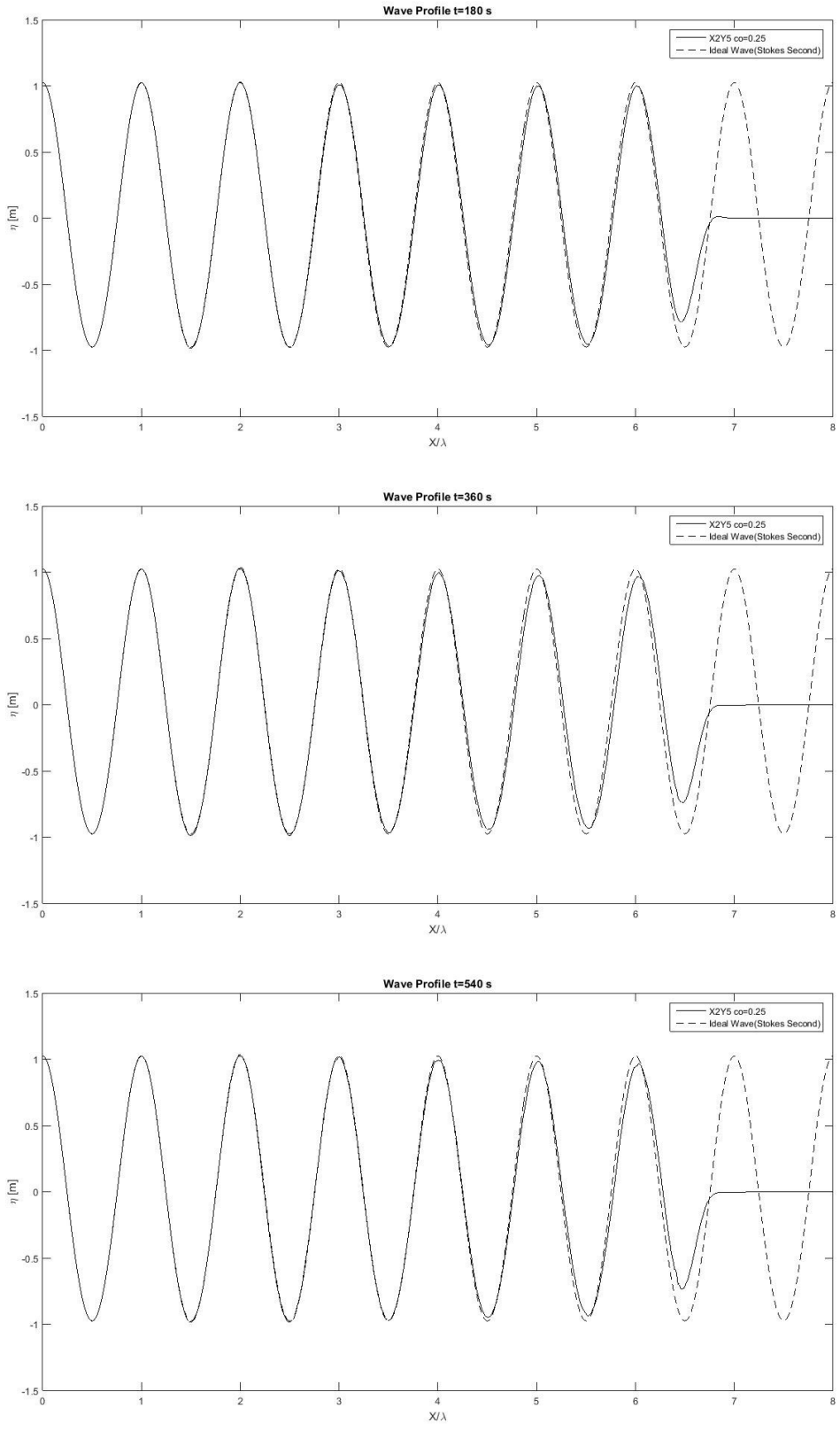

Figure 53 *Wave Profile for case X2Y5 Co=0.25*

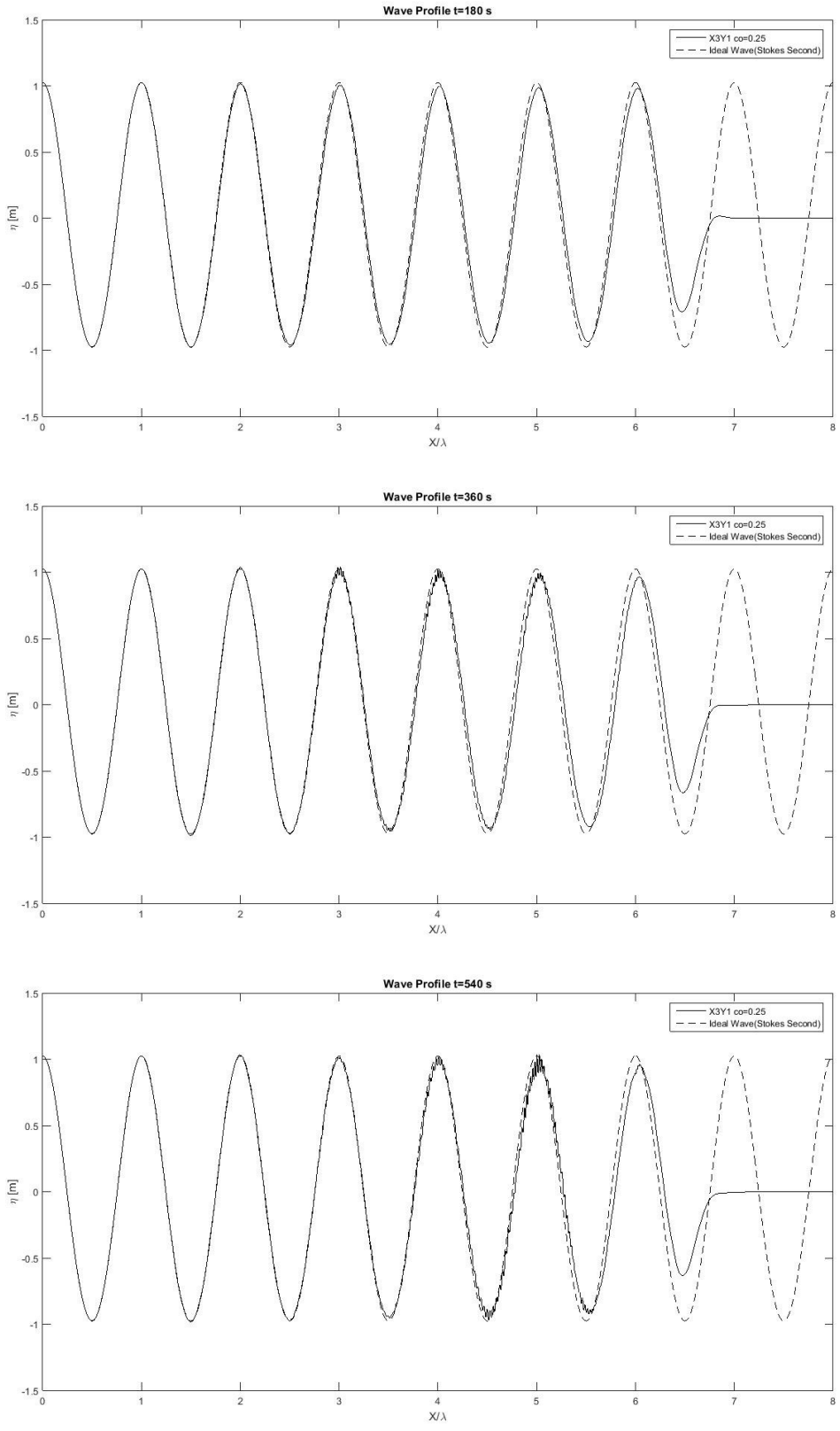

Figure 54 *Wave Profile for case X3Y1 Co=0.25*

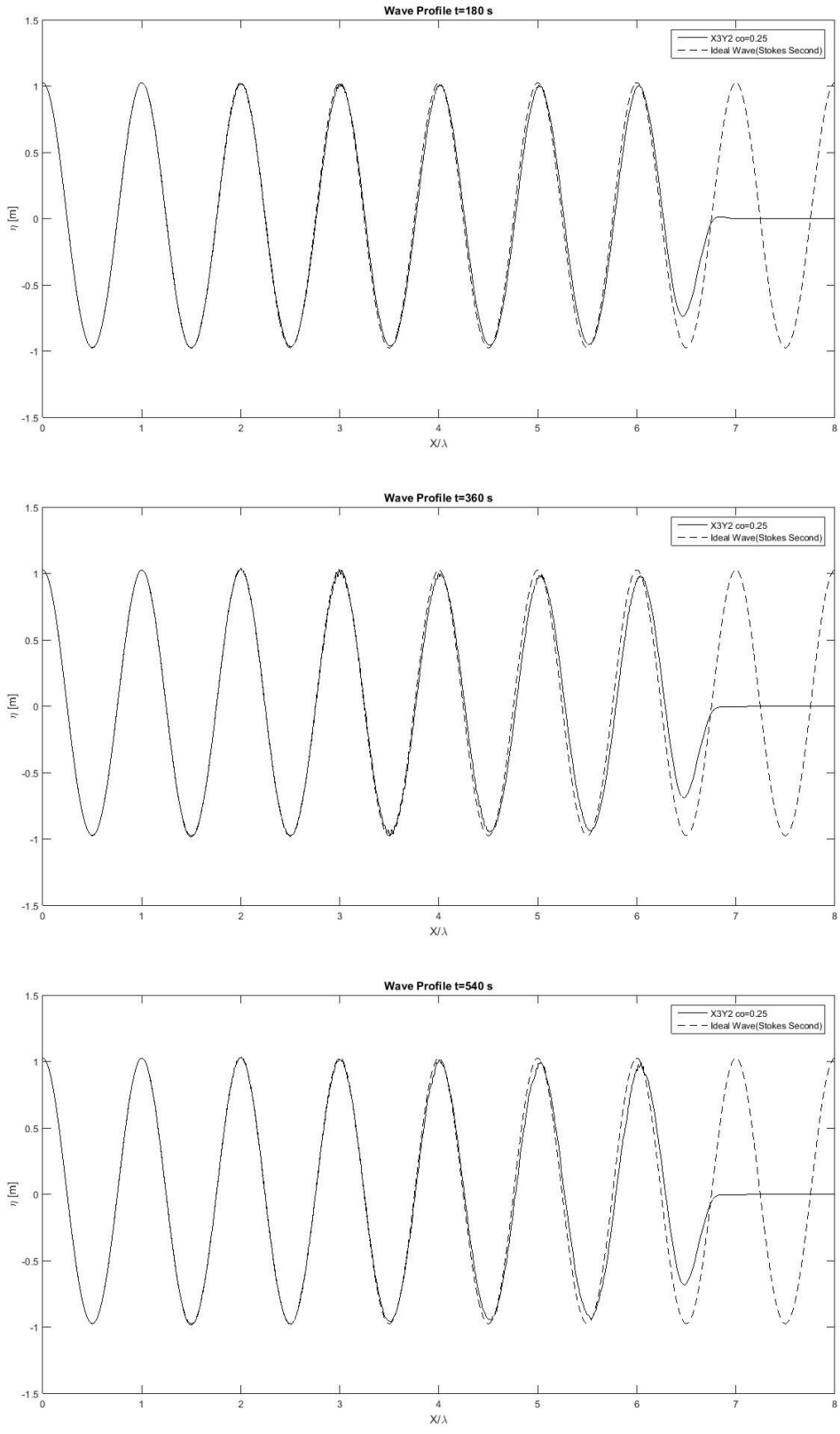

Figure 55 *Wave Profile for case X3Y2 Co=0.25*

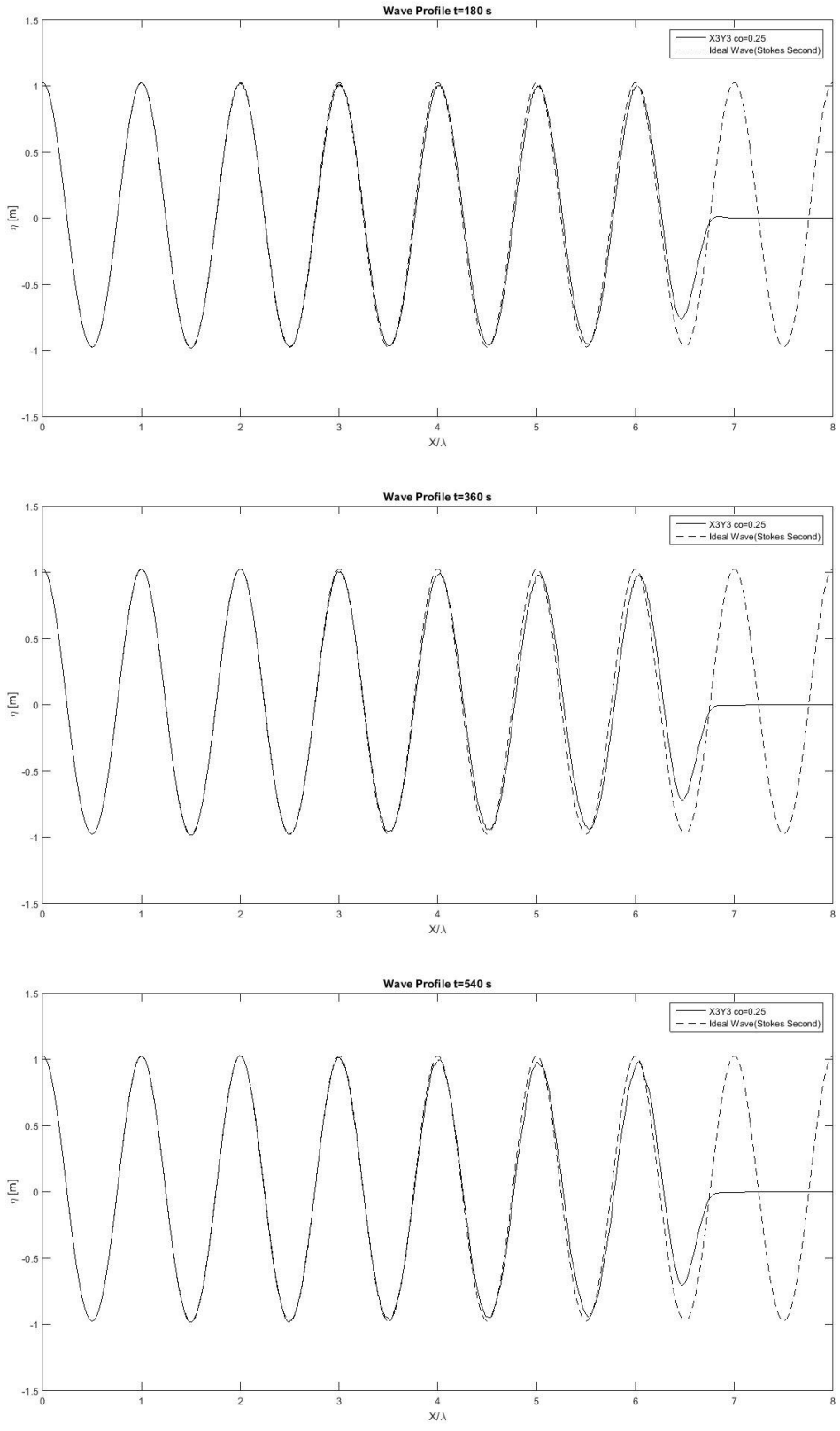

Figure 56 *Wave Profile for case X3Y3Co=0.25*

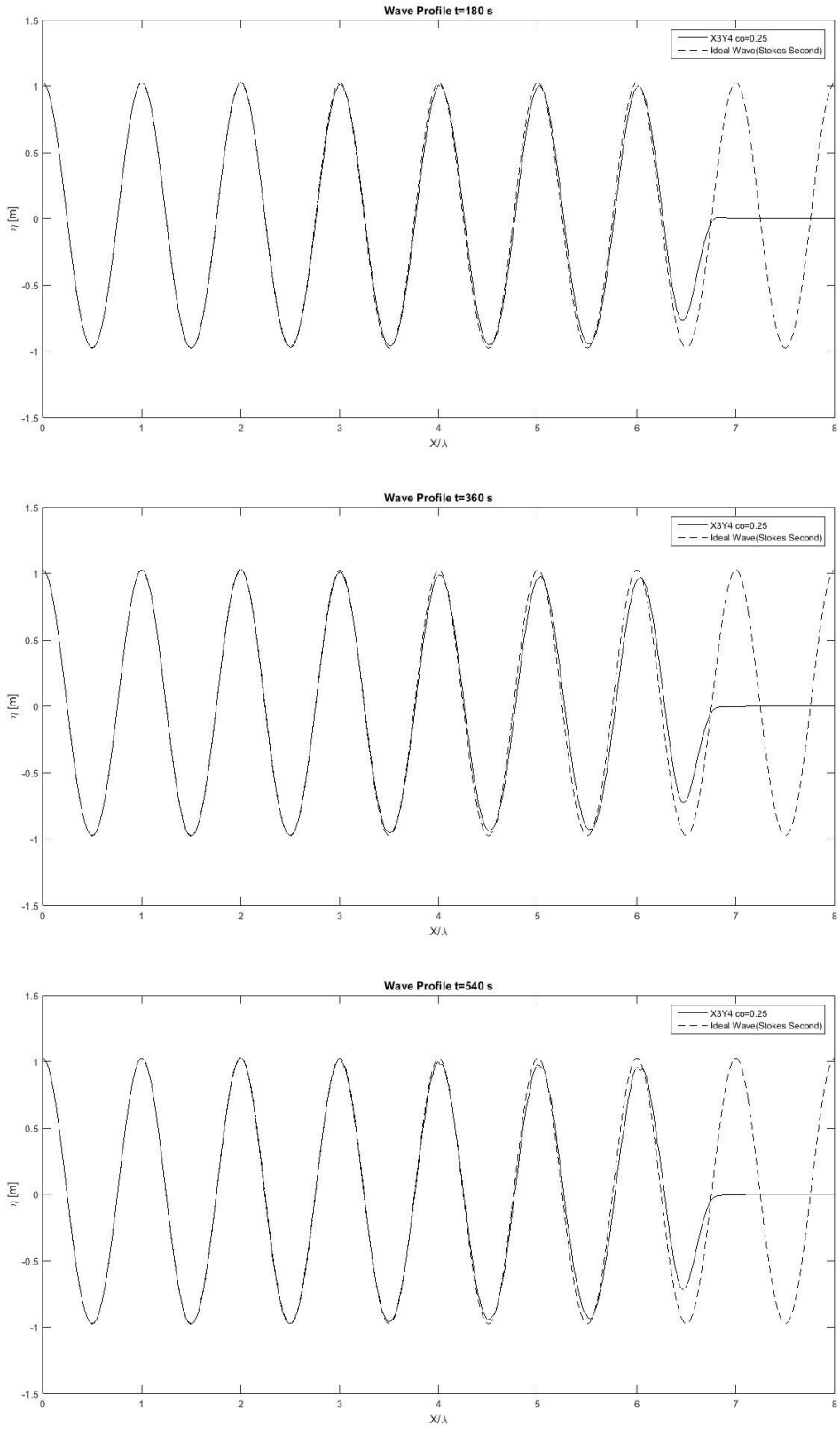

Figure 57 *Wave Profile for case X3Y4 Co=0.25*

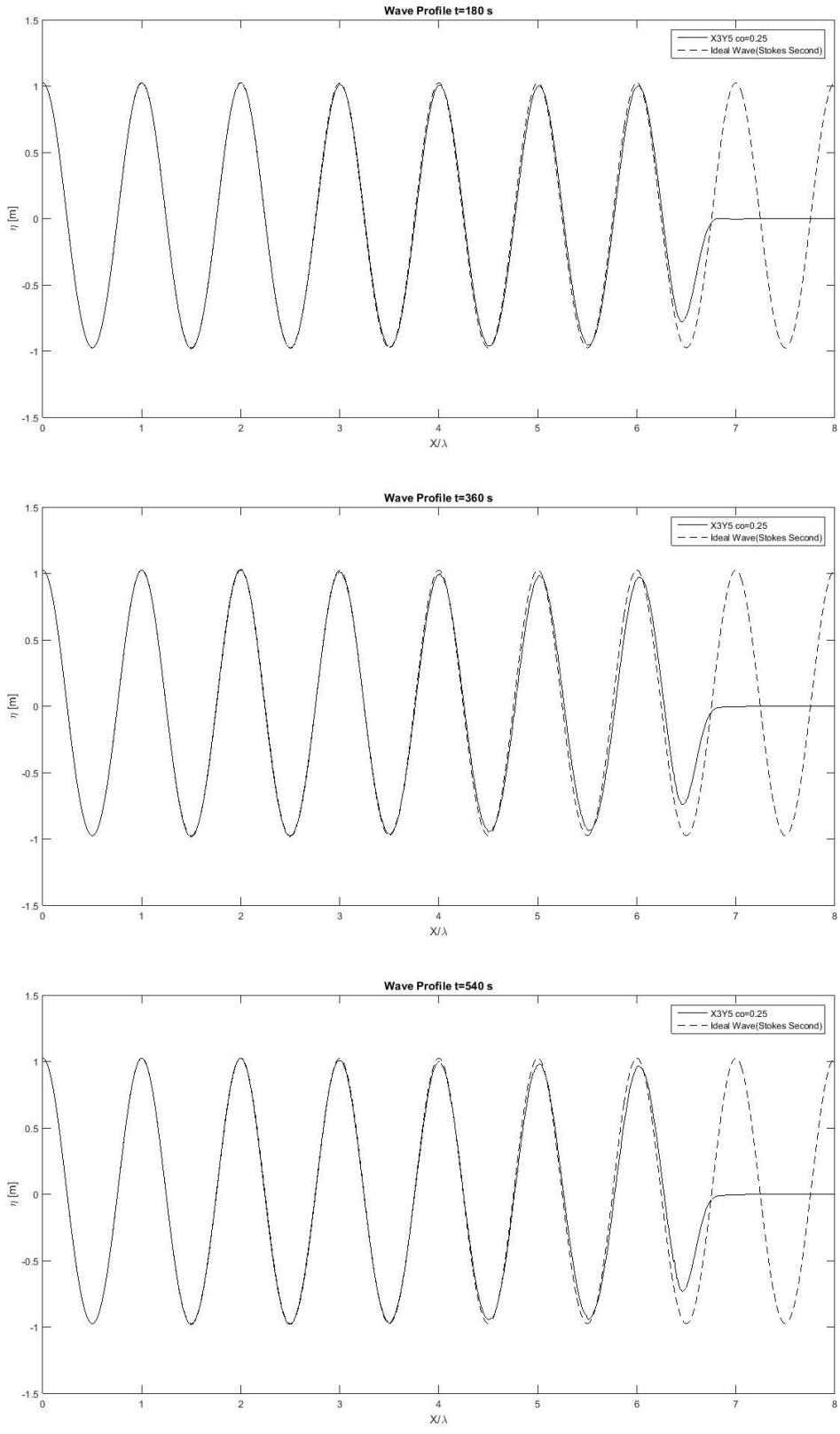

Figure 58 *Wave Profile for case X3Y5 Co=0.25*

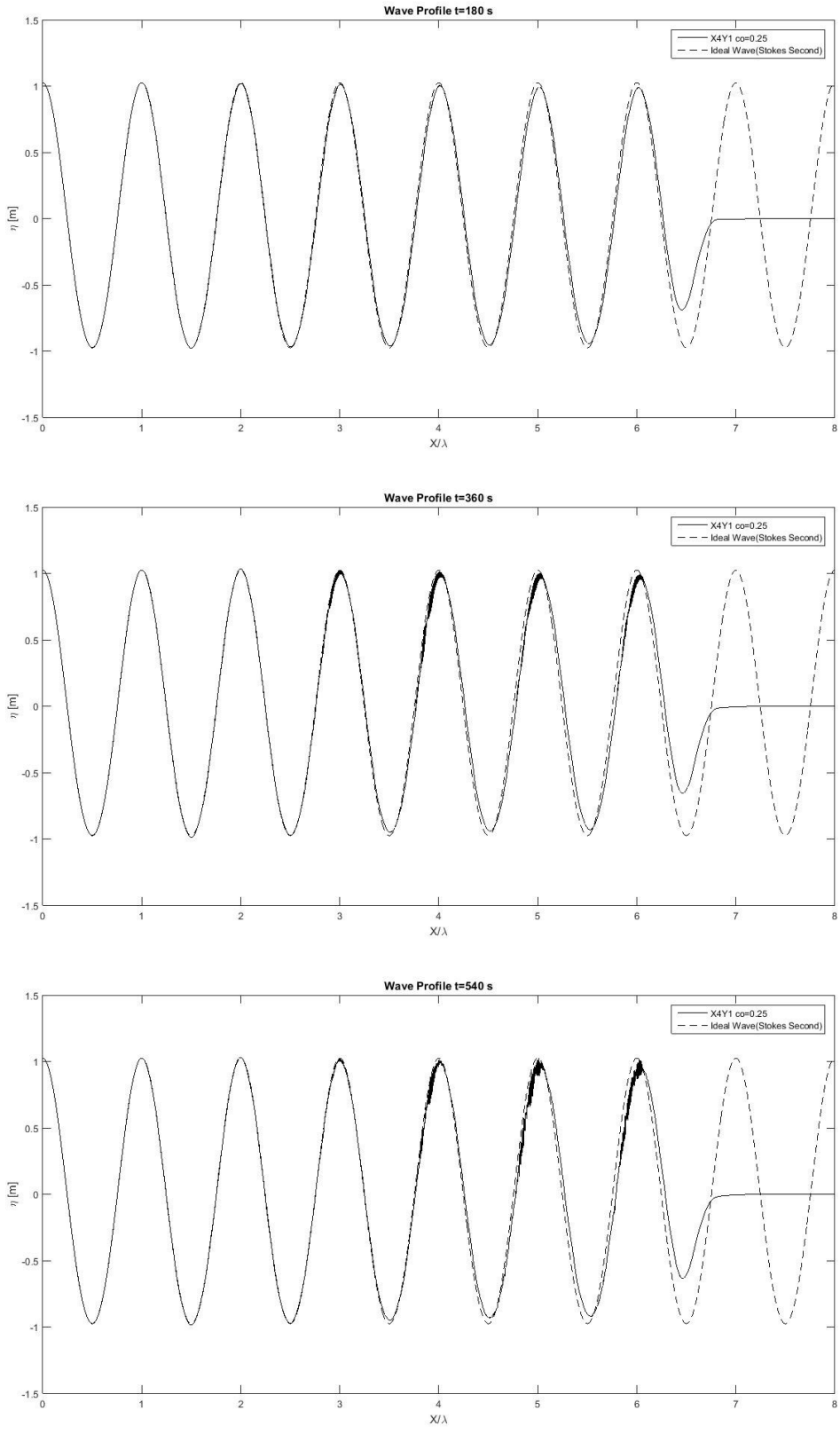

Figure 59 *Wave Profile for case X4Y1 Co=0.25*

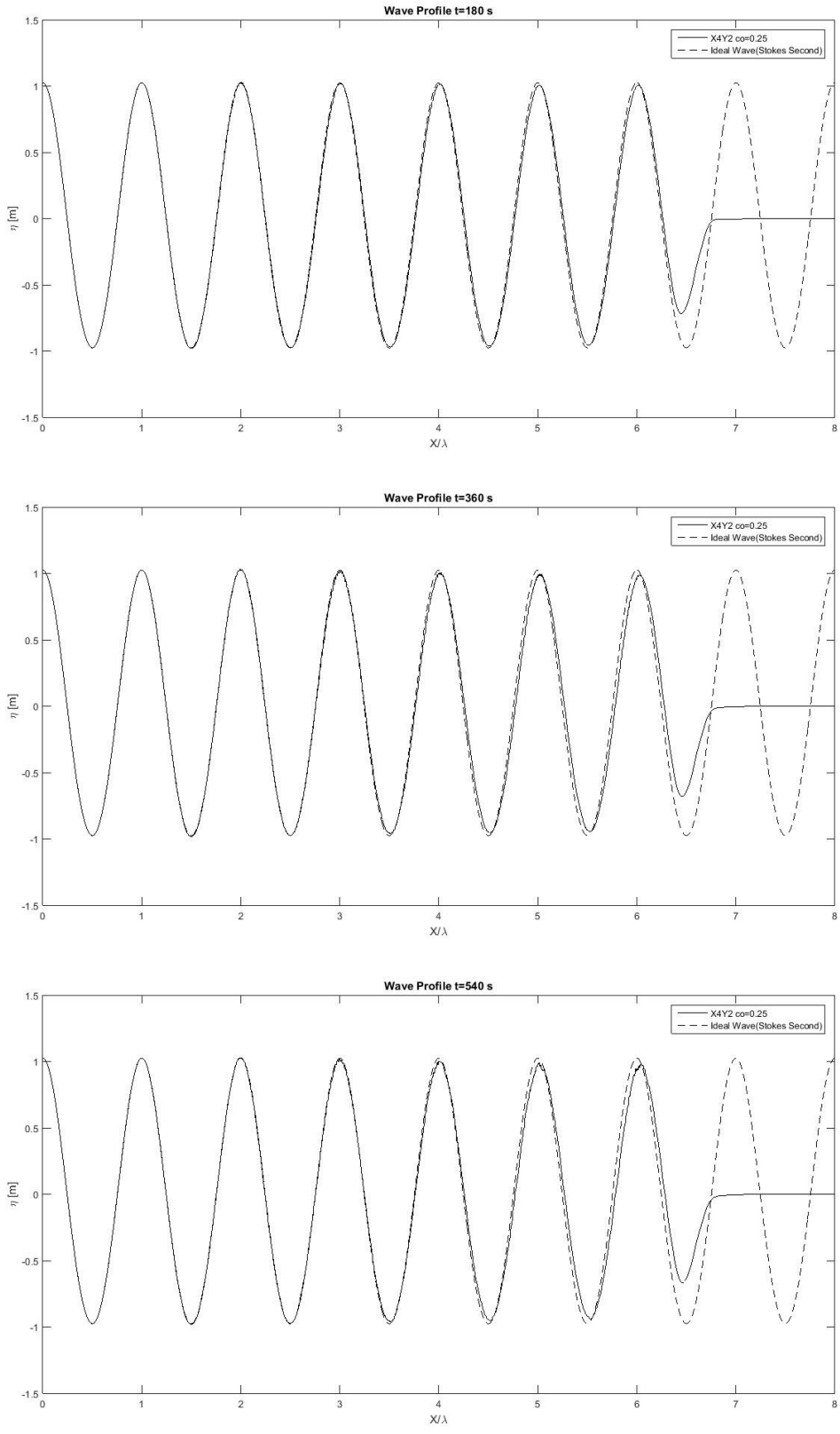

Figure 60 *Wave Profile for case X4Y2 Co=0.25*

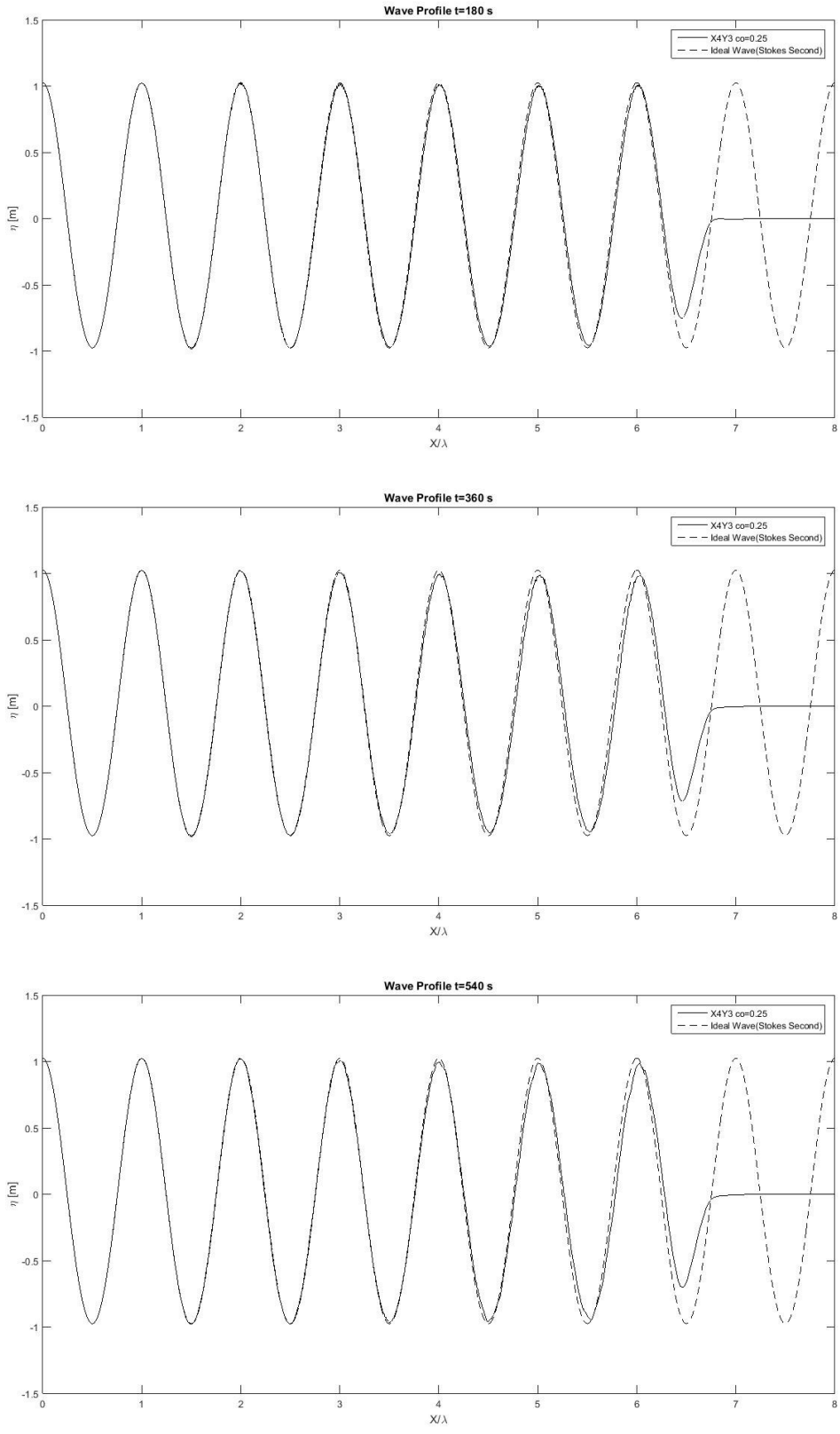

Figure 61 *Wave Profile for case X4Y3 Co=0.25*

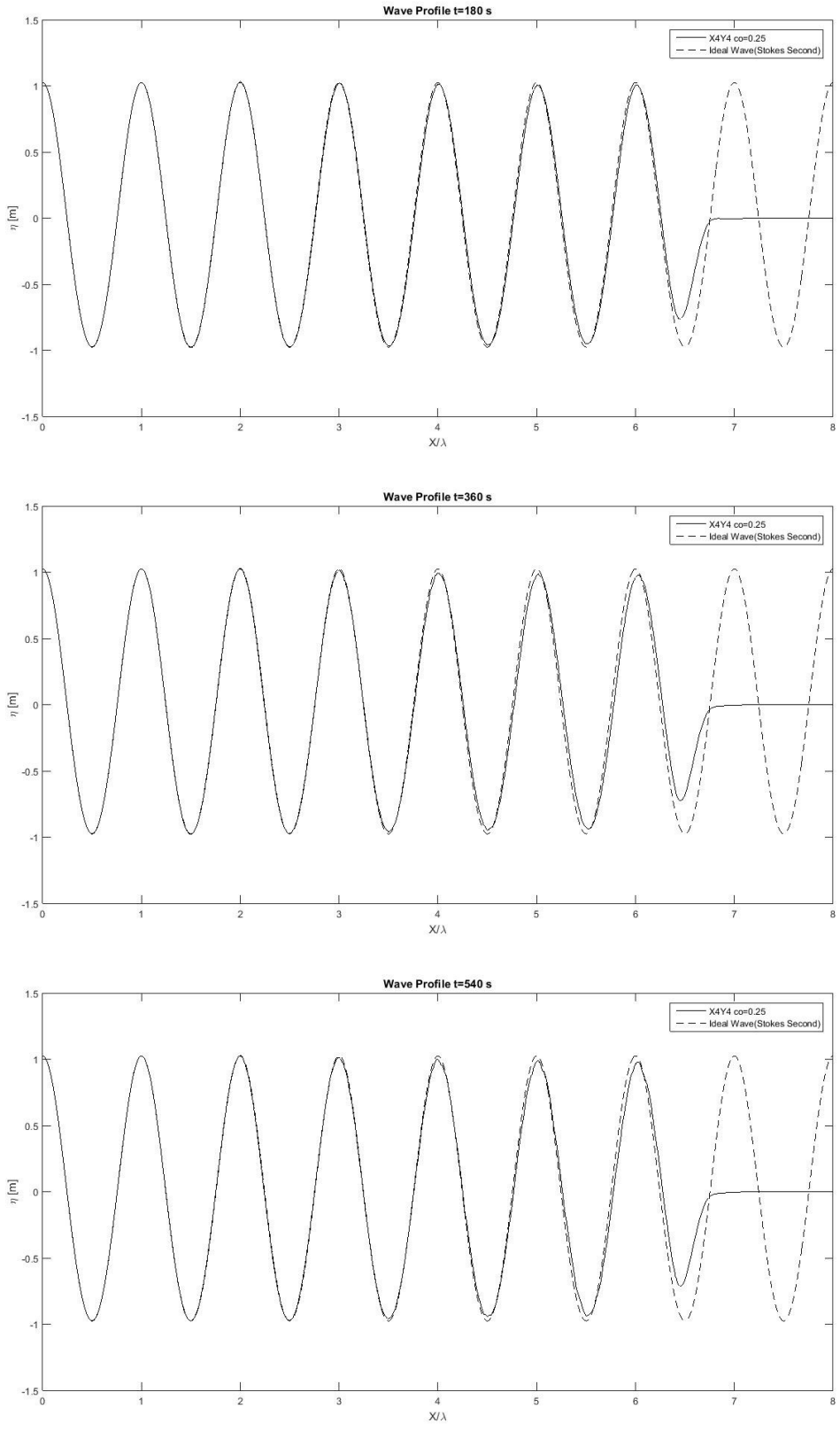

Figure 62 *Wave Profile for case X4Y4 Co=0.25*

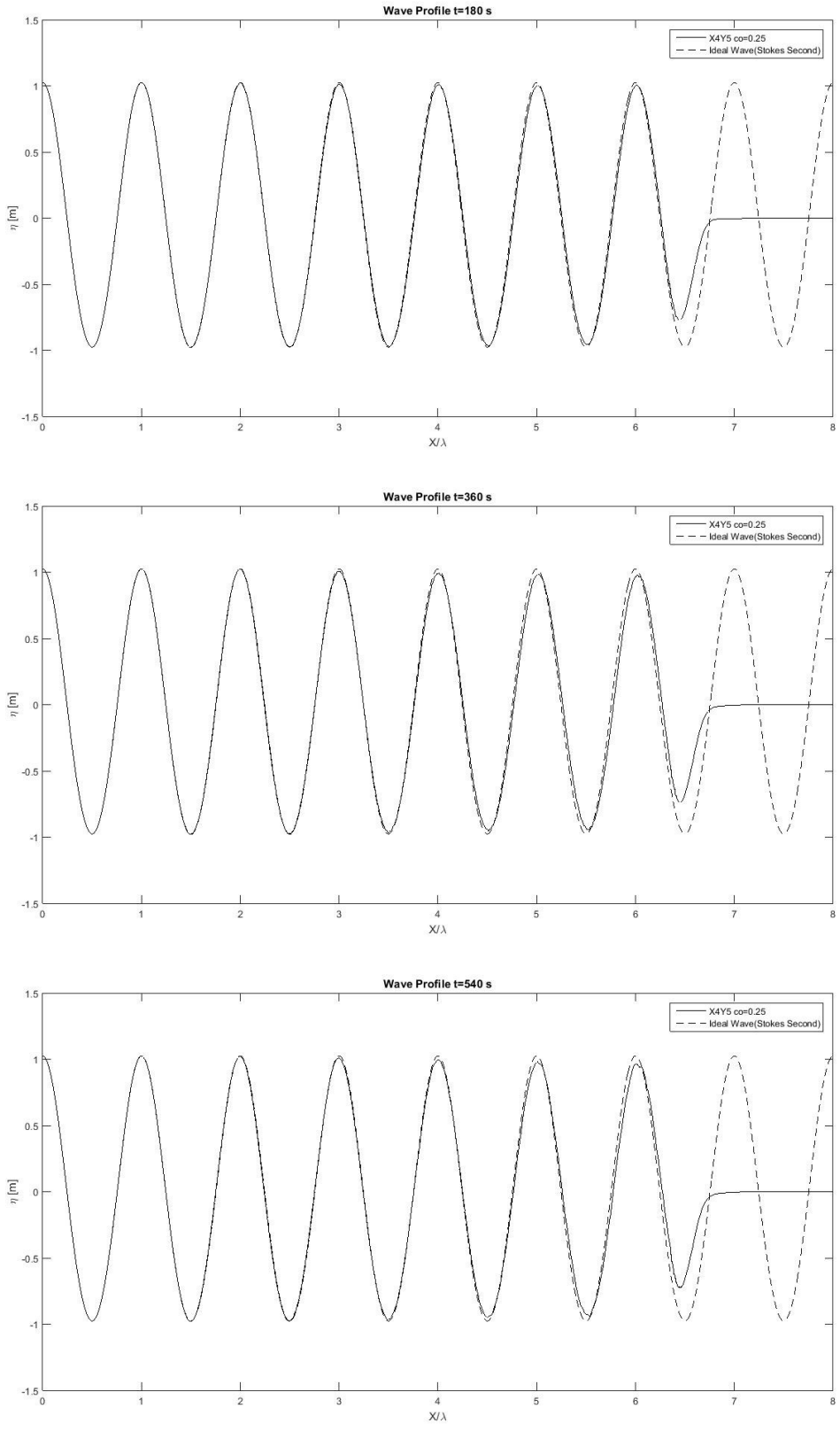

Figure 63 *Wave Profile for case X4Y5 Co=0.25*

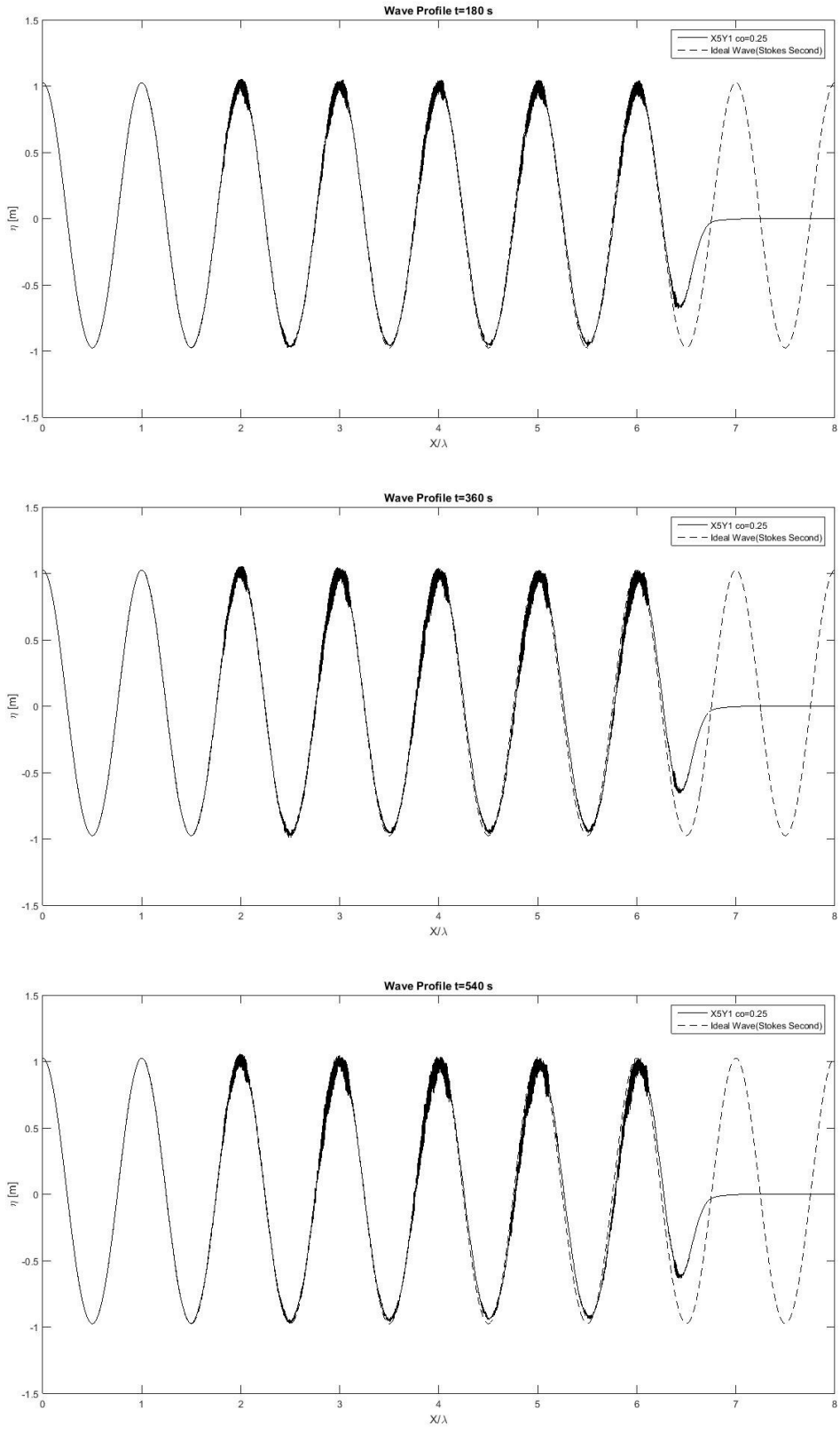

Figure 64 *Wave Profile for case X5Y1 Co=0.25*

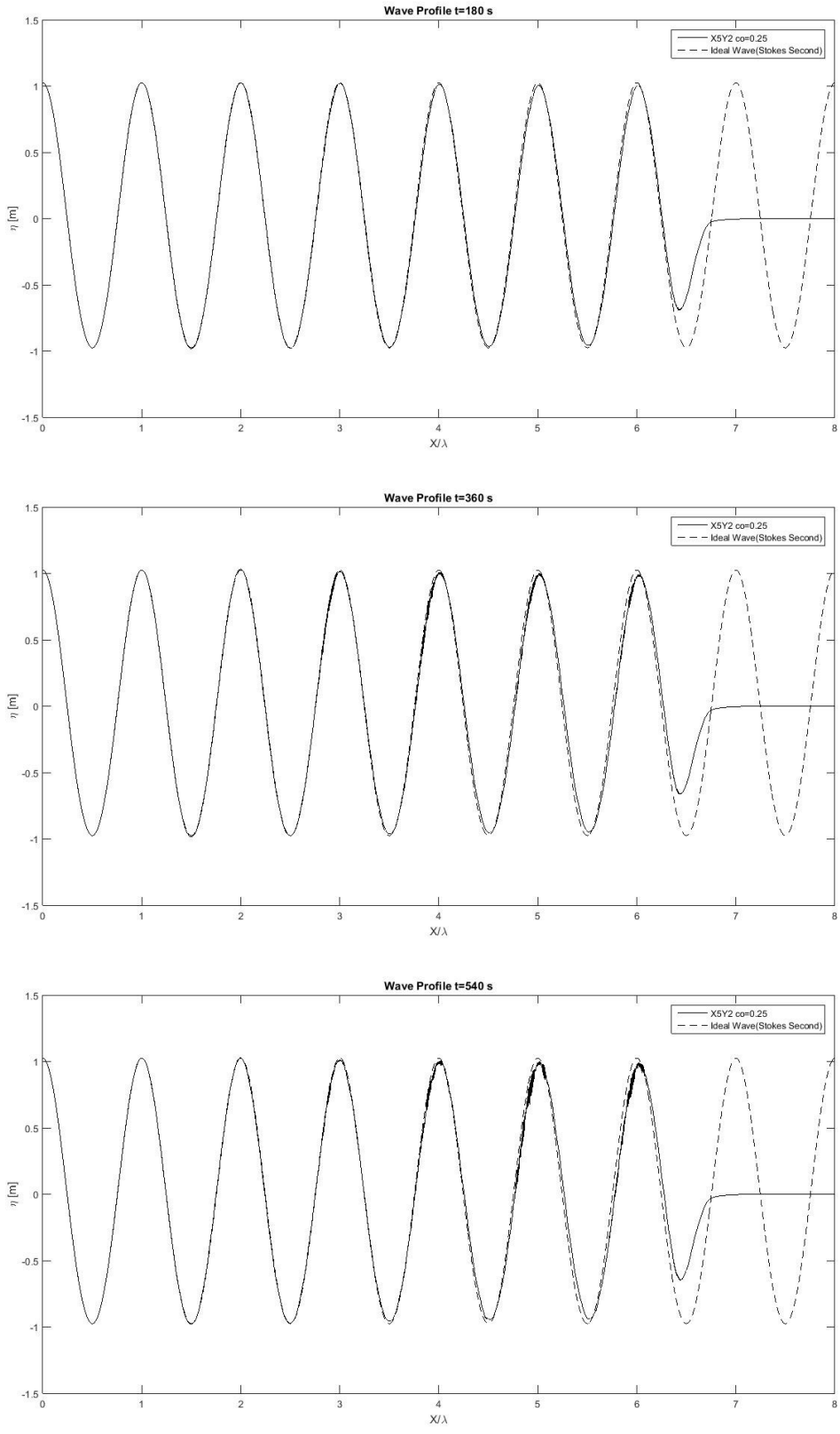

Figure 65 *Wave Profile for case X5Y2 Co=0.25*

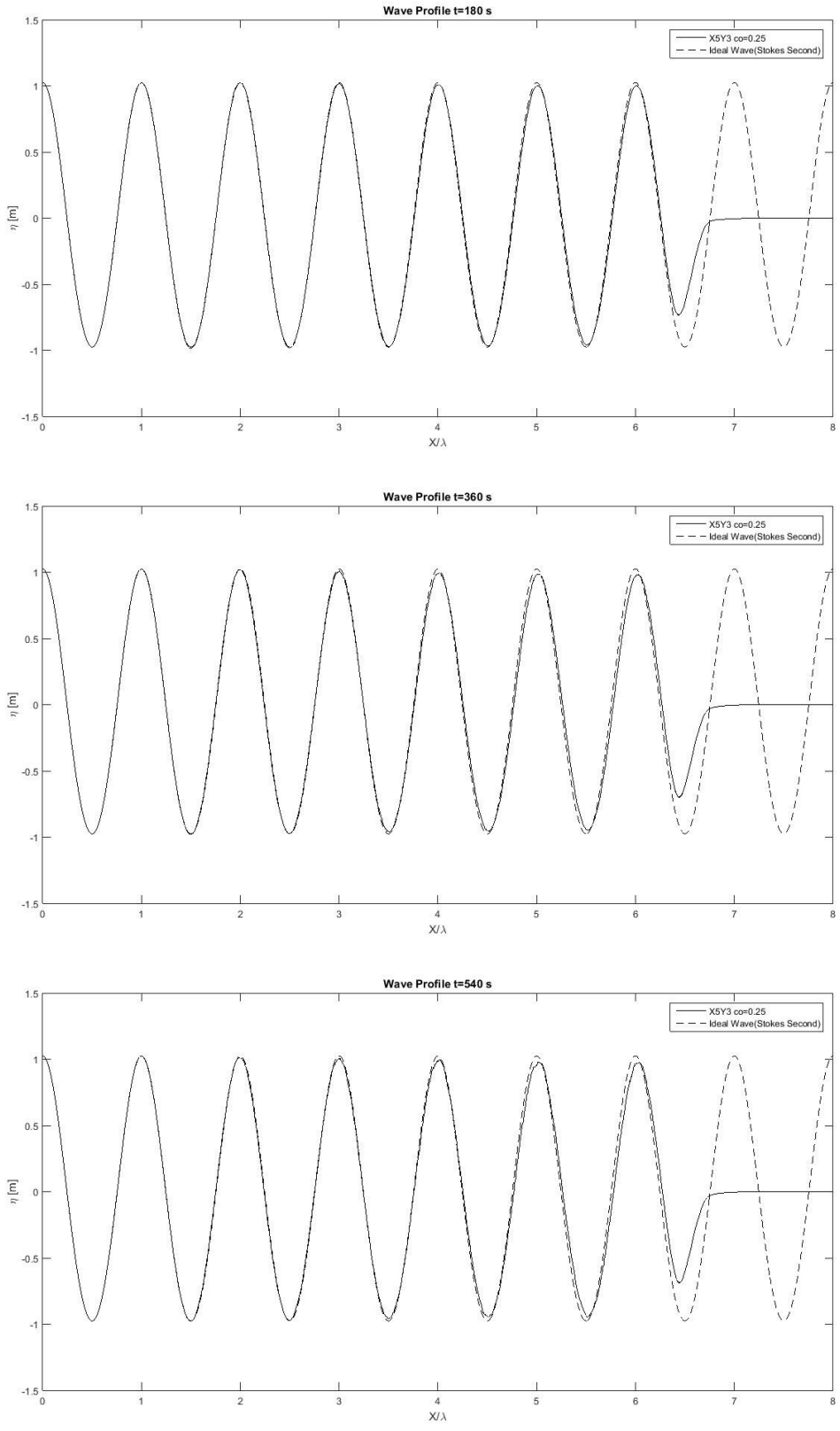

Figure 66 *Wave Profile for case X5Y3Co=0.25*

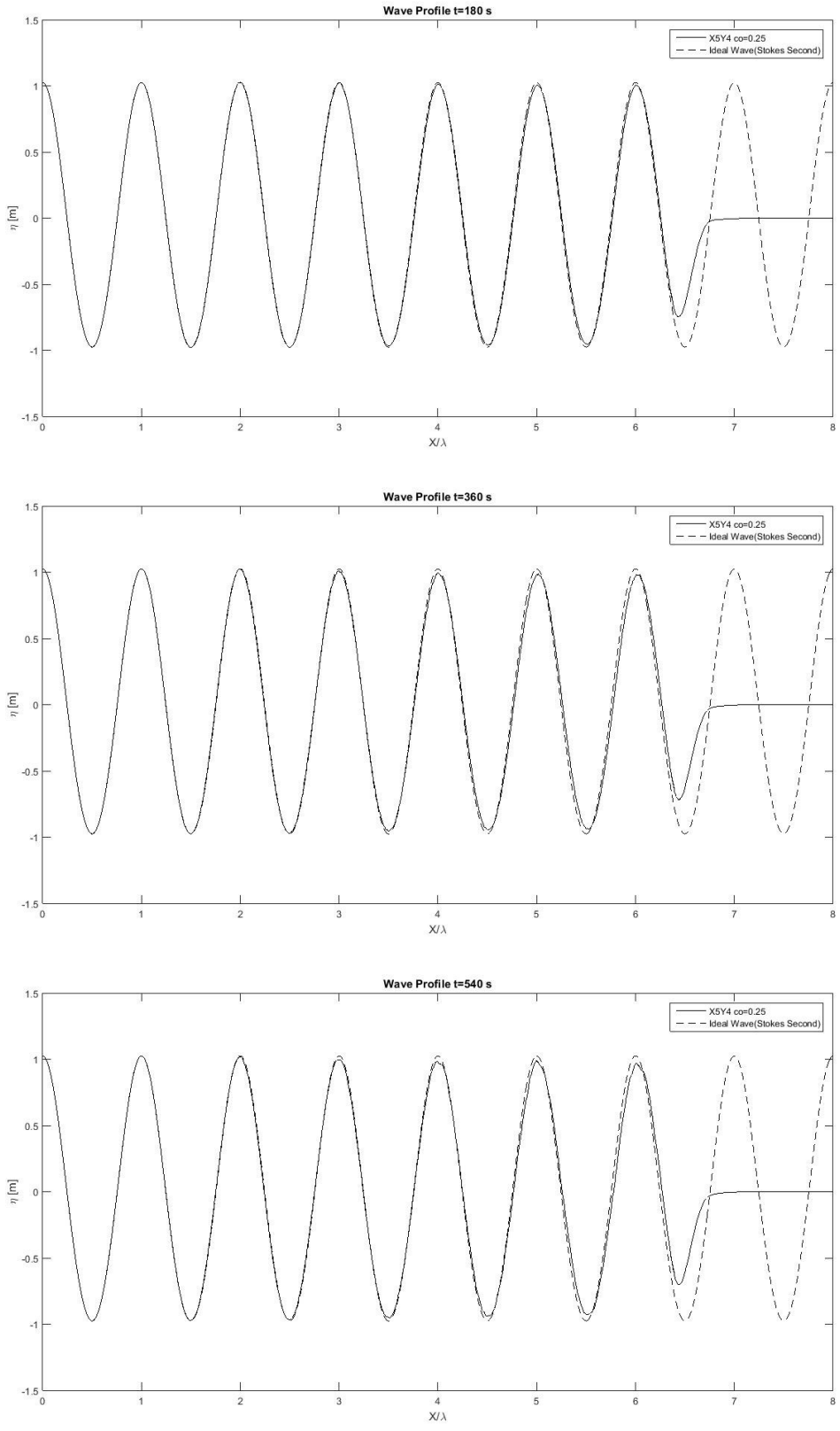

Figure 67 *Wave Profile for case X5Y4 Co=0.25*

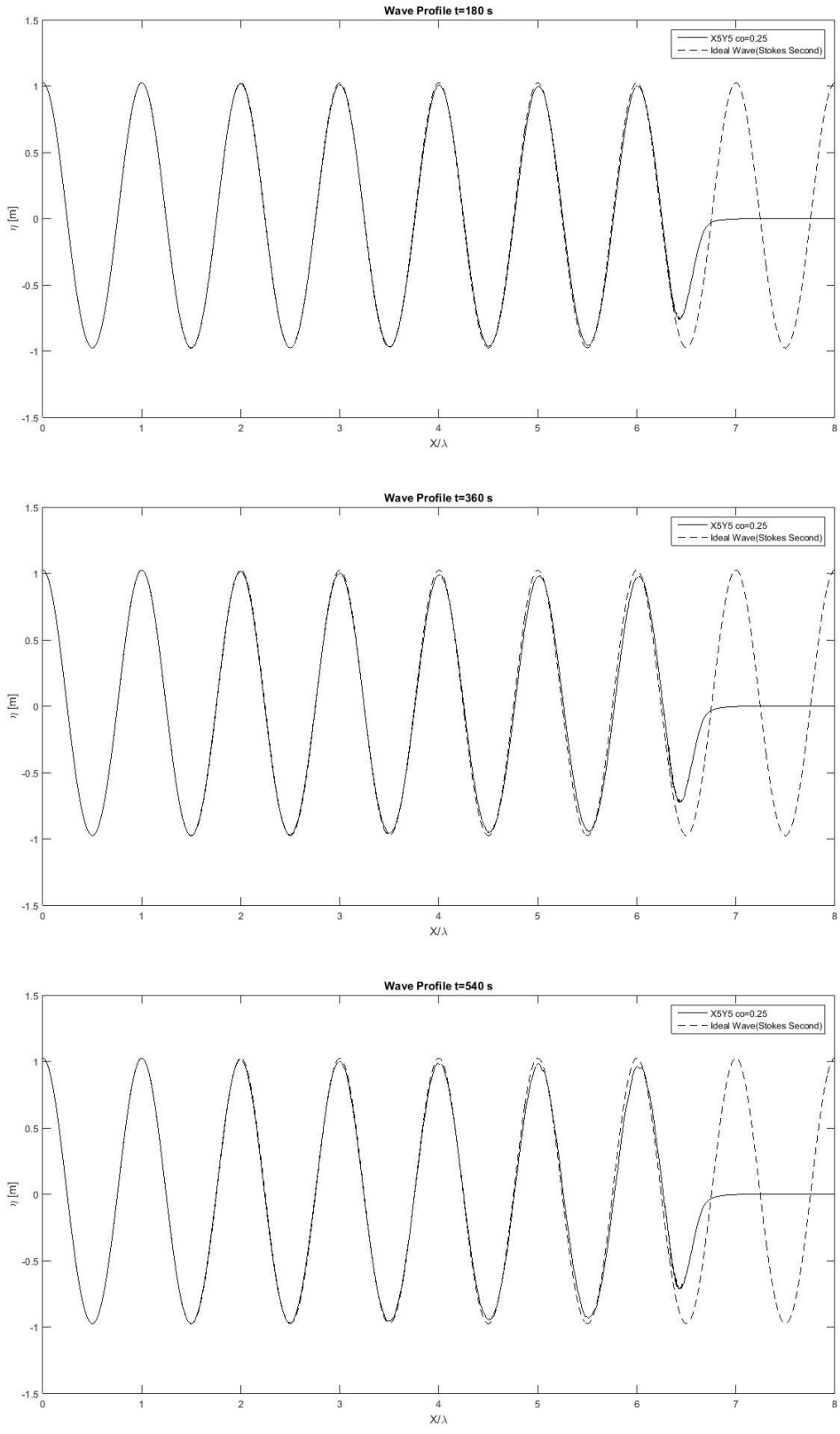

Figure 68 *Wave Profile for case X5Y5 Co=0.25*

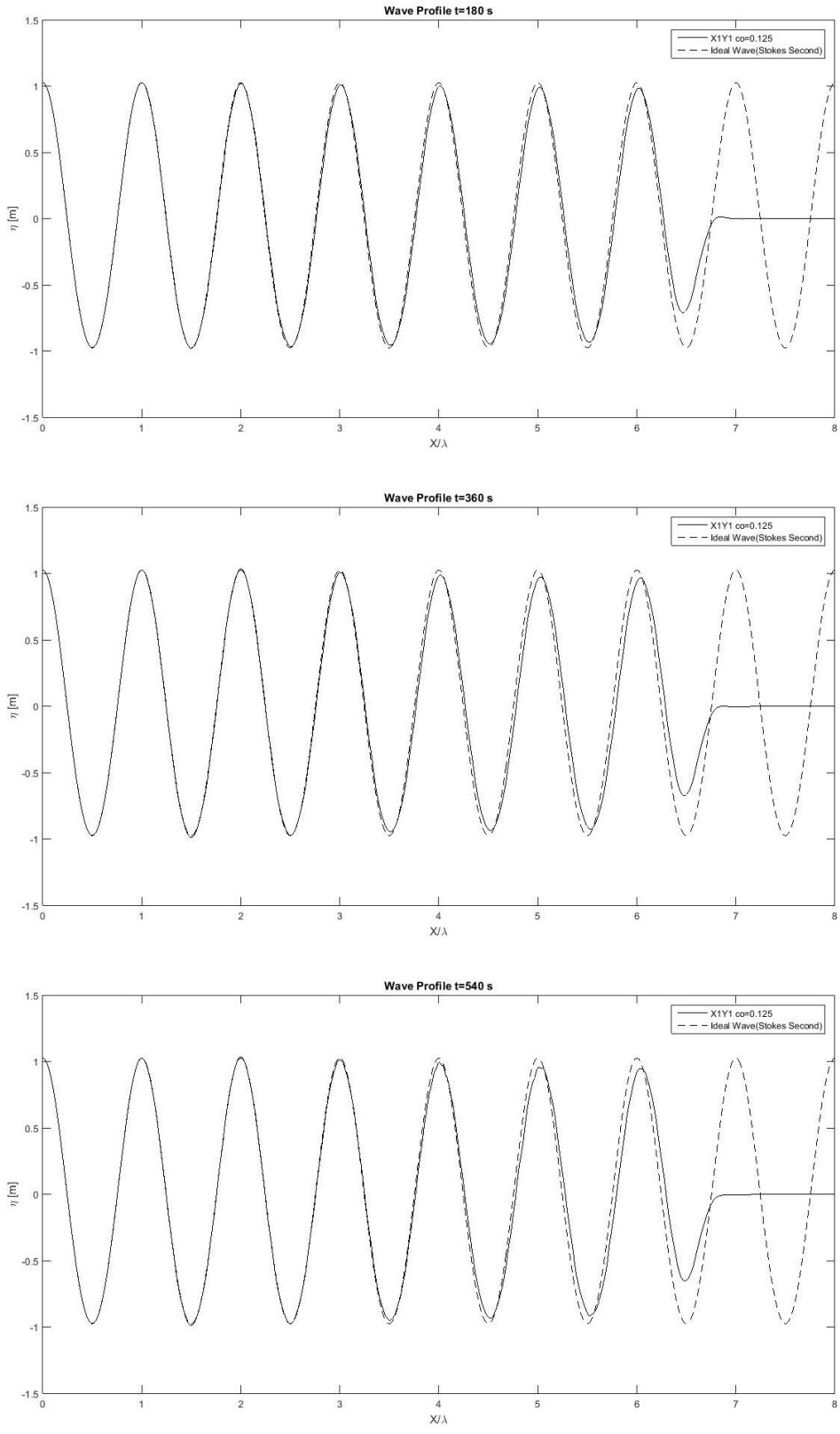

Figure 69 *Wave Profile for case X1Y1 Co=0.125*

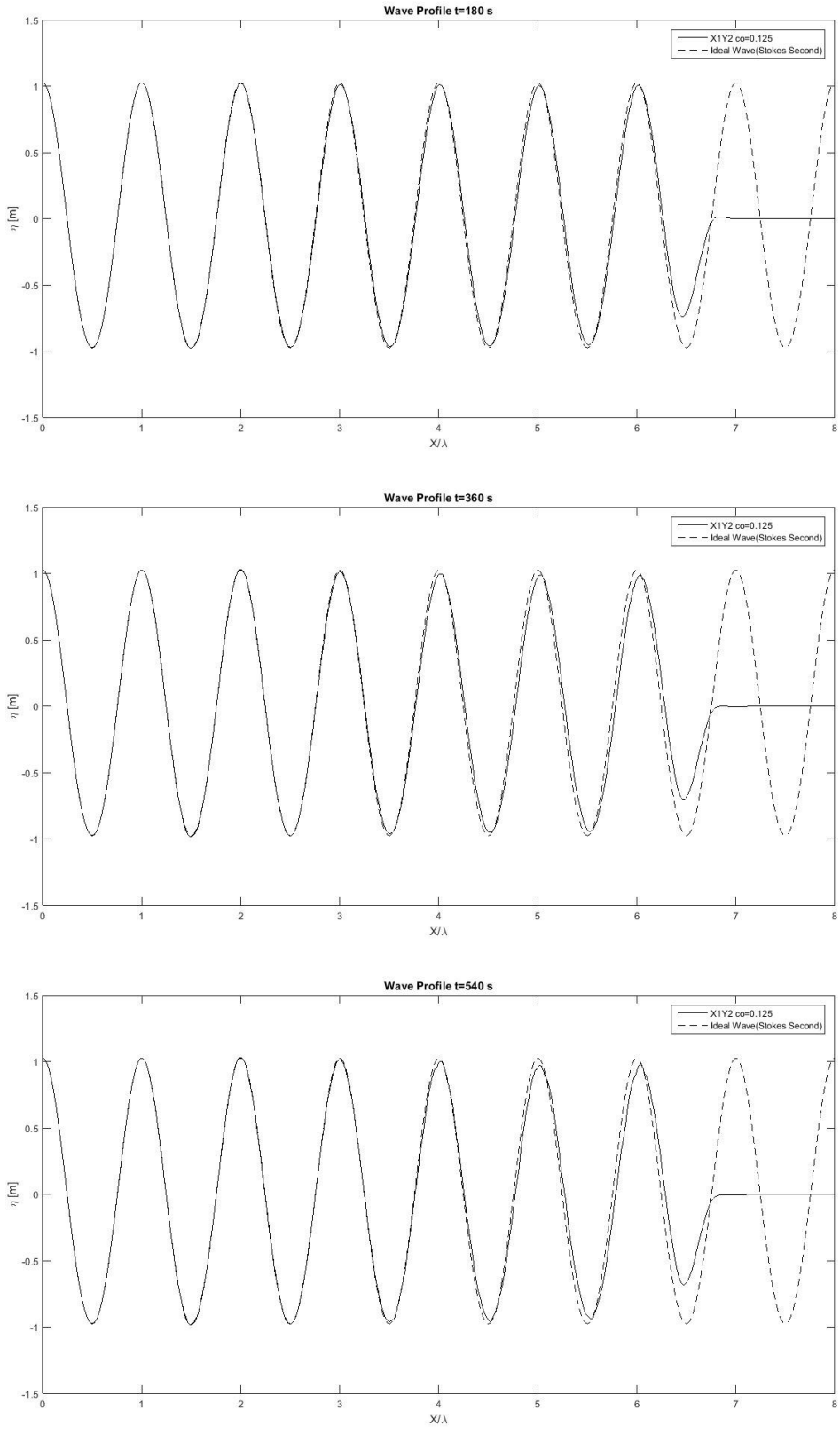

Figure 70 *Wave Profile for case X1Y2 Co=0.125*

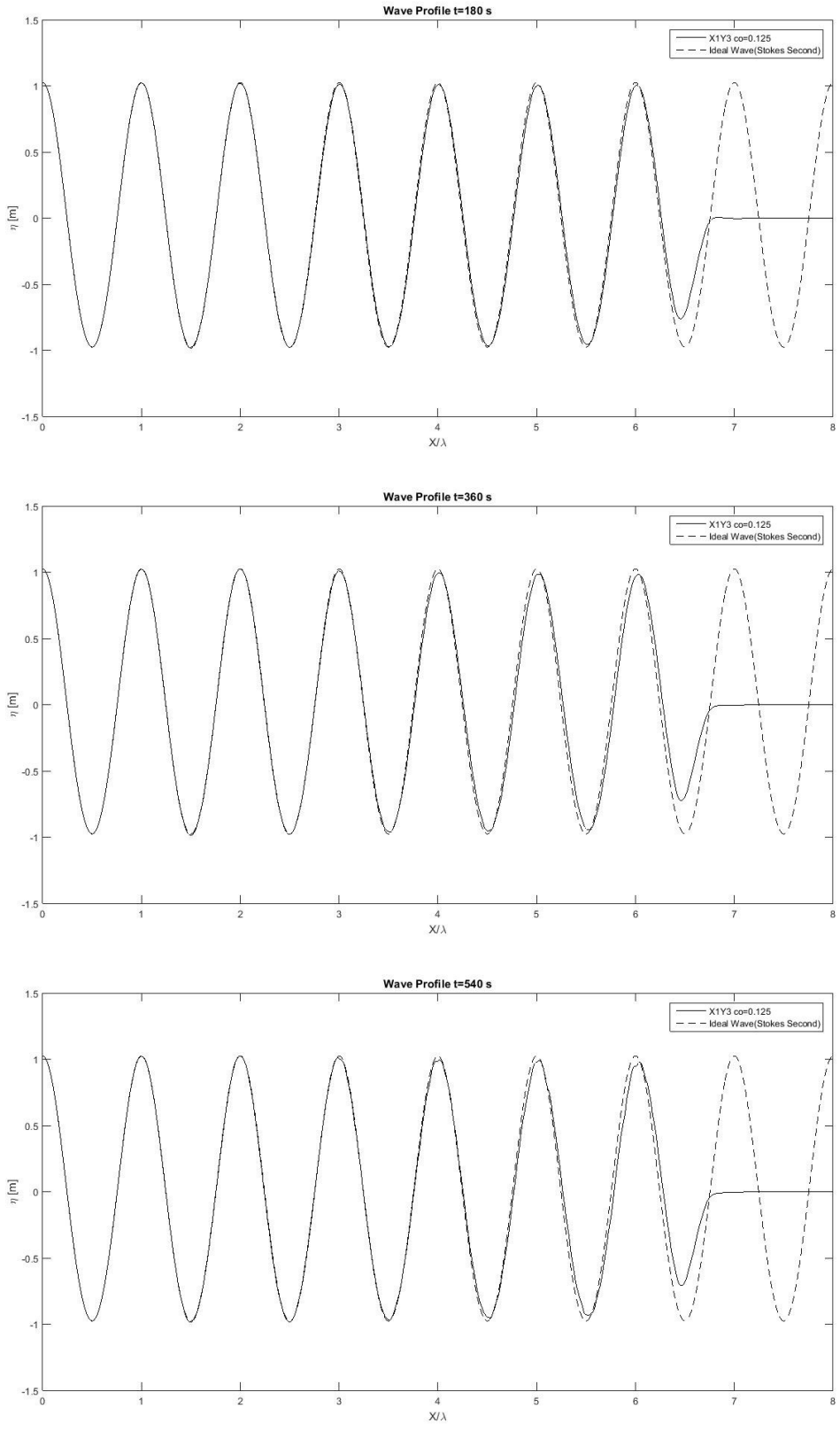

Figure 71 *Wave Profile for case X1Y3 Co=0.125*

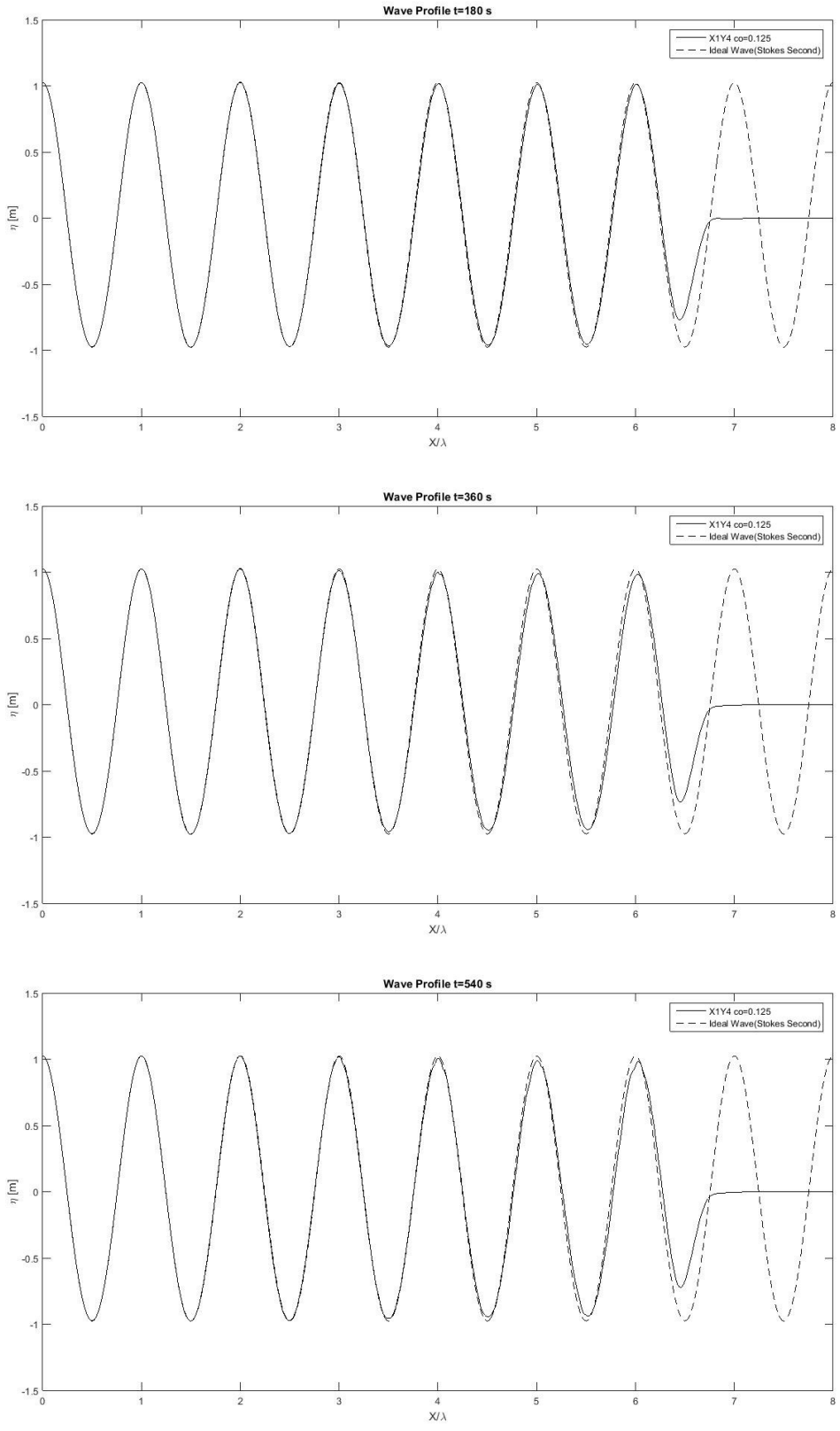

Figure 72 *Wave Profile for case X1Y4Co=0.125*

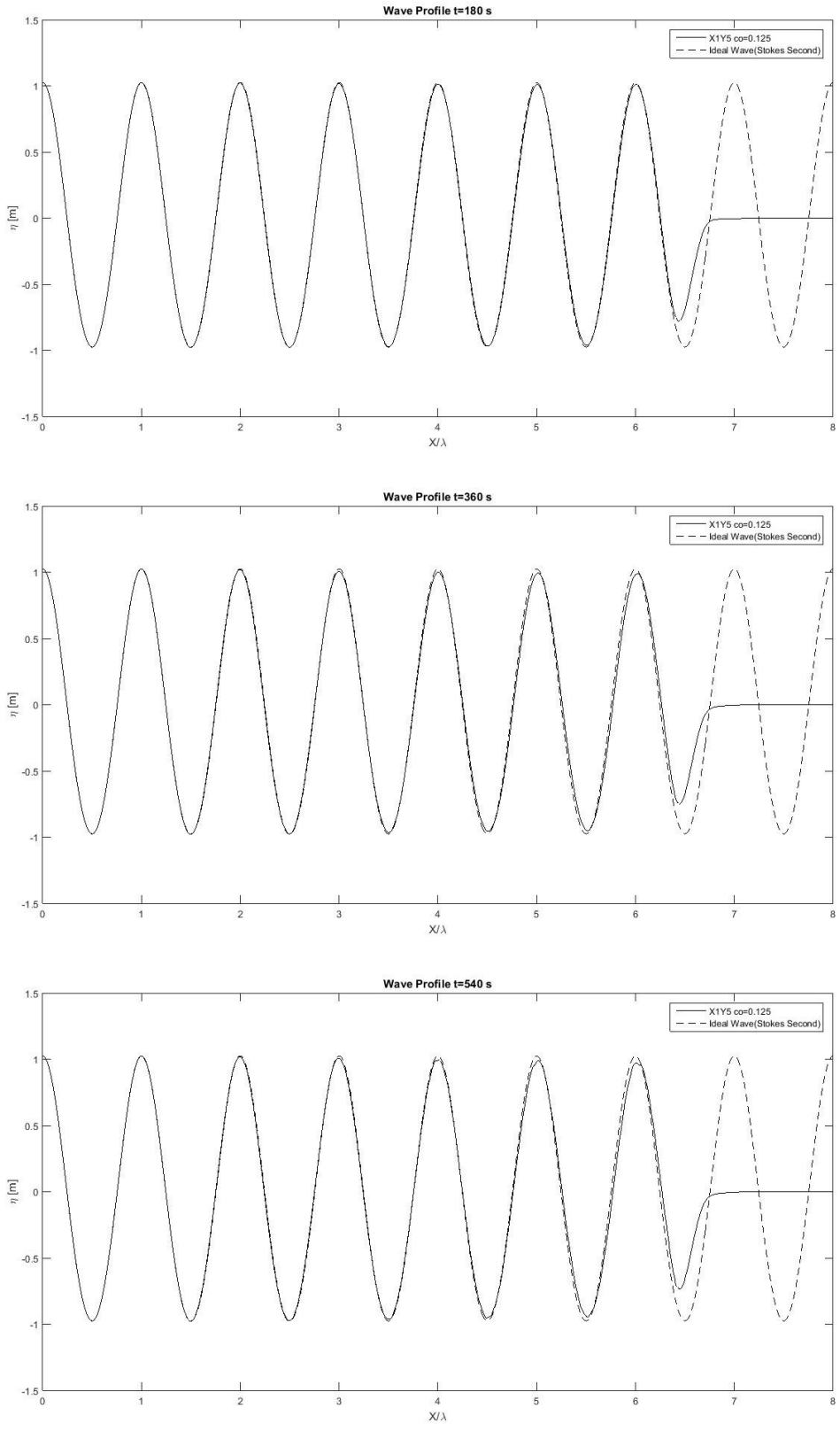

Figure 73 *Wave Profile for case X1Y5 Co=0.125*

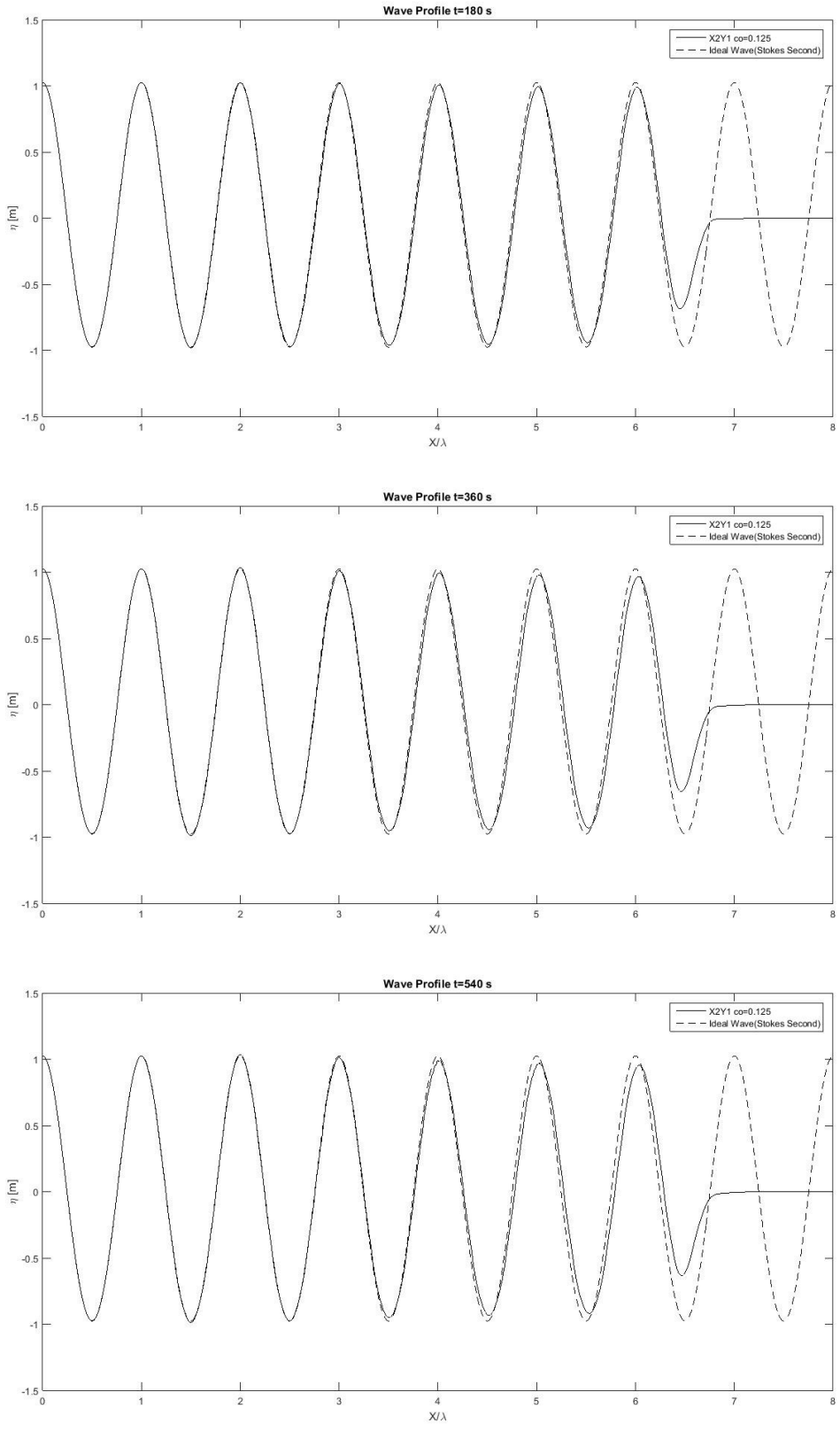

Figure 74 *Wave Profile for case X2Y1 Co=0.125*

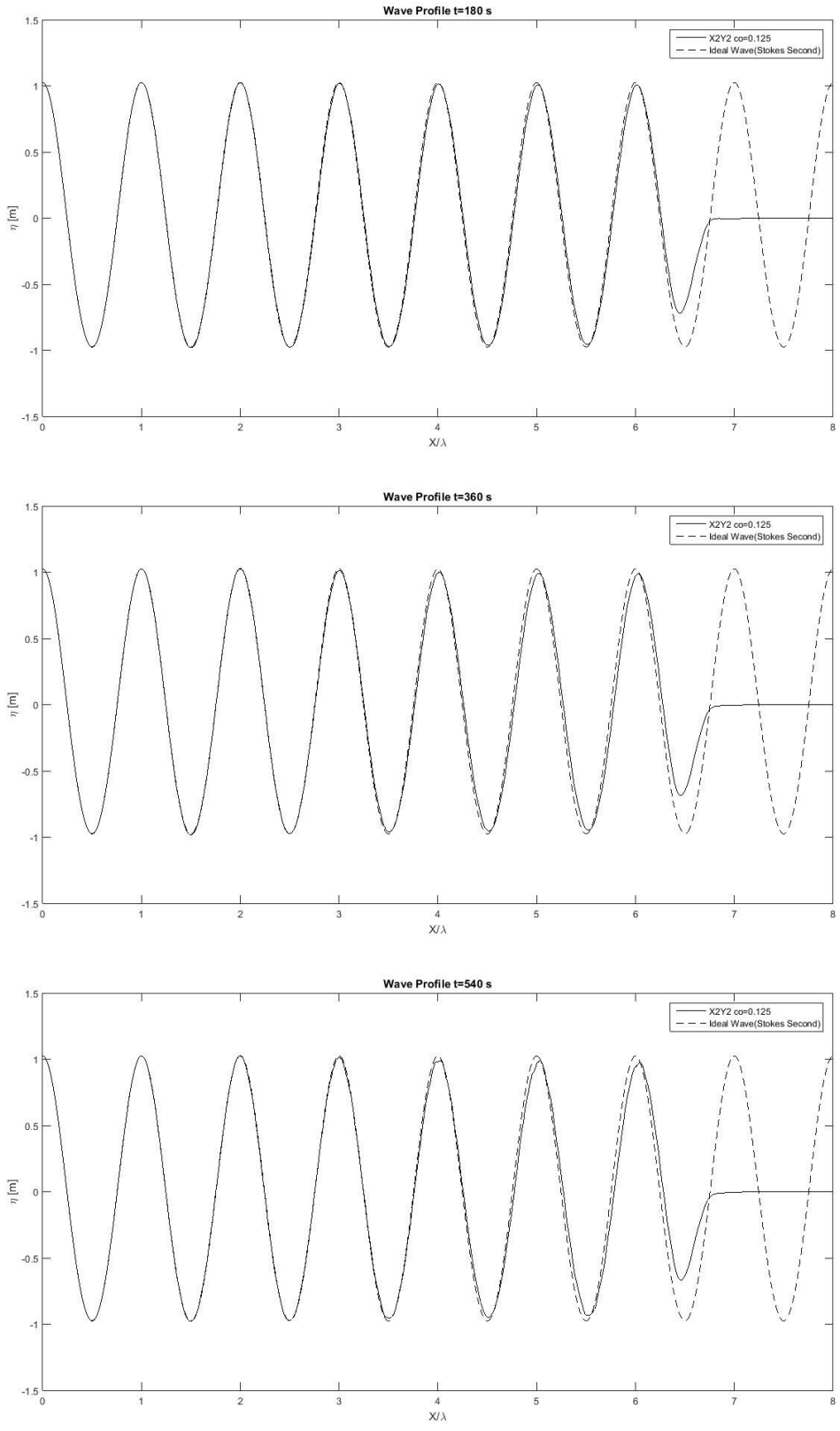

Figure 75 *Wave Profile for case X2Y2Co=0.125*

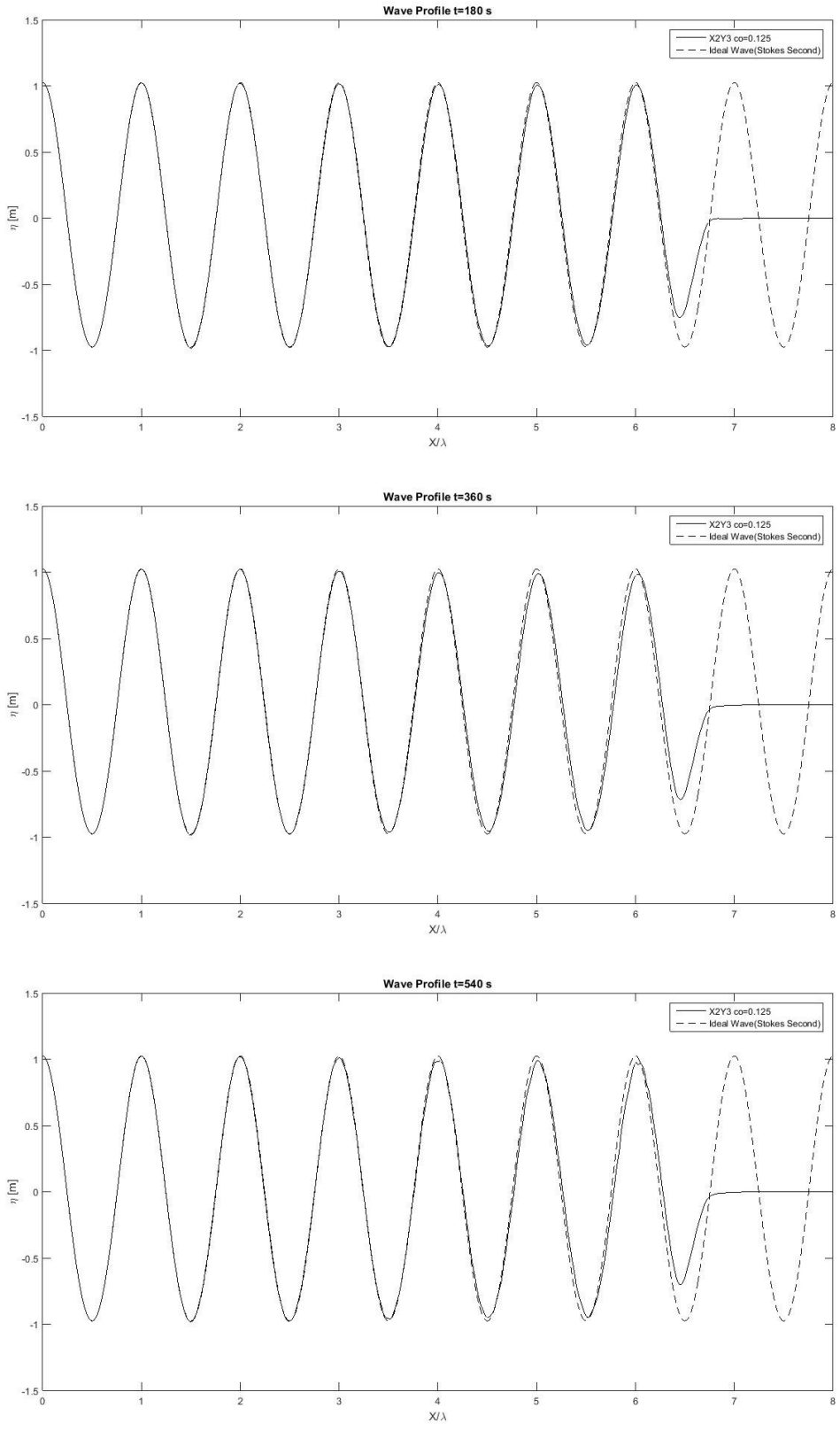

Figure 76 *Wave Profile for case X2Y3 Co=0.125*

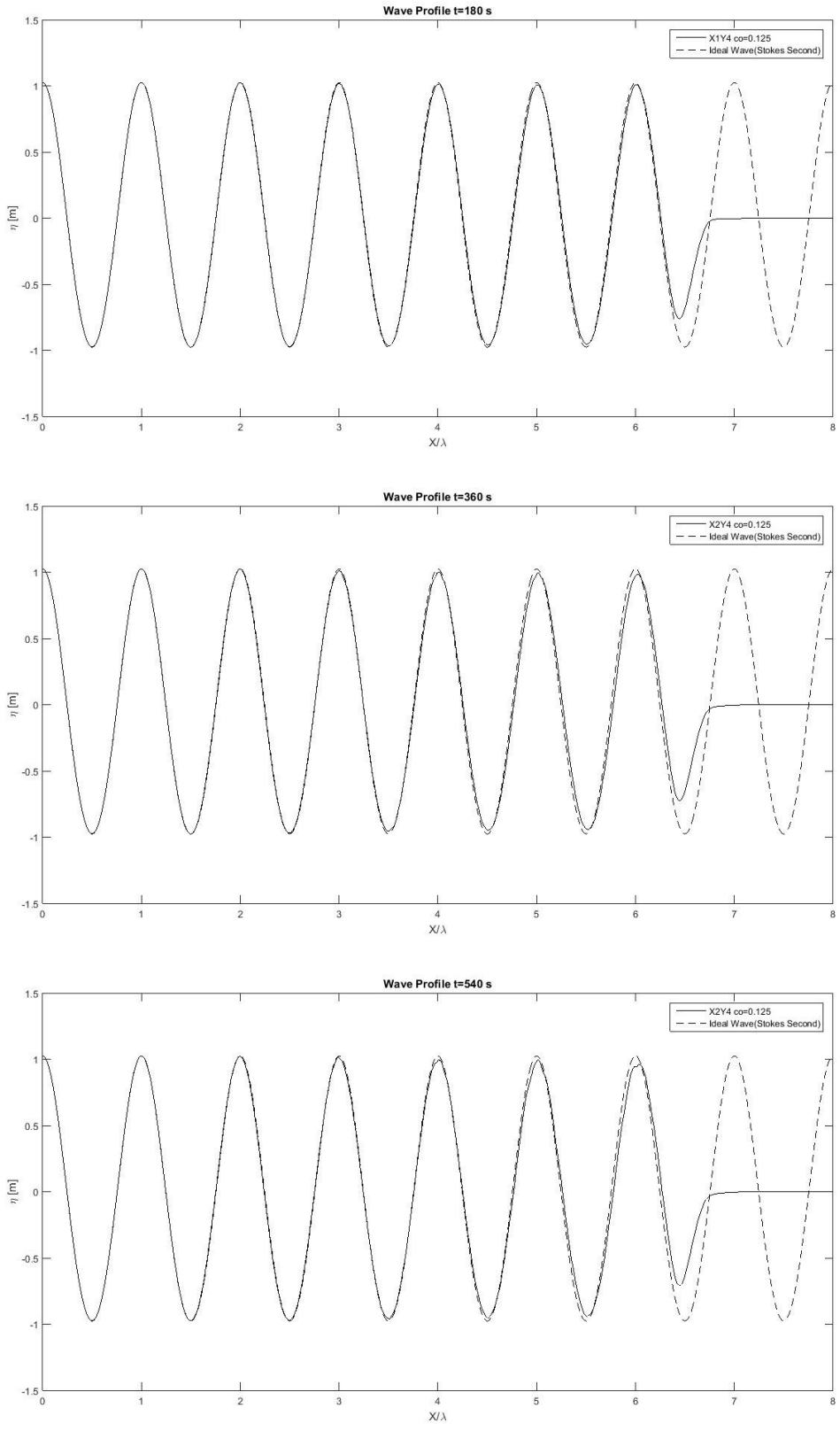

Figure 77 *Wave Profile for case X2Y4 Co=0.125*

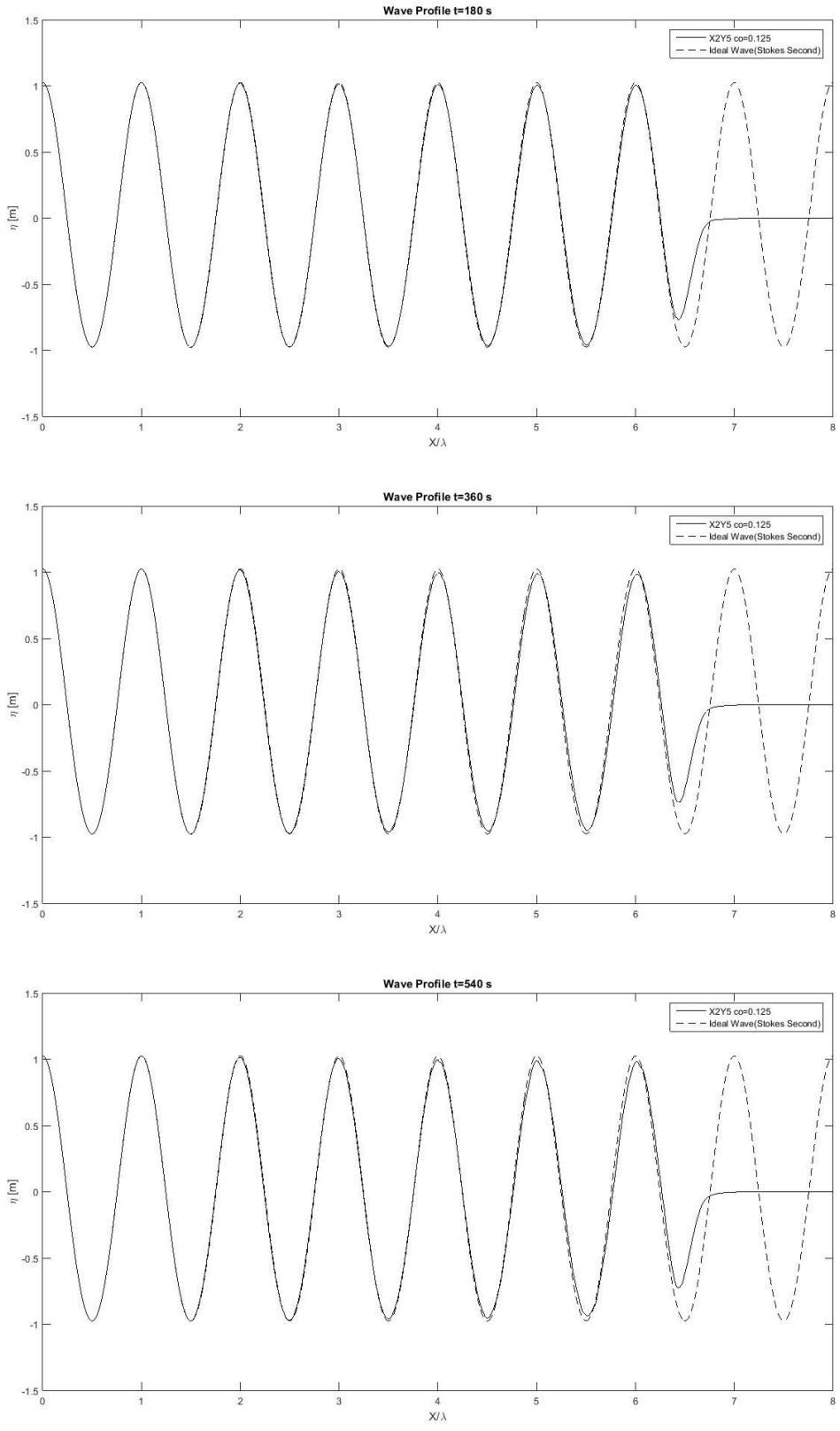

Figure 78 *Wave Profile for case X2Y5 Co=0.125*

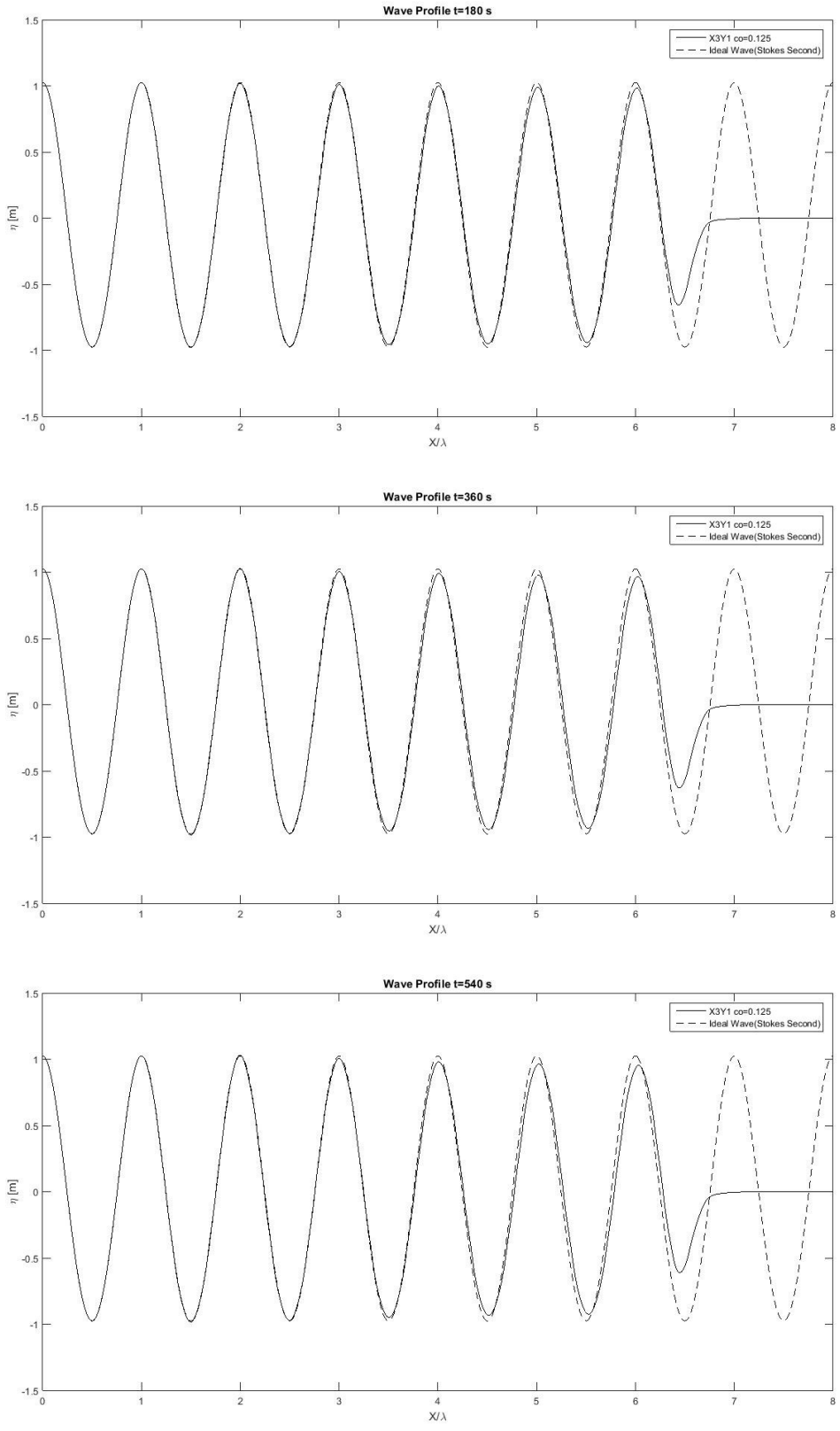

Figure 79 *Wave Profile for case X3Y1 Co=0.125*

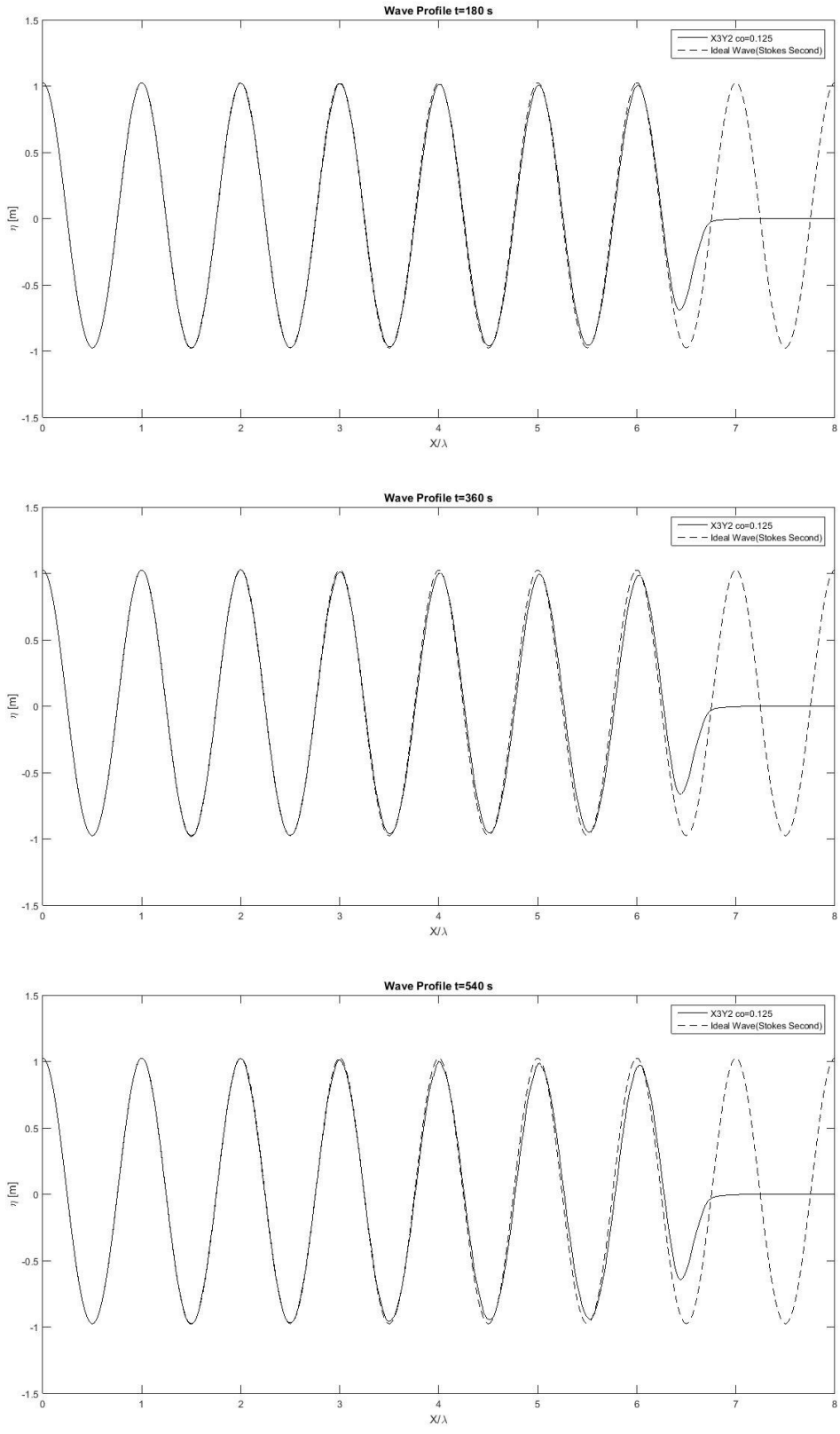

Figure 80 *Wave Profile for case X3Y2 Co=0.125*

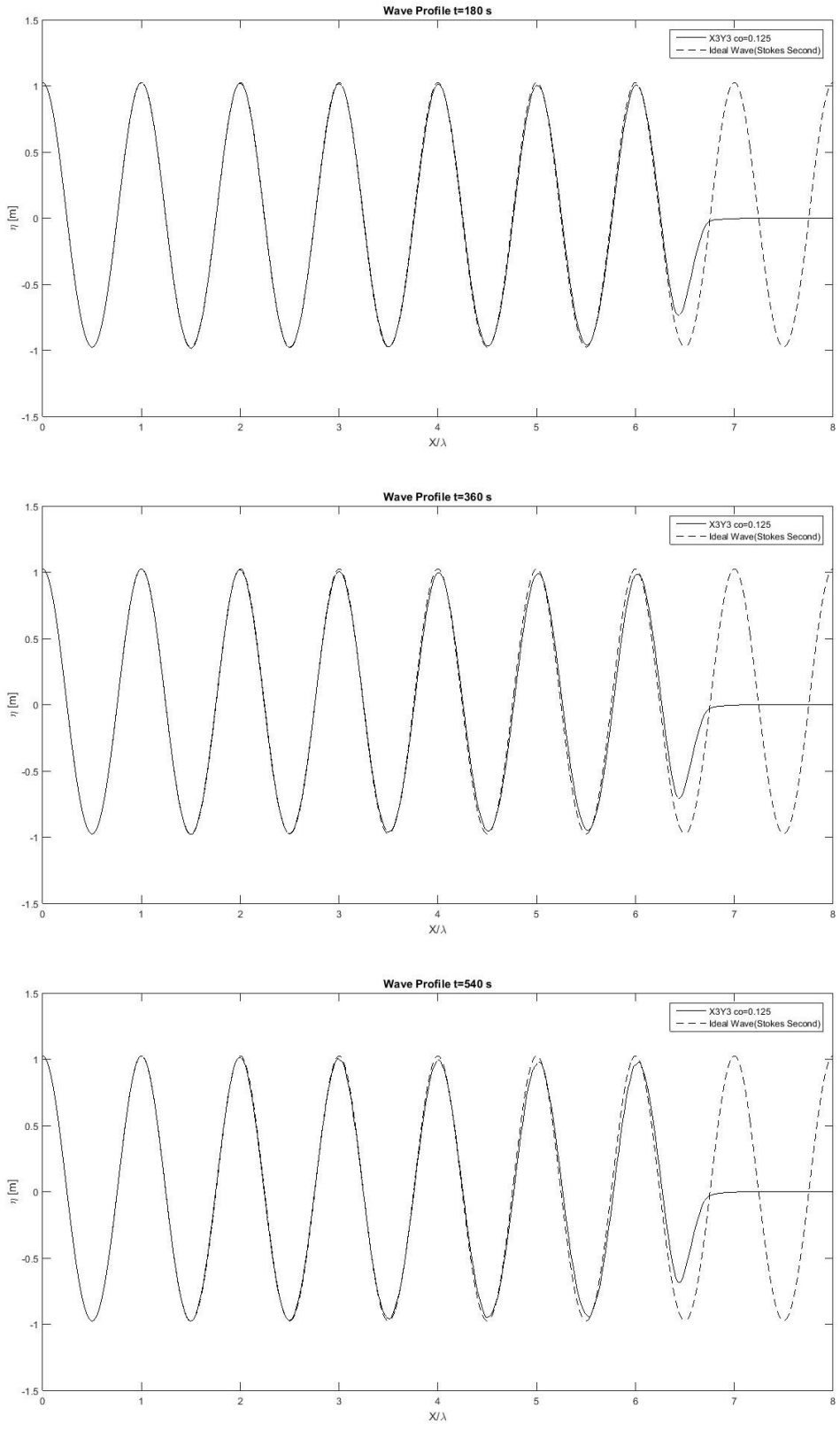

Figure 81 *Wave Profile for case X3Y3 Co=0.125*

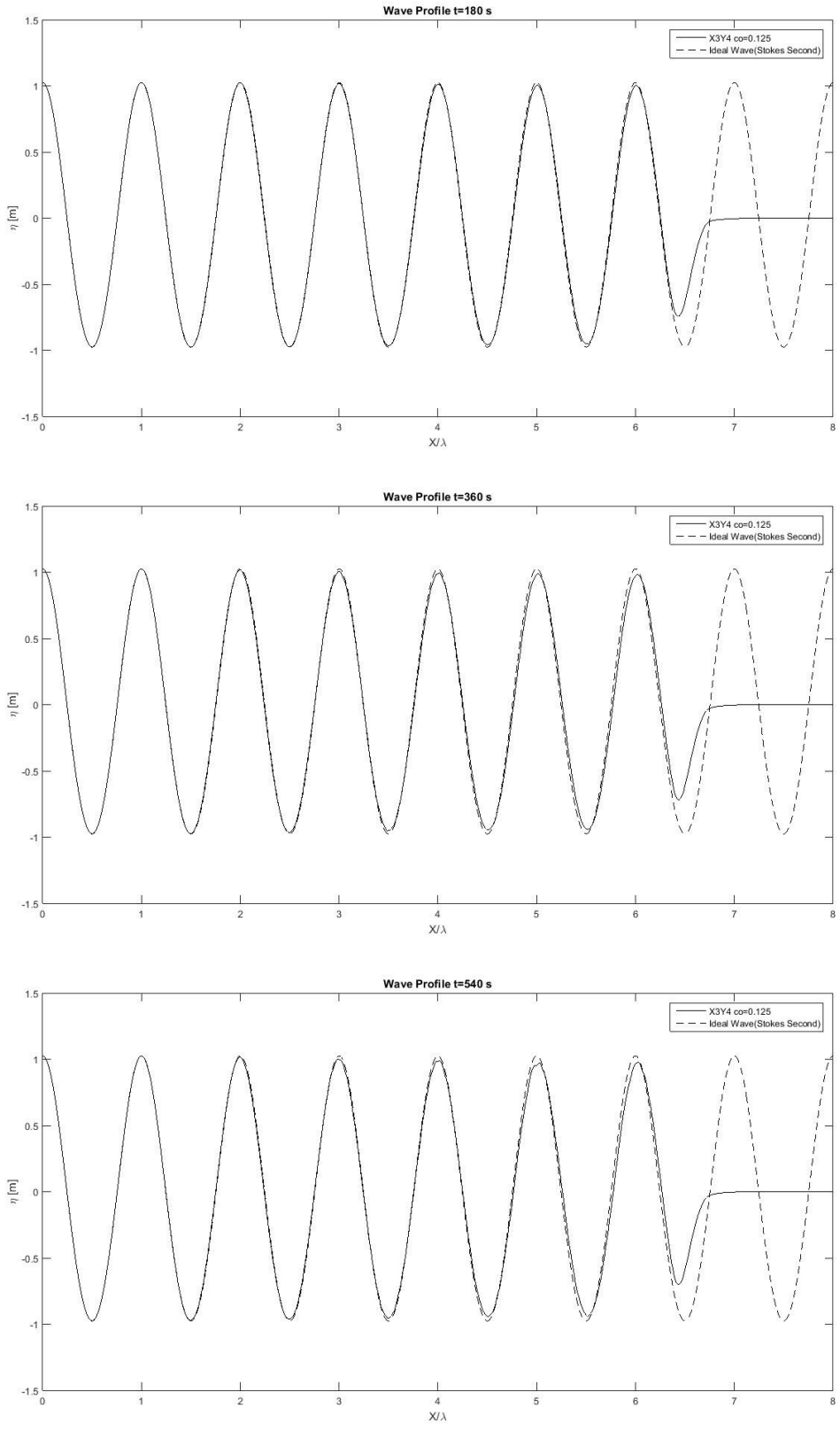

Figure 82 *Wave Profile for case X3Y4 Co=0.125*

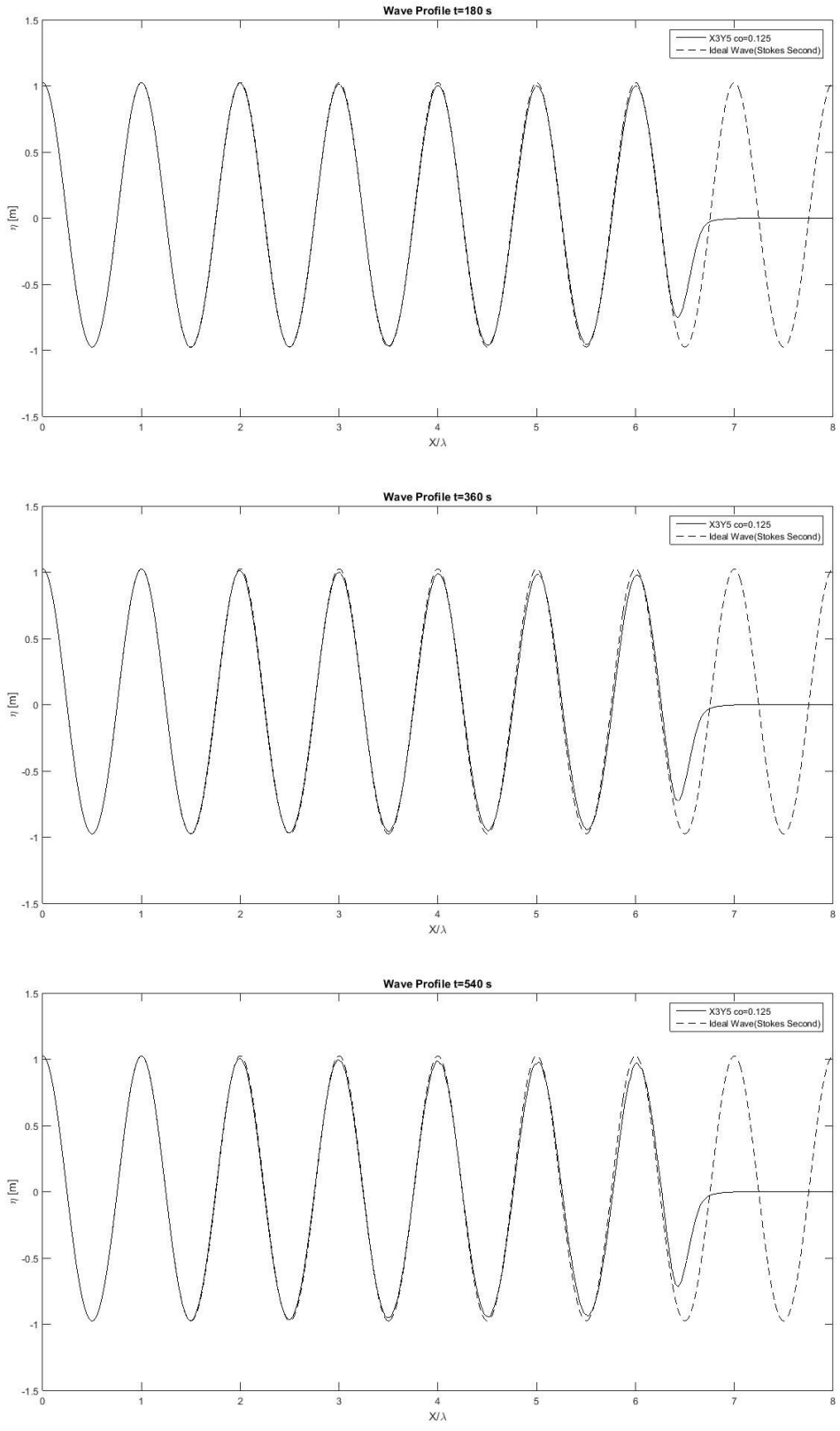

Figure 83 *Wave Profile for case X3Y5 Co=0.125*

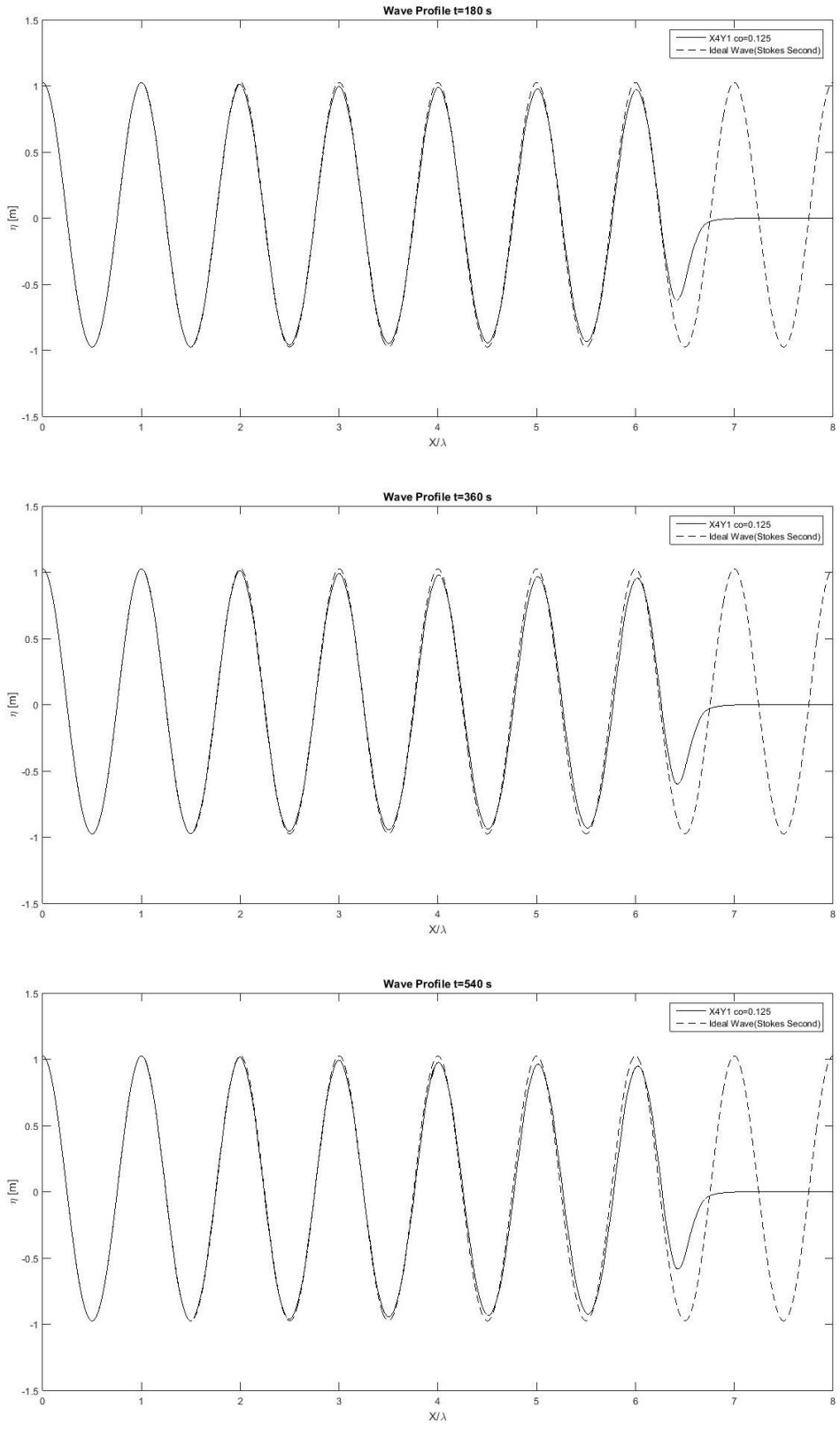

Figure 84 *Wave Profile for case X4Y1 Co=0.125*

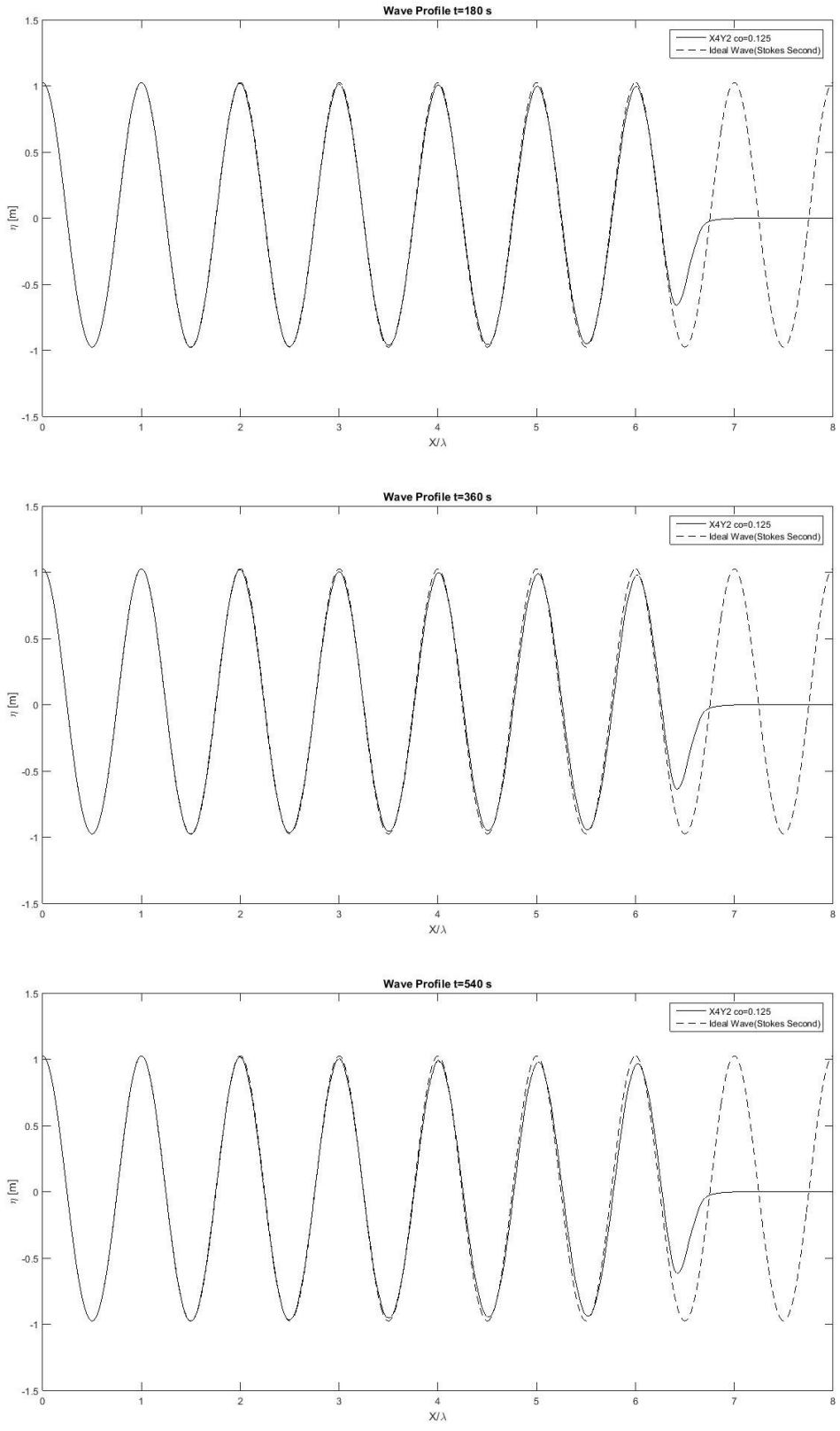

Figure 85 *Wave Profile for case X4Y2 Co=0.125*

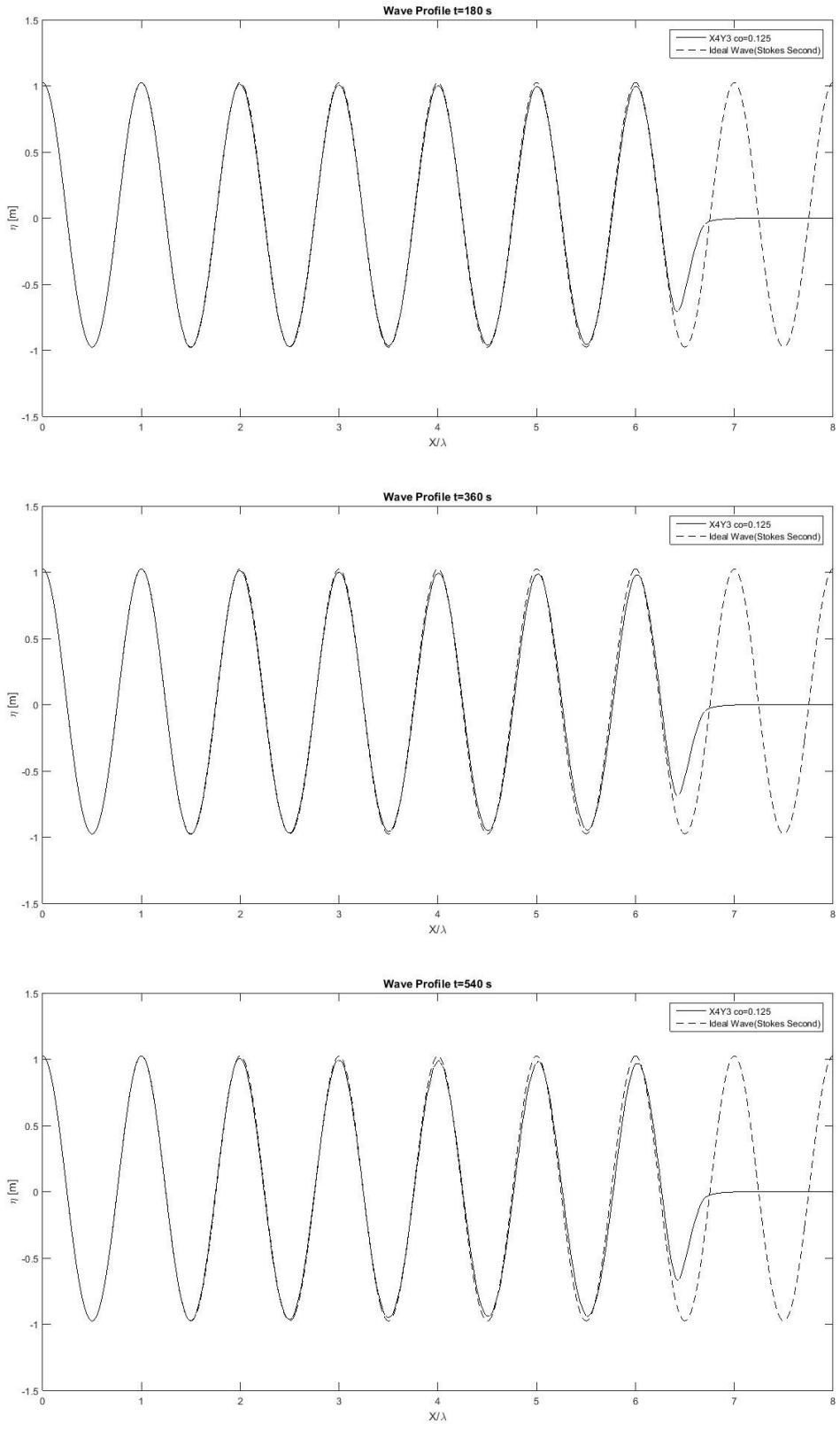

Figure 86 *Wave Profile for case X4Y3 Co=0.125*

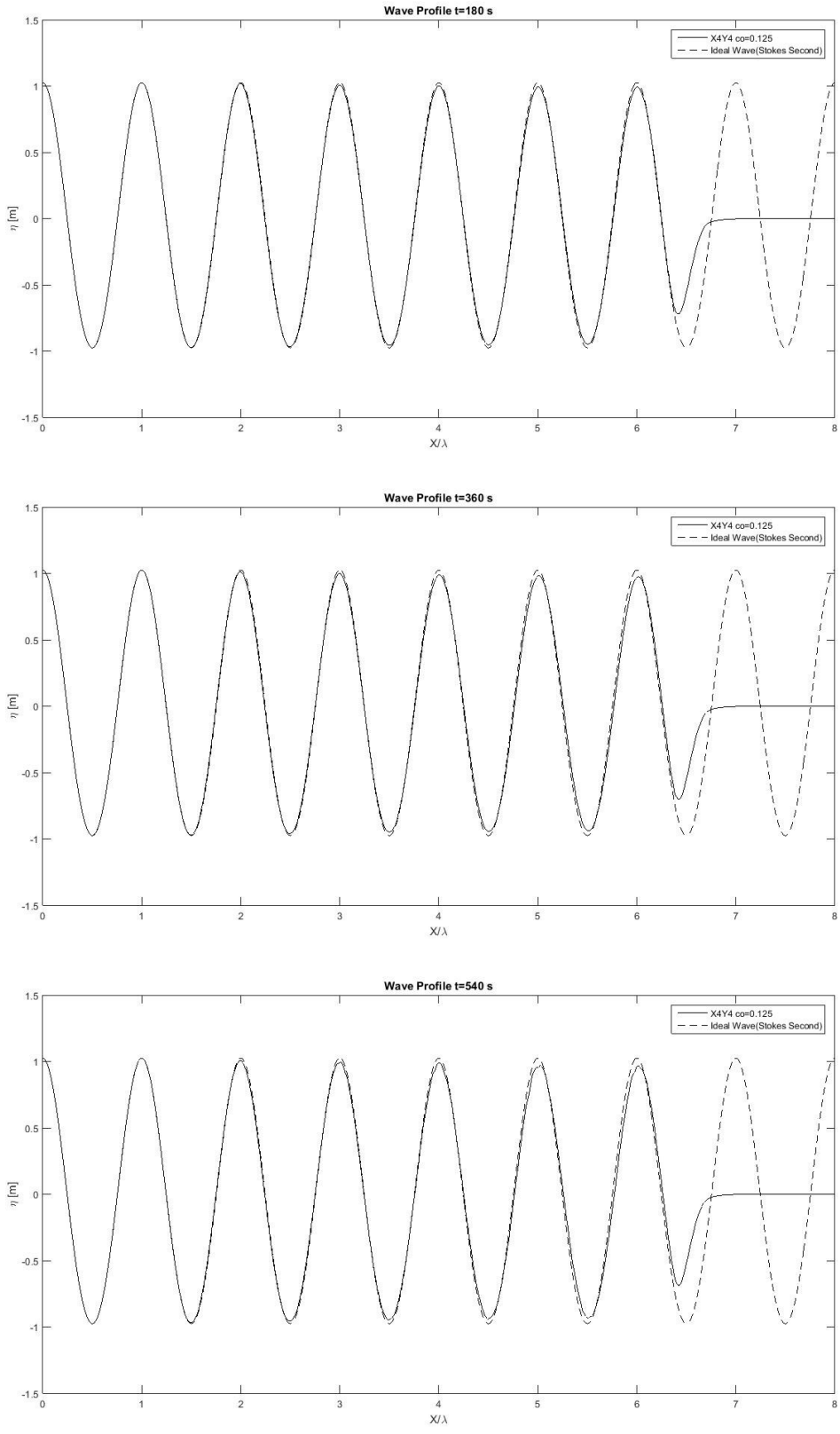

Figure 87 *Wave Profile for case X4Y4 Co=0.125*

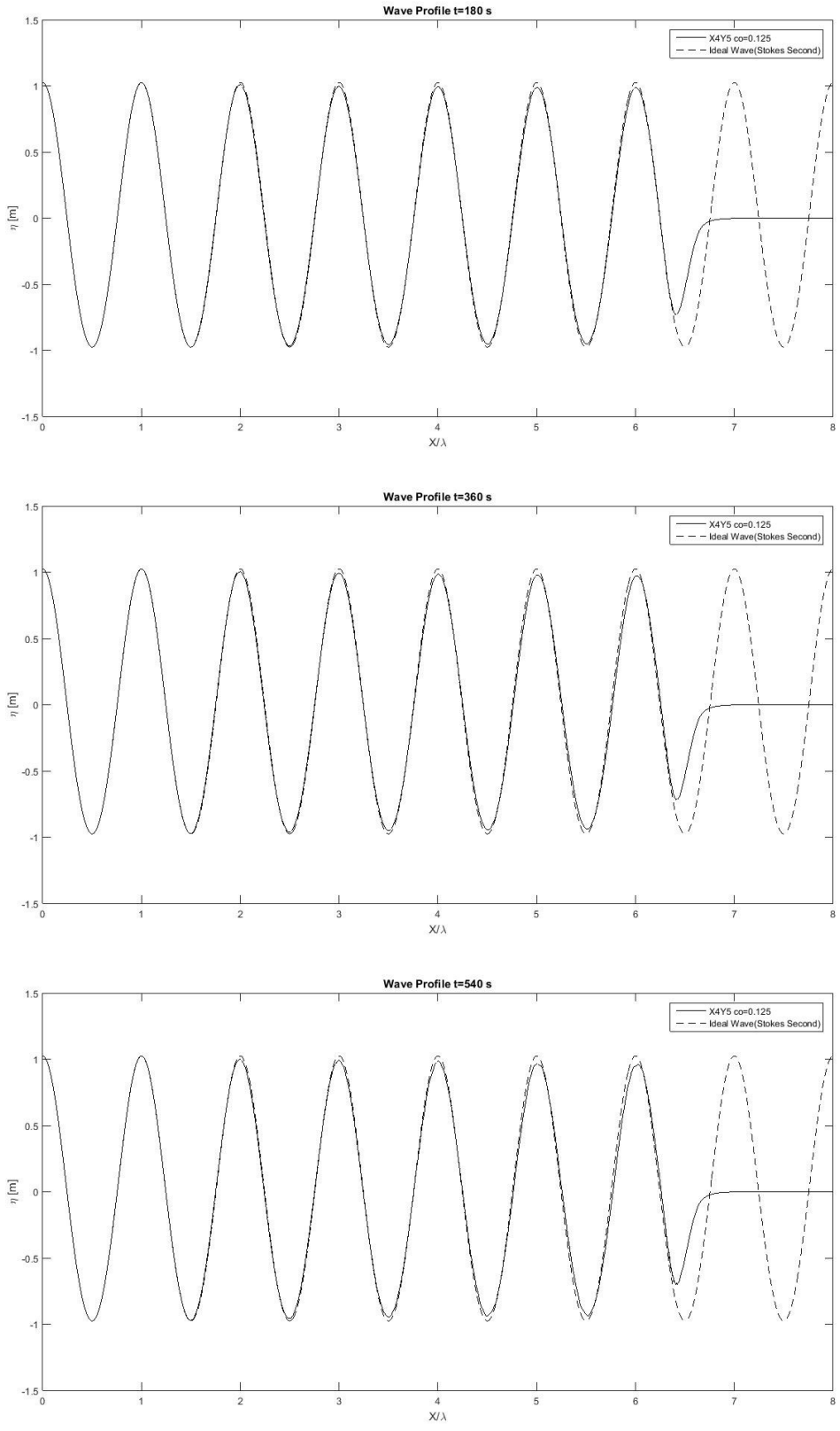

Figure 88 *Wave Profile for case X4Y5 Co=0.125*

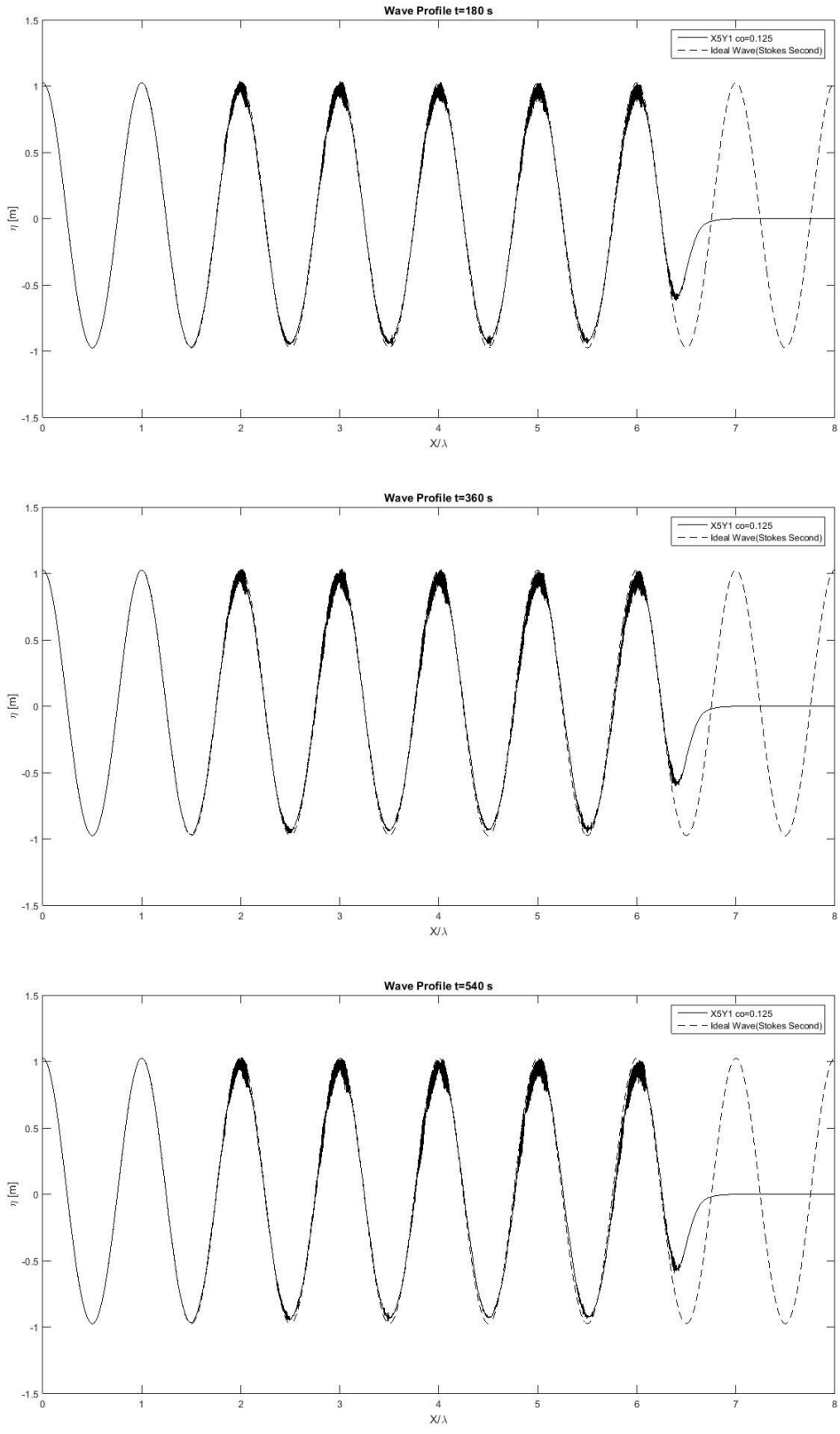

Figure 89 *Wave Profile for case X5Y1 Co=0.125*

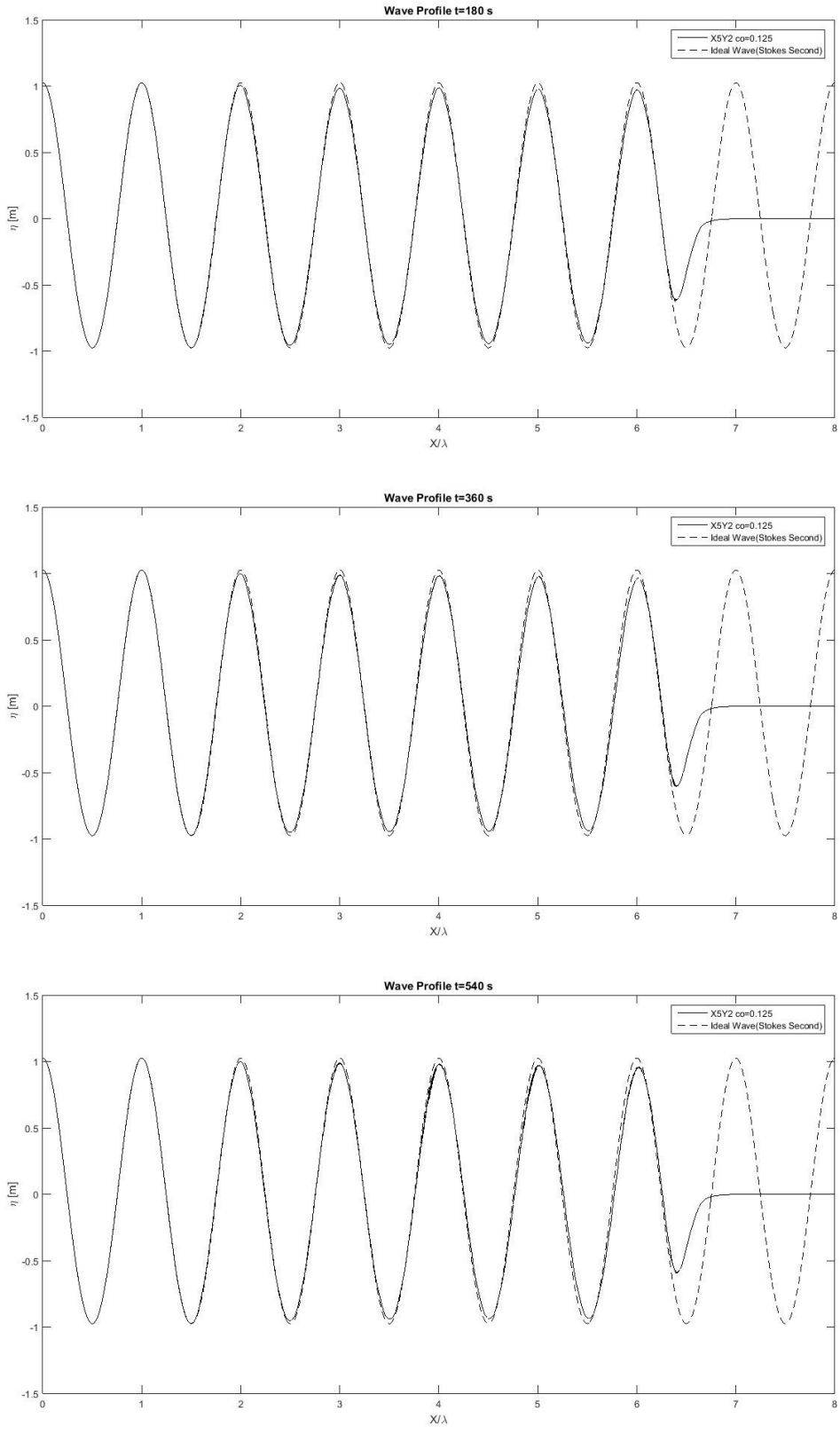

Figure 90 *Wave Profile for case X5Y2 Co=0.125*

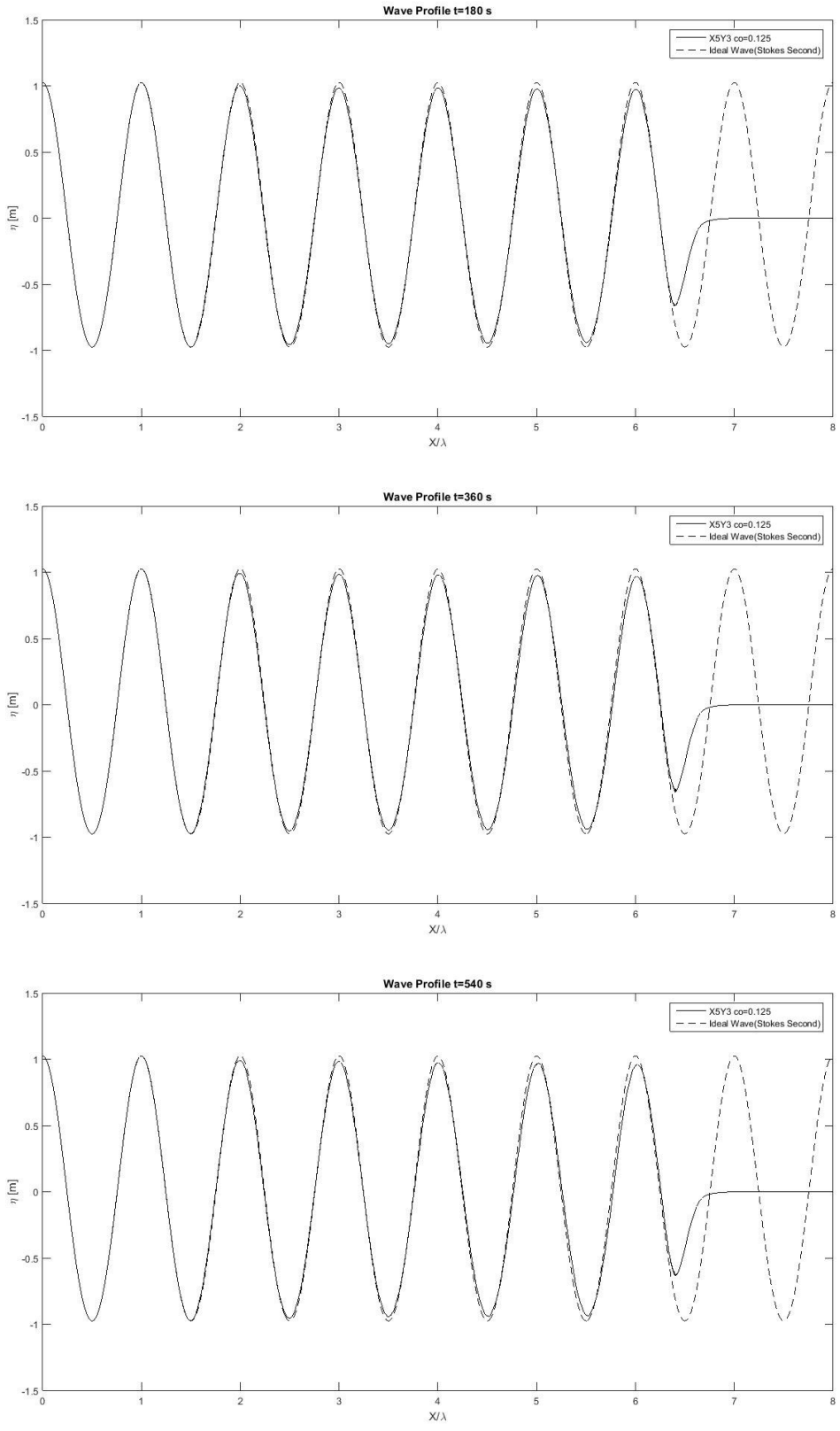

Figure 91 *Wave Profile for case X5Y3 Co=0.125*

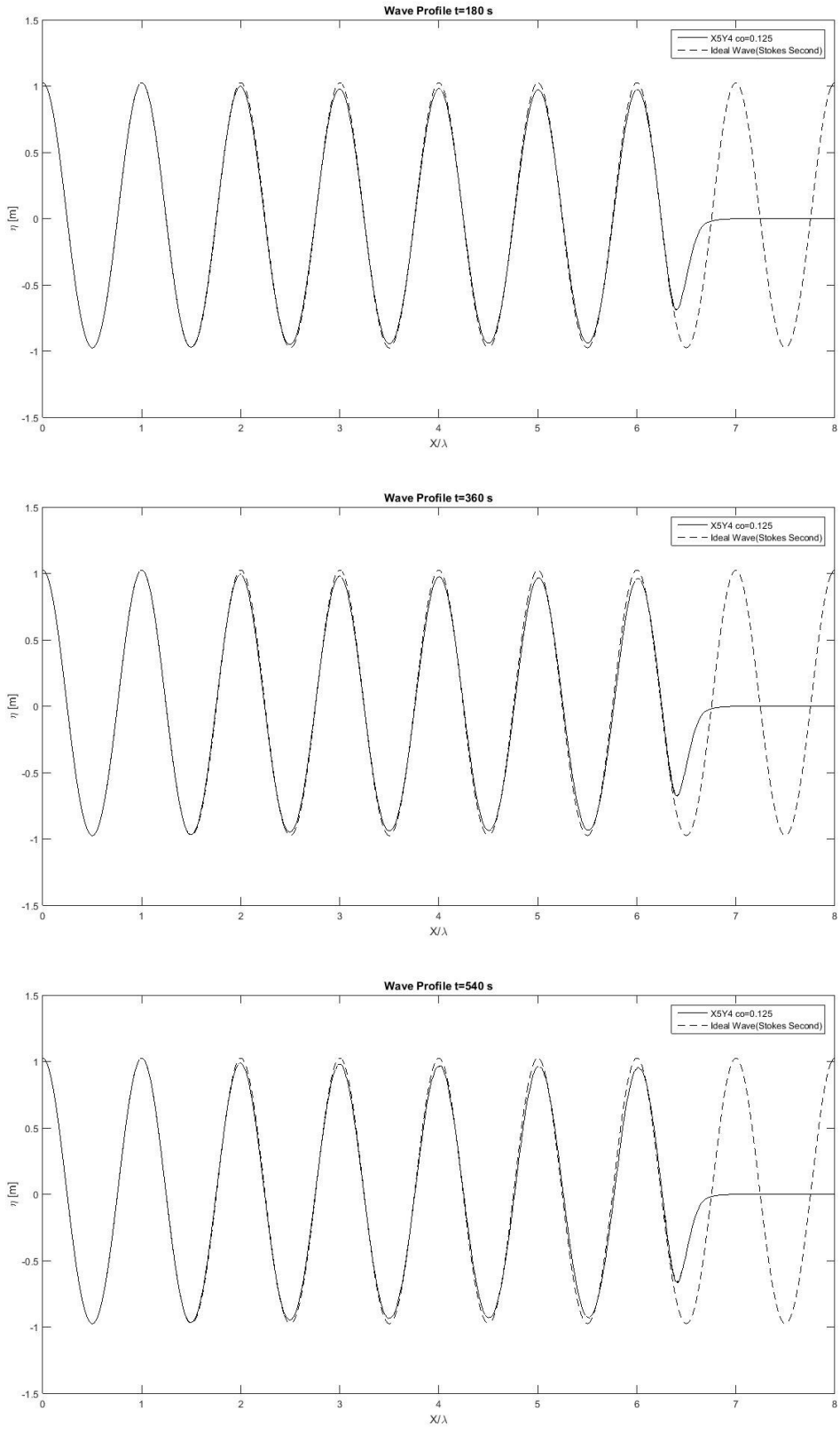

Figure 92 *Wave Profile for case X5Y4 Co=0.125*

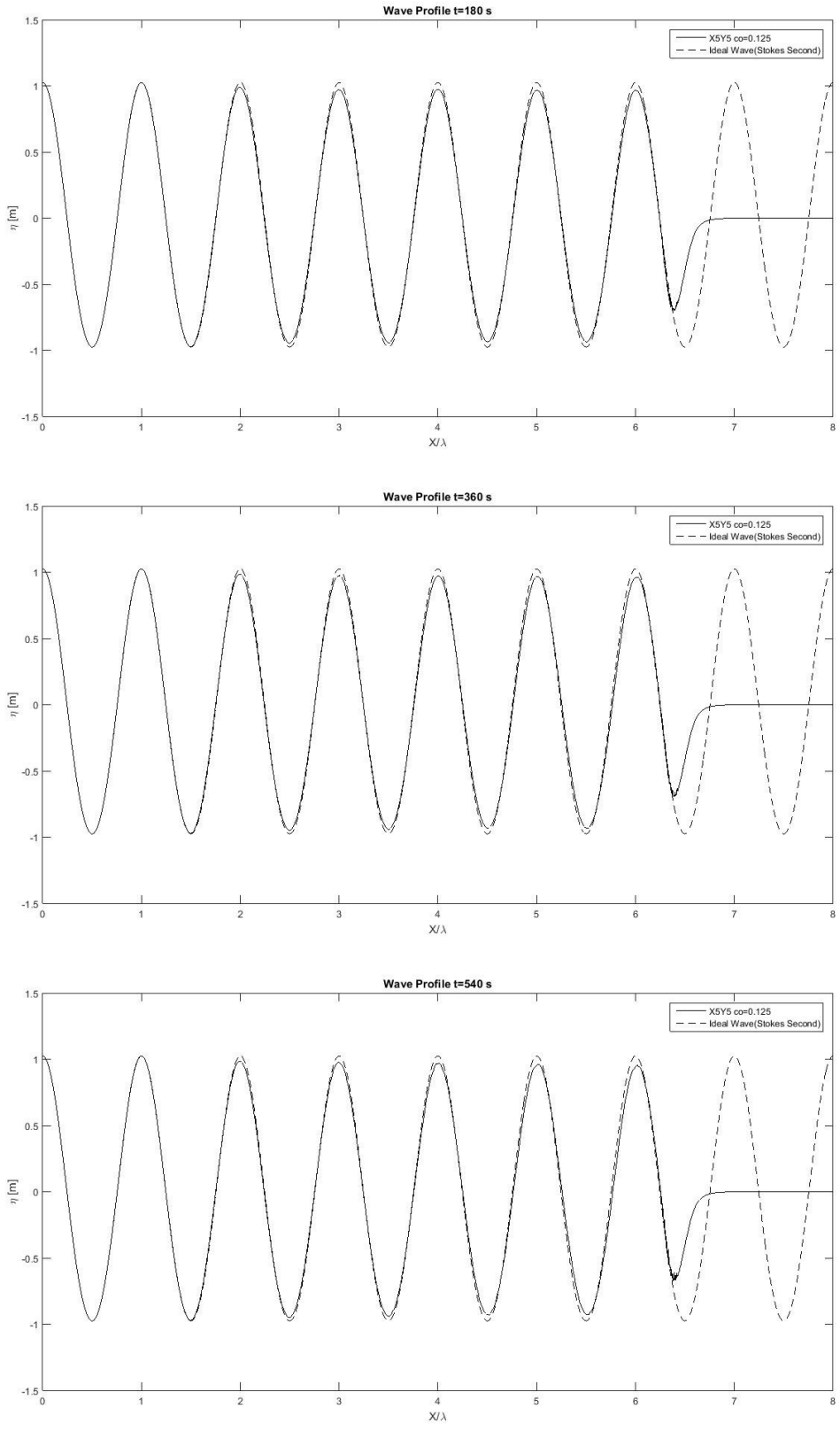

Figure 93 *Wave Profile for case X5Y5 Co=0.125*

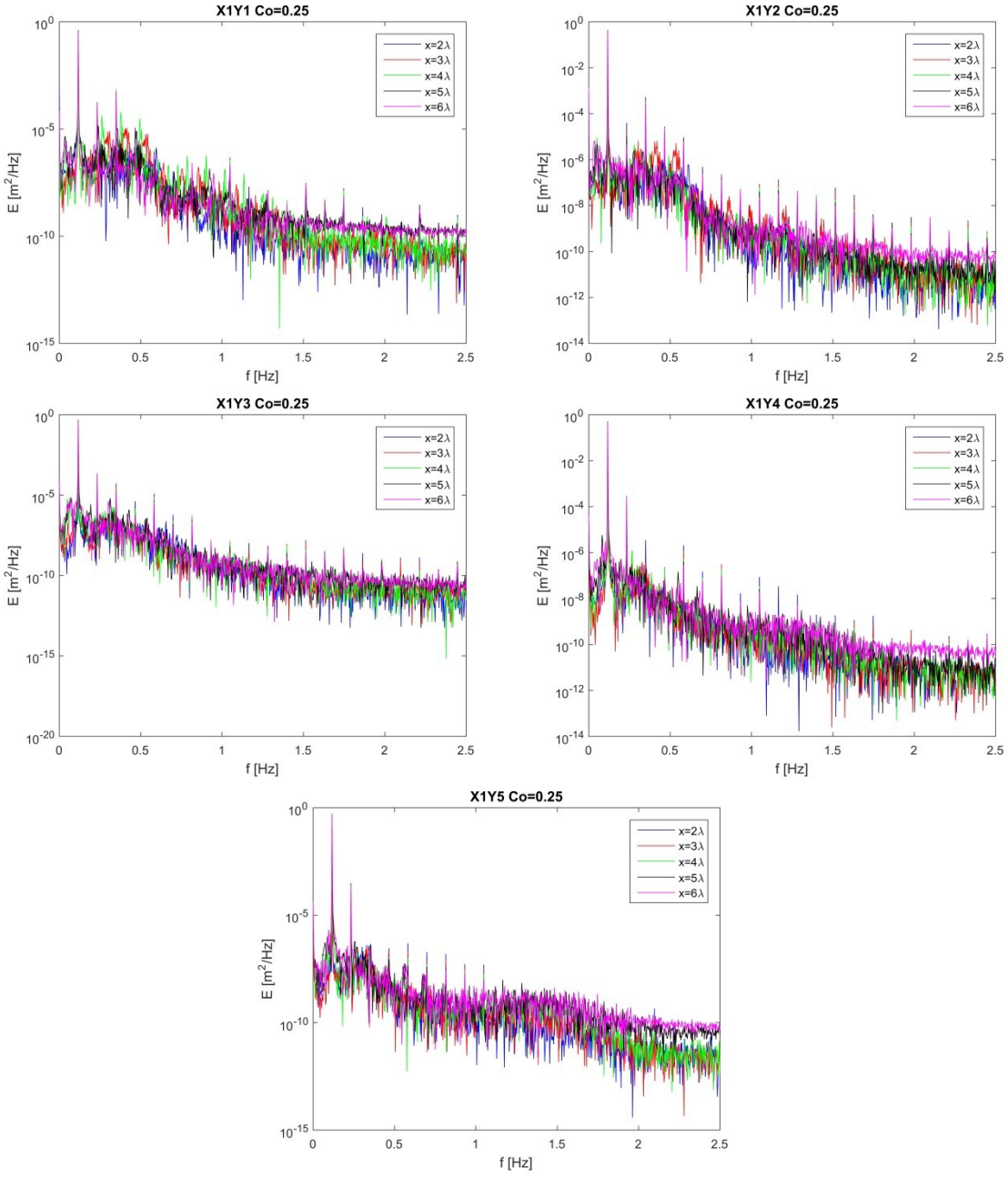

Figure 94 *Fourier analysis of cases with* $\boldsymbol{\delta x = 0.5\,m}$*, Co=0.25*

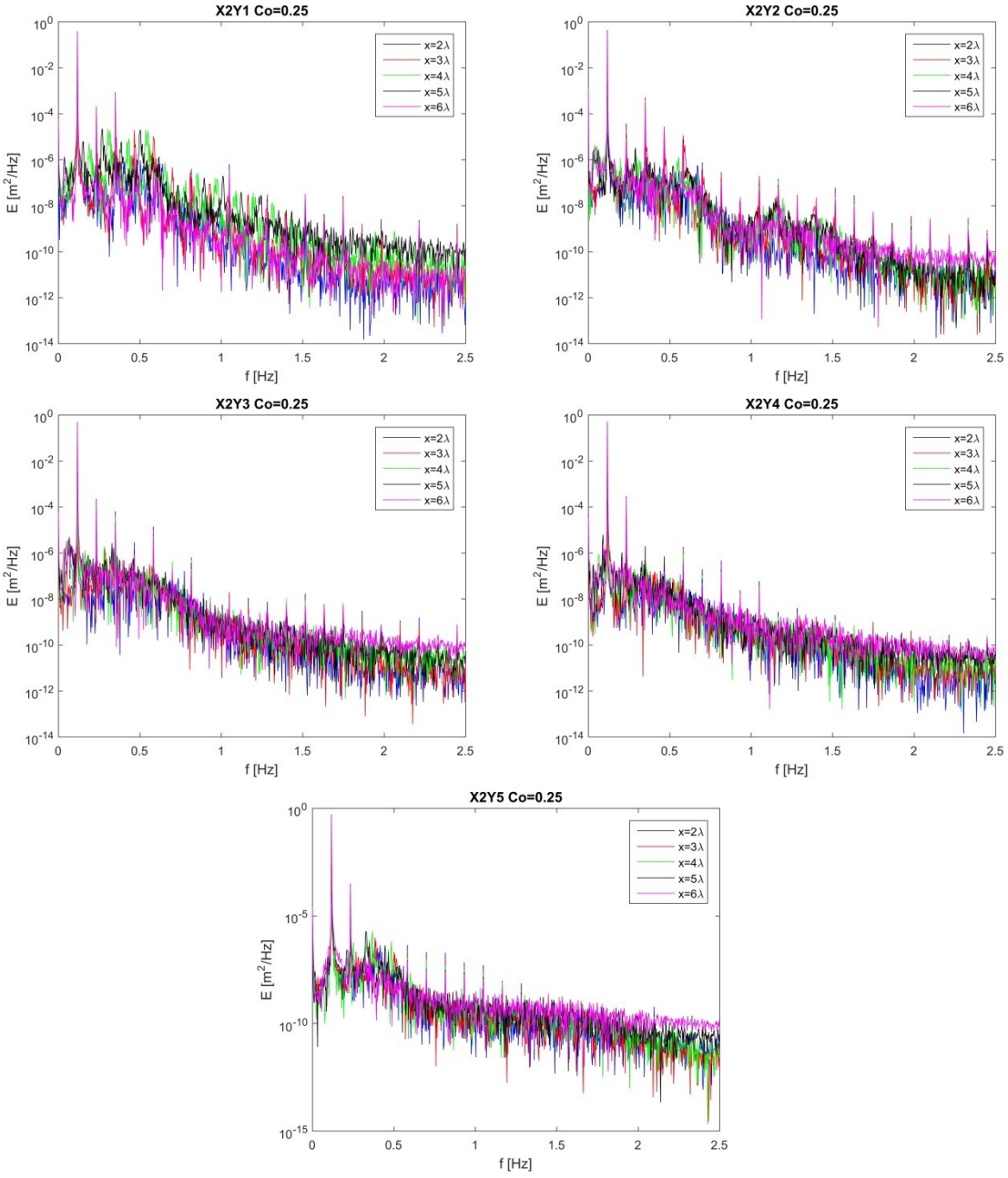

Figure 95 *Fourier analysis of cases with* $\boldsymbol{\delta x = 0.36\ m}$*, Co=0.25*

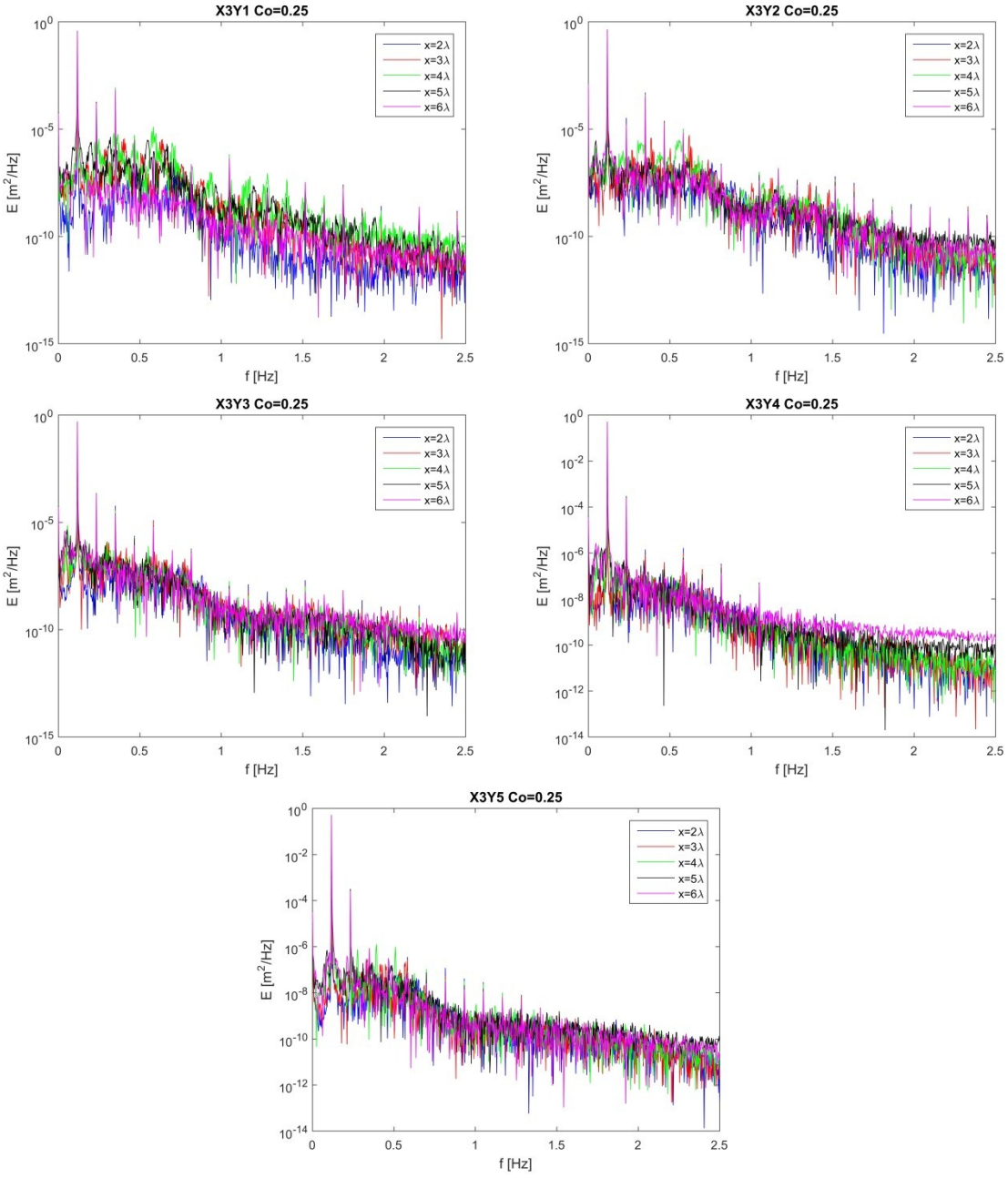

Figure 96 *Fourier analysis of cases with* $\boldsymbol{\delta x = 0.25\ m}$*, Co=0.25*

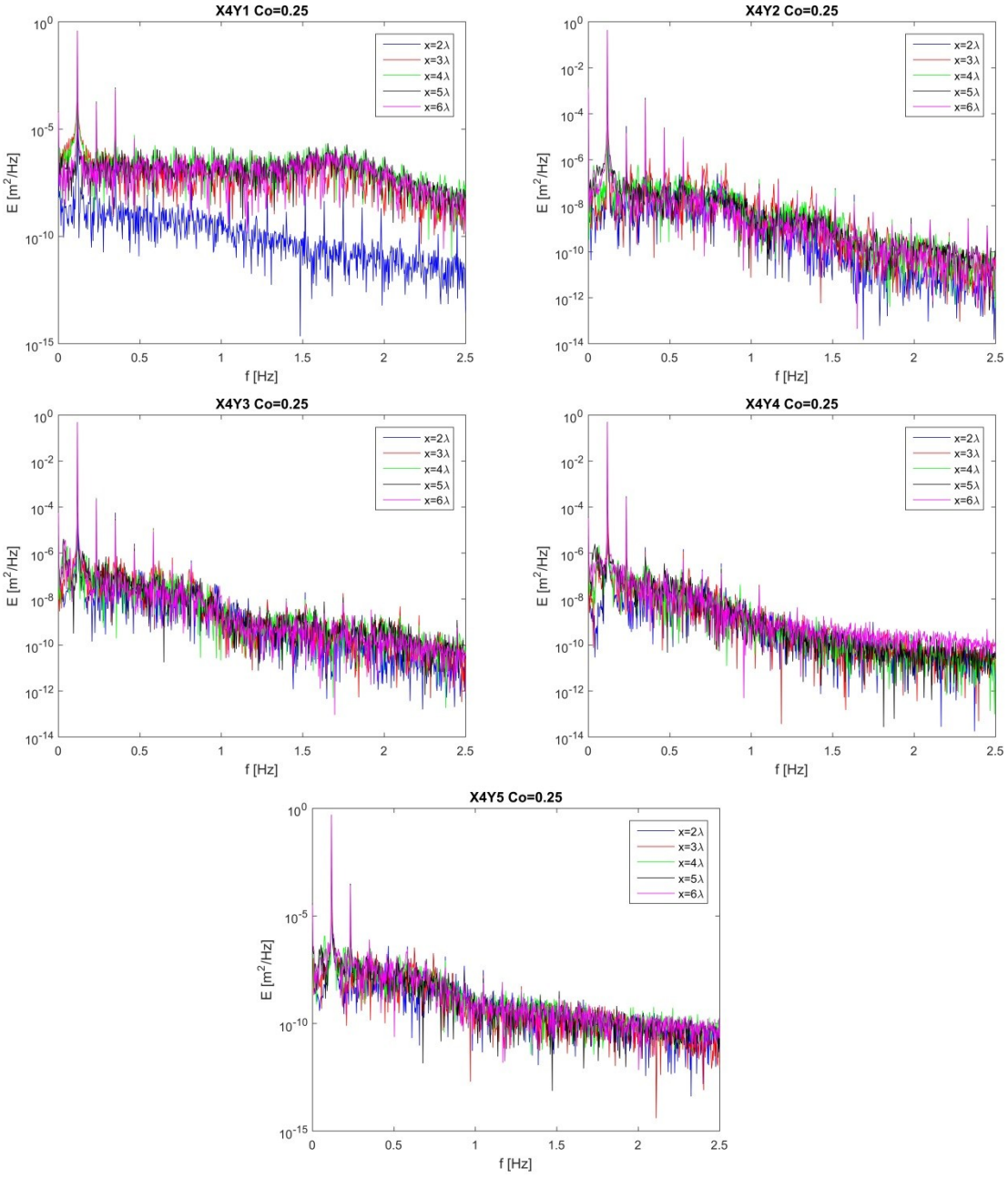

Figure 97 *Fourier analysis of cases with* $\boldsymbol{\delta x = 0.18\ m}$*, Co=0.25*

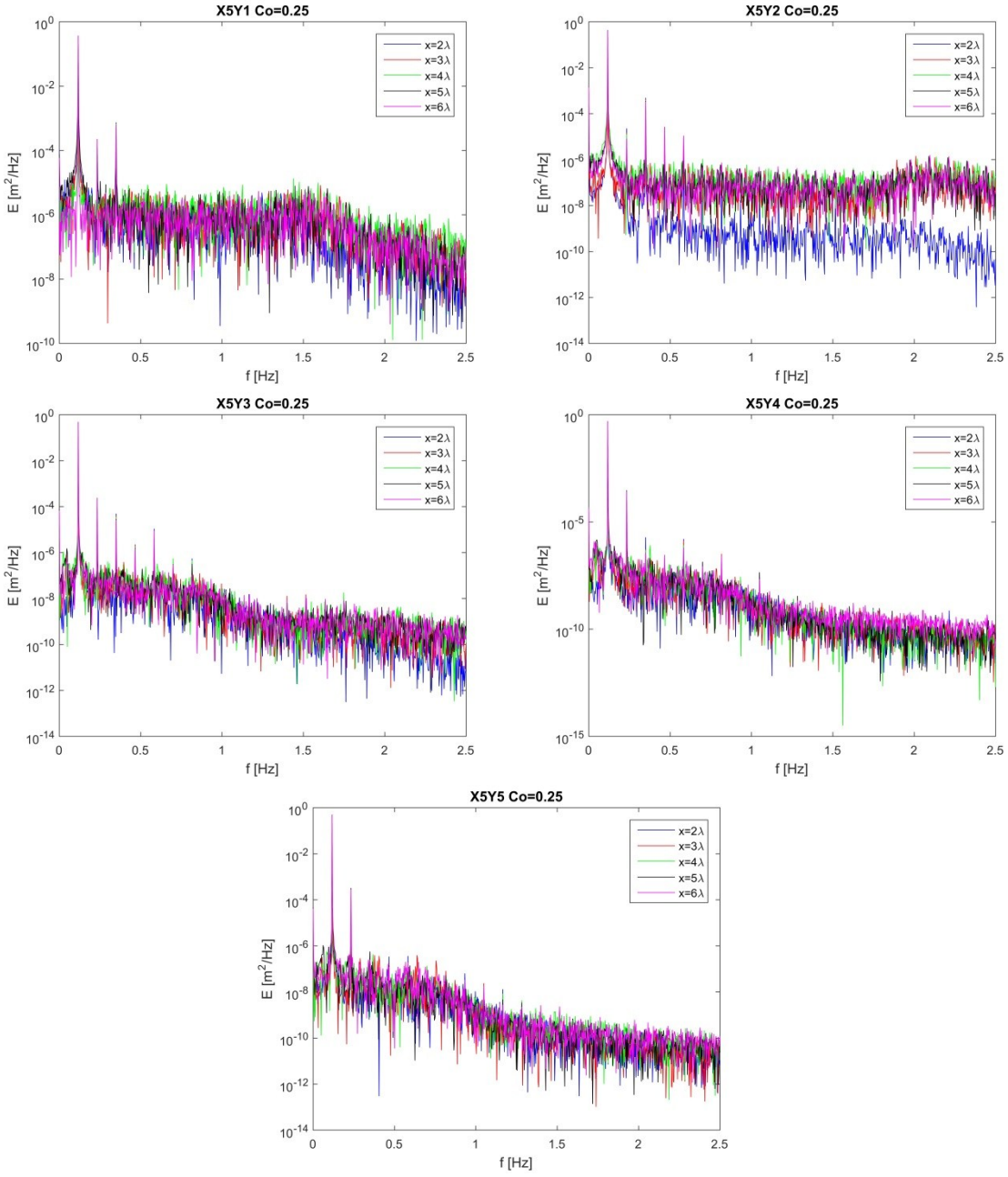

Figure 98 *Fourier analysis of cases with* $\boldsymbol{\delta x = 0.13\ m}$*, Co=0.25*

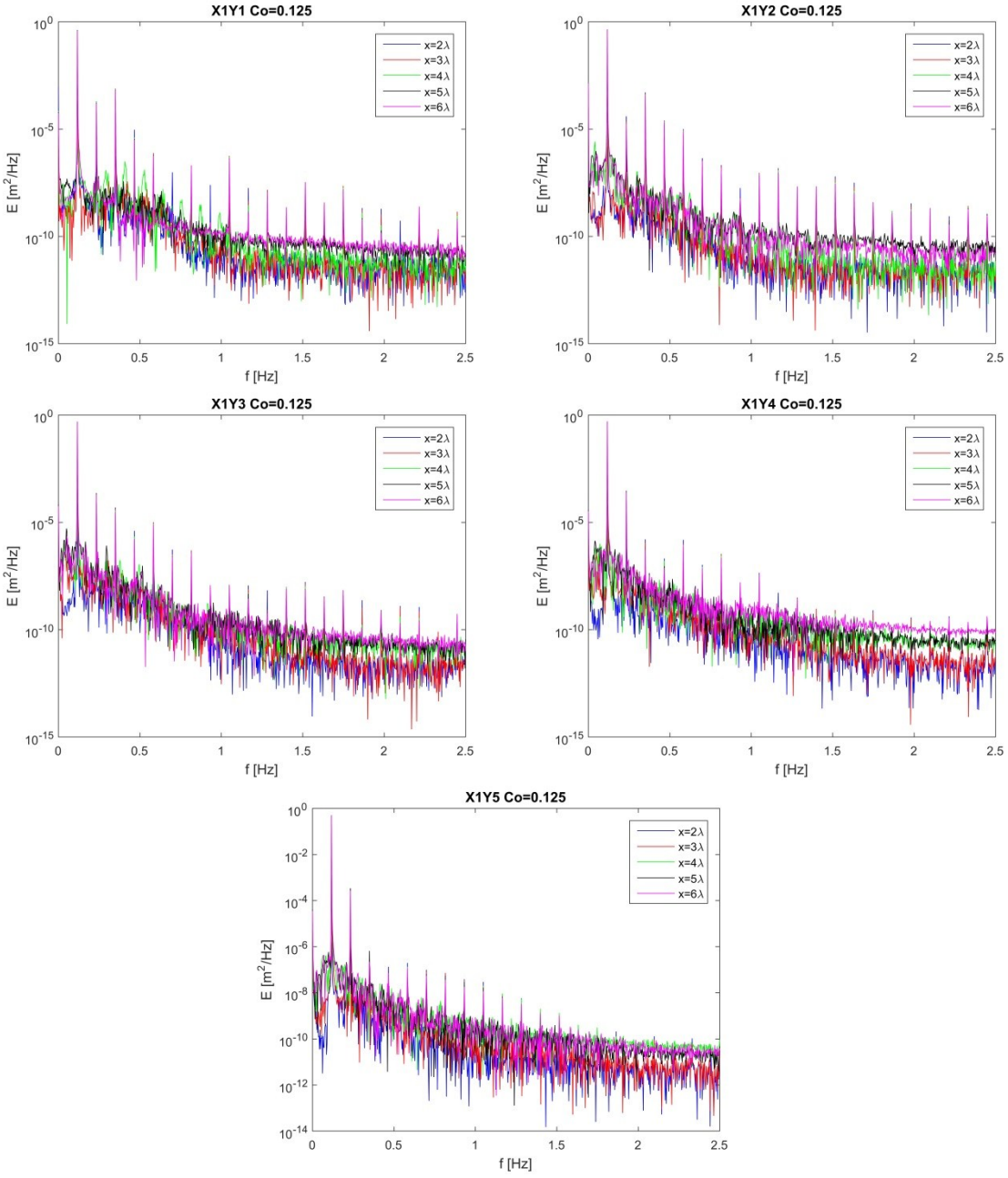

Figure 99 *Fourier analysis of cases with* $\boldsymbol{\delta x = 0.5\,m}$*, Co=0.125*

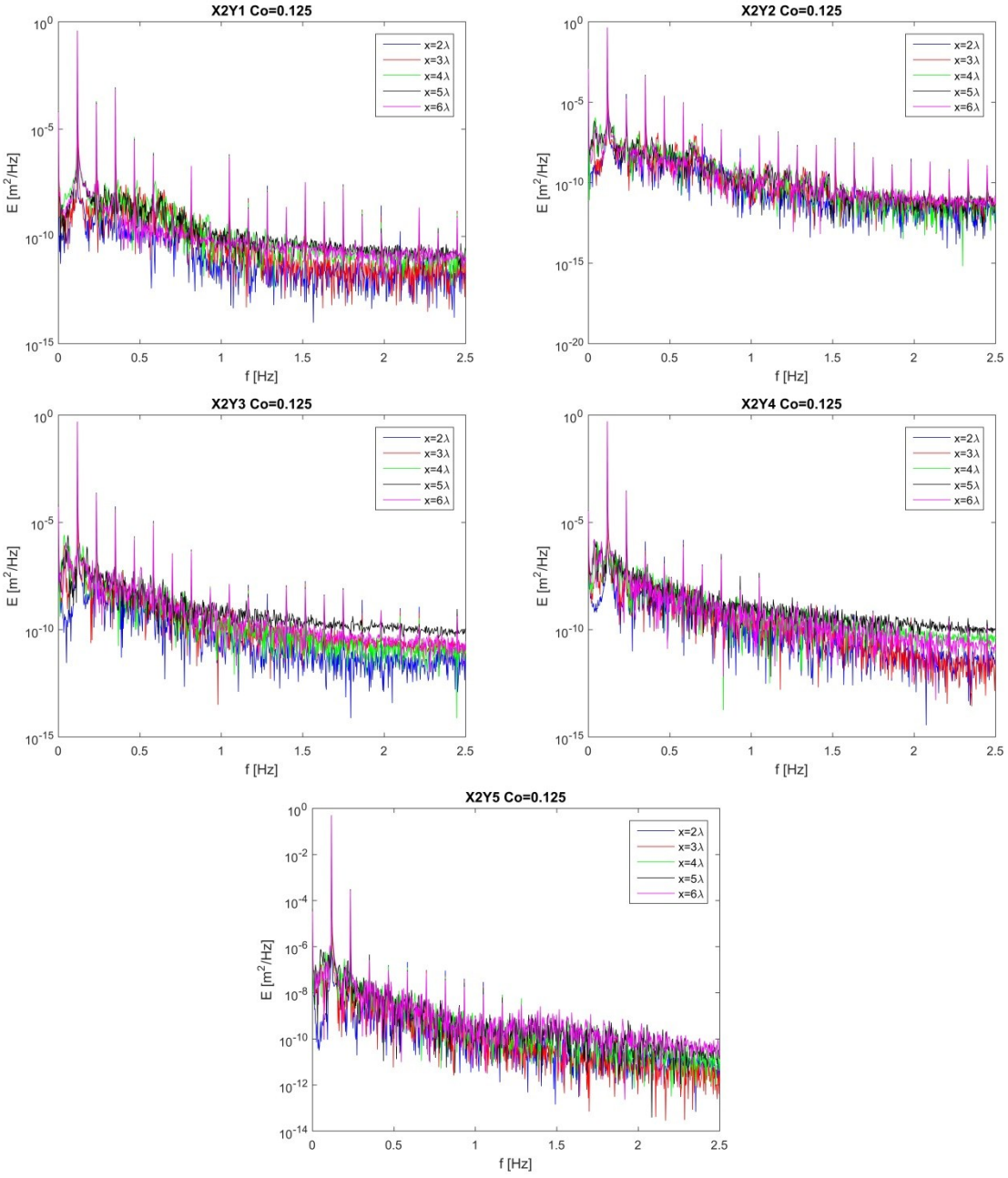

Figure 100 *Fourier analysis of cases with* $\boldsymbol{\delta x = 0.36\ m}$*, Co=0.125*

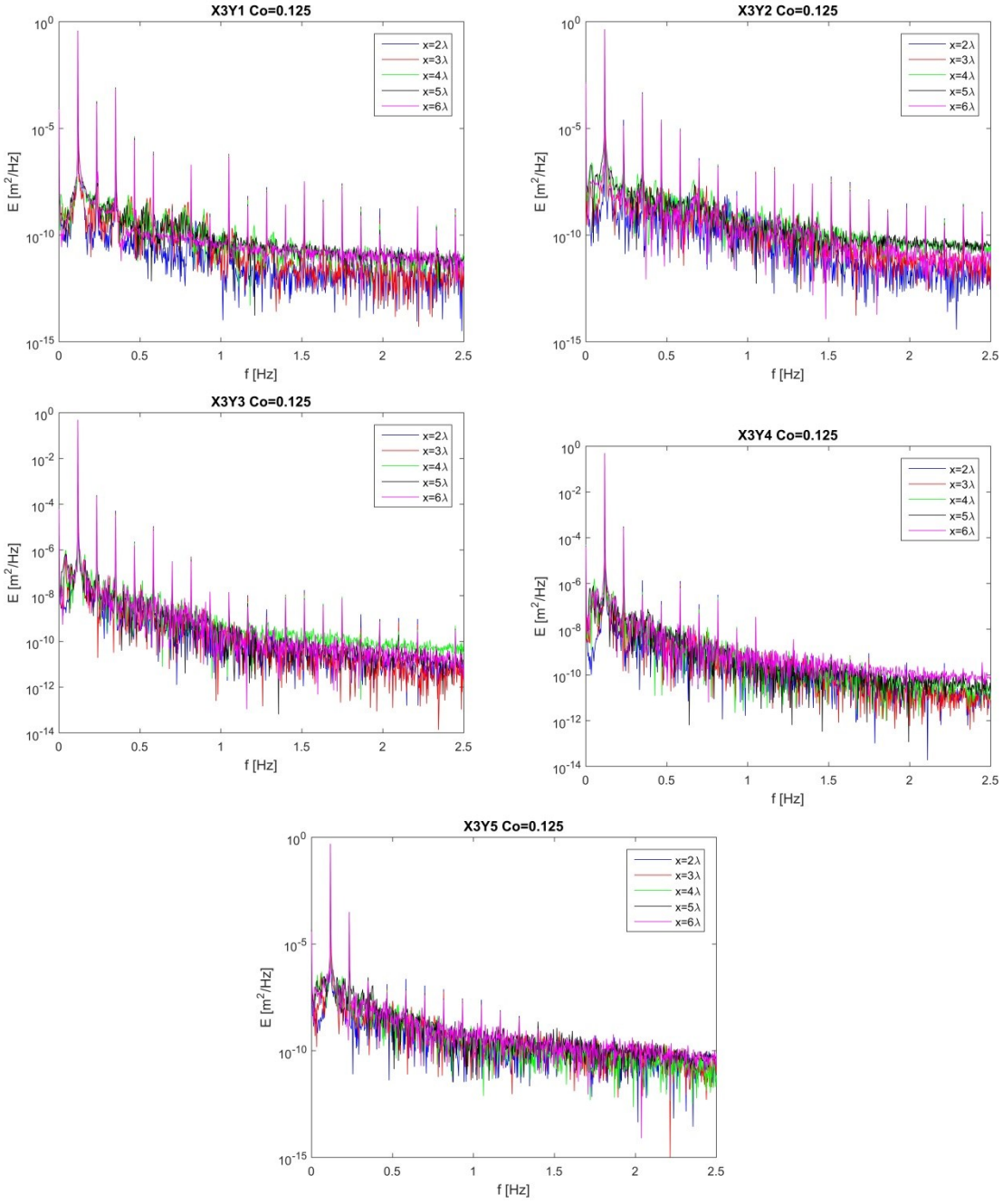

Figure 101 *Fourier analysis of cases with* $\boldsymbol{\delta x = 0.25\ m}$*, Co=0.125*

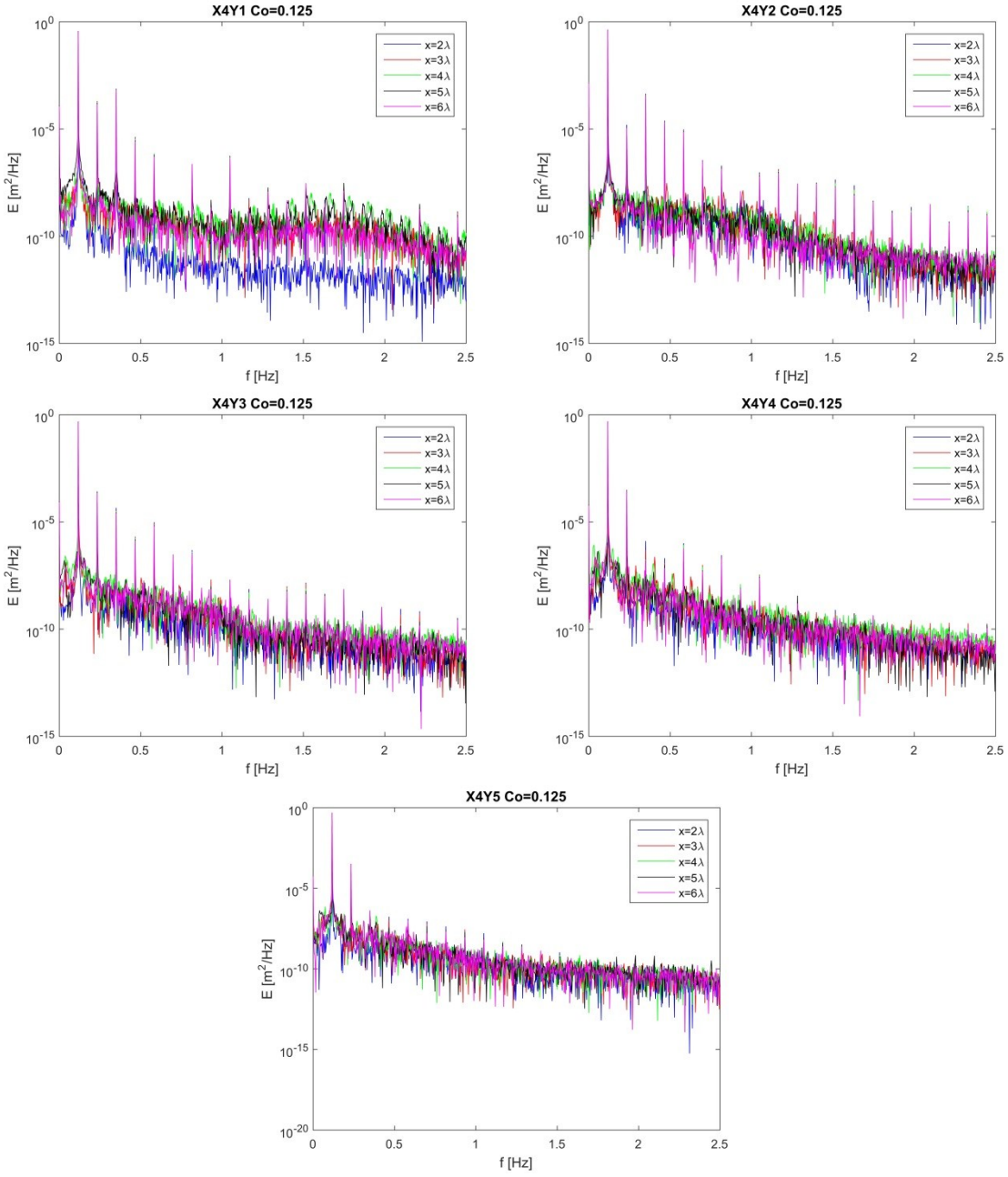

Figure 102 *Fourier analysis of cases with* $\boldsymbol{\delta x = 0.18\ m}$*, Co=0.125*

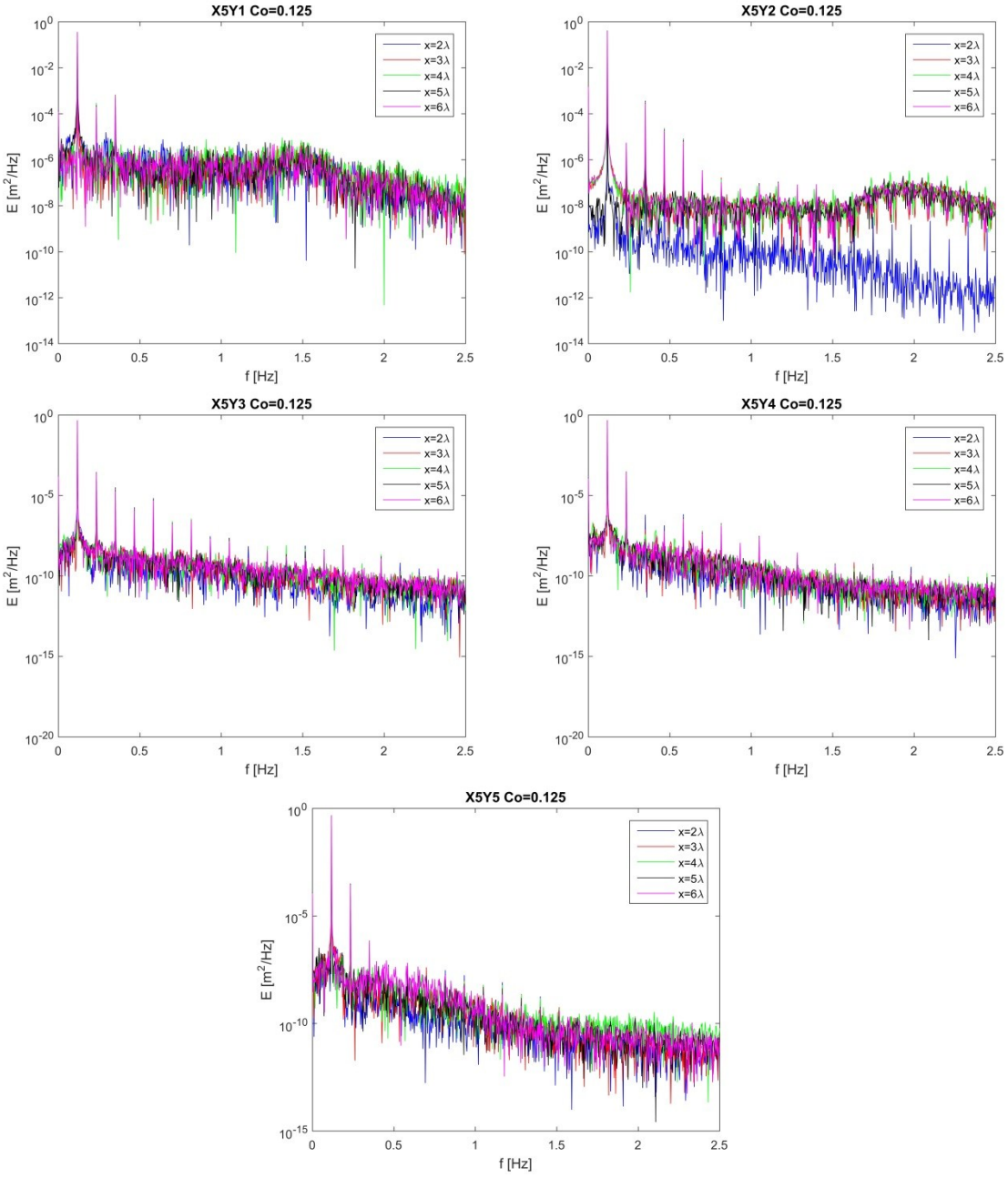

Figure 103 *Fourier analysis of cases with* $\boldsymbol{\delta x = 0.13\ m}$*, Co=0.125*